Regularized Image Up-sampling

Hussein A. Aly

Ottawa-Carleton Institute for Electrical & Computer Engineering
School of Information Technology & Engineering (SITE)
University of Ottawa
Ottawa, Ontario, Canada

March 2004

A thesis submitted to the University of Ottawa in partial fulfilment of the requirements of the degree of Doctor of Philosophy.

Abstract

This thesis addresses the problem of performing image magnification to achieve higher perceived resolution for grey-scale and color images. A new perspective on the problem is introduced through the new concept of a *theoretical camera* that can acquire an ideal high resolution image. A new formulation of the problem is then introduced using two ingredients: a newly designed observation model and the total-variation regularizer. An observation model, that establishes a generalized relation between the desired magnified image and the measured lower resolution image, has been newly designed based on careful study of the physical acquisition processes that have generated the images. The result is a major contribution of this thesis: a closed-form solution for obtaining the observation model. This closed form has been implemented and observation models were obtained for different typical scenarios, and their performance was shown to outperform observation models used in the literature. Two new theorems for designing the theoretical camera, adapted to the display device used, on arbitrary lattices have been developed. The thesis presents new analysis with a signal processing perspective that justifies the use of the total-variation regularizer as *a priori* knowledge for the magnified image; this analysis is defined on both the low and the high resolution lattices simultaneously. The resulting objective function has been minimized numerically using the level-set method with two new motions that interact simultaneously, leading to a solution scheme that is not trapped in constant-image solutions and converges to a unique solution regardless of the initial estimate. For color images, the *human visual system* characteristics were involved in the choice of the color space used in the implementation. It was found that a proper color space such as YCbCr that focuses on magnifying a better luminance channel provided the same result as a vectorial total-variation formulation, but at a reduced computational cost. The quality of the magnified images obtained by the new approaches of this thesis surpassed the quality of state-of-the-art methods from the literature.

Acknowledgments

I would like to express my deepest gratitude to my supervisor Professor Eric Dubois for his continuous supervision and help during all the research phases. He has been involved in every single detail in the research by in-depth weekly discussions. His extremely valuable guidance and criticism were the keys to the contributions achieved.

My thanks go to Professor Tyseer Aboulnasr for her precious advice. My thanks also go to the staff of the School of Information Technology and Engineering for their help and administrative assistance.

I am indebted to the Egyptian Ministry of Defence for their financial support. I am also grateful to the Royal Canadian Mounted Police for providing useful software.

Finally, I would like to thank my parents for their support and prayers from far away. I would like to thank my wife for her continuous support and patience during these three and a half years.

Contents

List of Figures

List of Tables

Notation

$\|\cdot\|_p$	p-norm
$\|\cdot\|$	2-norm
$\langle\ ,\ \rangle$	Inner product
$\circ$	Schur product
ΔT	Time step
$\setminus$	Set difference
$\triangle$	Laplacian operator
$\nabla_{\mathbf{x}}$	Spatial gradient
κ	Mean curvature
$\kappa^{\perp}$	Dual mean curvature
div	Divergence operator
diag	Diagonal matrix
σ	Standard deviation
ν	Speed of evolution of a front
λ	Regularization parameter
ϕ	Prototype for continuous-space(-time) reconstruction basis
$\overset{\circ}{\phi}$	Prototype for continuous-space(-time) dual reconstruction basis
Γ	HR image sampling lattice
Γ^*	HR image reciprocal sampling lattice
Λ	LR image sampling lattice
Λ^*	LR image reciprocal sampling lattice
$(\Lambda : \Gamma)$	index of Γ in Λ
Ξ	Sampling lattice
Ξ^*	Reciprocal sampling lattice
$\ell_p(\Lambda)$	The space of all p-summable discrete functions defined over a lattice Λ
$L_p(\mathbb{R}^D)$	The space of all Lesbeque p-integrable functions defined in $\mathbb{R}^D$
$.^T$	Transpose
$.^{(n)}$	Value at iteration n
$d(\cdot)$	Volume of a unit-cell of the sampling lattice
f_c	Continuous-space(-time) image
f_1	HR digital image

f_2	LR digital image
F	Fourier transform of image f
F^*	Complex conjugate of F
$\mathcal{J}$	Cost function of objective criterion
$\mathfrak{L}$	Non-negative monotonically increasing functional
$\mathcal{P}_.$	Unit cell of a sampling lattice
$\mathfrak{P}$	Projection operator
$R_.$	Autocorrelation
$\mathbb{R}^D$	D-dimensional real space
$S_.$	Power spectral density
$\tilde{t}$	Artificial time
u	Horizontal frequency variable
v	Vertical frequency variable
V	Sampling Matrix
$\mathbf{V}$	Reconstruction Space
$\mathcal{W}_T$	Spatio-temporal domain of an image
x	Horizontal spatial variable
X	Horizontal spatial sampling period
y	Vertical spatial variable
Y	Vertical spatial sampling period

Chapter 1

Introduction

1.1 Problem area

This thesis addresses the problem of image magnification to achieve higher perceived resolution from a variety of acquired sensor data. The raw image output of the sensor is considered to be the *lower resolution* (LR) image(s); this means that the resolution is lower than that desired or required by the application. The desired *higher resolution* (HR) image will be a better representation than the LR images in terms of two aspects: size and perceived information content (resolution). The LR images here are obtained by capturing a real-world natural scene by a physical imaging system. Imaging systems provide the coarse information content of the scene as well as a portion of the finer details. The extent of this portion depends on the quality of the imaging system. High quality images with deep fine details can be obtained by using higher quality (expensive) imaging systems. Unfortunately, many applications demand higher quality images than the most high-end current existing imaging system, or specifically higher than the capability of the imaging system available. Imaging systems are governed by design requirements like size and weight and the technology of the sensors that capture the light. These requirements and the current technology limits appear in the

form of optical and electronic processes that degrade the LR images obtained. These degradations usually result in LR images suffering from loss of resolution and noise. The scene's finer details are the most affected by these degradations. Should higher perceived resolution and size be required, an appropriate digital image magnification technique is necessary.

Fortunately there are two important facts: first, natural images possess far greater fine details compared to what can be captured by any current imaging system. Second, the degradation in the imaging system does not fully eliminate all the image fine details but rather attenuates them. Based on these two facts, some of the fine details are expected to be embedded and exist in the given LR images by the digitization process. This is called aliasing, which might be perceived as outlier patterns in the LR images. This invigorates research in digital image magnification that will hopefully be capable of utilizing and reconstructing these embedded information contents as much as possible in the HR image. This kind of reconstruction approach is called *super-resolution* in the image processing literature. The approach in this thesis belongs to this class. In this thesis the approach is named a more self-descriptive one which is *regularized image up-sampling*, in accordance with the theory of digital signal processing and the mathematical theory for solving ill-posed inverse problems like this one.

The problem area described above is specified by the definition of the underlying sensor data. This thesis covers two different types of sensor data, namely grey scale and color. Every type stands alone as a separate problem and many research approaches address each one separately. In this thesis, some of the theorems developed is used in both of them, namely a new designed observation model. Additionally, independent theory is developed to specifically suit each case. Two additional problems that can greatly benefit from the solutions developed in this thesis are the ones associated with color filter array and color image sequence sensor data. The associated four problems for these types of sensor data are listed below in increasing level of complexity.

1.1.1 Regularized grey scale image up-sampling

In this problem the sensor data is a grey-scale LR image. There is extensive literature addressing this problem. Usually the success of the formulation for this basic problem, as verified by the results, is crucial and considered to be the basis for further extension in solving the other more complex related problems below.

1.1.2 Regularized color image up-sampling

In this problem the sensor captures 3 different measurements from the visual light spectrum of the scene. The spectrum is usually analyzed by a beam splitter. The sensor data output are three (or more) values called the color channels. When appropriately combined together by a display device, these color channels will produce similar color-sensation of the scene to a viewer. The problem of obtaining the HR color image from this LR color image comes as a natural extension to the problem in section 1.1.1. This problem benefits from the formulation in section 1.1.1. However, the correlation of information in the color channels needs to be utilized to the greatest extent. The proposed approach here deals with this correlation and also addresses the choice of a color space that is oriented towards the *human visual system* (HVS).

1.1.3 Regularized color filter array image up-sampling

This problem is of special interest because most commercial color CCD cameras use the color filter array sensor and it is believed that these will continue to exist in the market for some time. Unlike the sensor describing the problem in section 1.1.2 this sensor provides only a single color channel value (data) alternatively at each location of the LR image. The rationale behind using this technology is because it is much cheaper than the beam-splitter technology used in the sensor of the problem in section 1.1.2. This means that in total only one-third of the total color information is given in comparison to the case in section 1.1.2 for the three color channel type.

It is then required to obtain the other two-thirds of the color information only from the observations given. This problem is called demosaicking of the color filter array. There is a wide literature addressing this problem.

1.1.4 Regularized image sequence up-sampling

In this problem the sensor data is a full color image sequence representing time-varying imagery. The LR color images can be thought to be shots of the scene at uniform time steps. This sensor type is used with most video imaging systems. These LR images can contain different information about the scene if there exists relative motion between the scene objects and the imaging system. If these motions are reliably exploited and then the additional information is appropriately registered, a significant resolution gain will be evident in a produced HR image of the scene thought to be at a specific time instant. Approaches possessing these capabilities are called image-sequence super-resolution and are recently referred to as simply super-resolution. The success of these approaches heavily rely on the reliability of the motion estimation technique used to deduce the motions. Hence this problem can be classified into two groups: global motion and arbitrary motion field.

1.2 Motivation

Image magnification to achieve higher perceived resolution is a problem with many potential applications such as:

1. Law enforcement and surveillance applications where usually poor quality LR images are obtained from typical low-quality commercial interlaced video cameras or snapshots acquired in a non-ideal imaging environment. From these poor LR images it is required to have a better quality HR image with clearer details that enhance its use as evidence and to support crime scene analysis.

2. Broadcasting and entertainment applications where standards conversions from one sampling structure to another is always a demand. In cinema production the high quality cameras used have large size and weight. These cameras are not suitable for use in highly dynamic scenes and cannot be mounted in all locations. The current remedy to this problem is to acquire these scenes with high-quality video cameras, because they are lighter and easier to mount. However, the quality of video cameras is far behind that of cinematic counterparts. Then the demand is to use digital techniques to up-convert the spatial resolution and interpolate the temporal component of the acquired video sequence.

3. Printing applications, especially in the field of advertisement, where an HR image poster is to be printed from an acquired LR image. When the source LR image is acquired by a color filter array CCD digital camera and the poster size is typically larger than one square meter in area then the situation is problematic. The problems arise in the form of misalignment in the color boundaries of the objects and the grainy effects in the smooth regions of the printed poster.

4. Aerial and satellite imaging where it is often required to zoom in a specific region of interest in the LR image sequence physically acquired or to view details beyond the limit of the satellite imaging system resolution, which is currently around one sample per meter.

1.3 Thesis overview

Chapter 2 introduces the problem formally and discusses its ill-posed nature and the challenges in solving it. Some definitions and background material are also presented in the chapter. The chapter commences with a new formulation of the problem. This formulation is the first contribution of the thesis. It surveys the solution approaches to the problem and discusses some previous approaches that are considered to be the cur-

rent state-of-the-art. The chapter analyzes the drawbacks of the solution approaches and the weaknesses of the discussed state-of-the-art approaches.

Chapter 3 introduces the proposed approach to address the weaknesses discussed before in chapter 2. Ingredients of the general formulation will be discussed. Background on the total-variation regularizer used is discussed. The solution method for this regularizer is derived.

Chapter 4 discusses one of the major contributions of the thesis which is the design of the first ingredient of the formulation, the observation model. A full chapter is reserved for this part because of its overarching nature in solving the two problems that the thesis addresses. The theory is derived, the design procedures are discussed, and several case studies are presented. A new concept introduced in this chapter, the theoretical camera is optimally designed in adaptation to the properties of the display device used. Its design theory is derived and some results are presented.

Chapter 5 presents the results for grey-scale image up-sampling and quantifies the parameters used in the experiments. The implementation algorithms are presented in a usable fashion. Results are provided and compared to other methods. The second part of this chapter introduces some aspects of the color spaces that are oriented toward the HVS. A contribution of the thesis which is the development of a new methodology that decouples the implementation color space from that of the formulation is discussed in the chapter. It is shown that the implementation can implicitly be executed in a perceptually uniform color space while the formulation is in the imaging system color space, for reasons discussed in the chapter.

Chapter 6 concludes the thesis by a summary of what has been presented. It lists the achieved contributions in this thesis. Finally, it provides some future directions for using the achieved contributions and extending the approaches developed to other closely related problems.

Chapter 2

Background

2.1 Definitions

Continuous real world scenes are acquired by an imaging system through projecting them by the optical component on to a plane and cropping to a cuboid $\mathcal{W}_T$ of size $\mathrm{W} \times \mathrm{H} \times \tau$, where $\mathrm{H} = 1$ ph, $\mathrm{W} = \mathrm{ar}$ ph, τ are the height, width, and the time interval respectively. The spatial unit of measure (ph) is the picture height and the aspect ratio $\mathrm{ar} = \frac{\mathrm{W}}{\mathrm{H}}$ [2]. In this thesis we are interested in this projected and cropped signal and consider it to be our starting point. This image will be denoted as $f_c(x, y, t) : \mathcal{W}_T \rightarrow \mathbb{R}$ when dealing with its grey scale form as luminance only imaging system. The variables x, y represent the spatial location on the plane and t represents the time parameter. Dealing with the full visual spectrum of light (colors), in the case of color imaging system, the signal is either split by a beam splitter for further filtering by different color filters or alternatively acquired by a color-filter-array. This will produce three values of the signal at each spatio-temporal location like the RGB values that are often used. In this case the continuous color signal can be written as a vectorial signal $\mathbf{f}_c(x, y, t) : \mathcal{W}_T \rightarrow \mathbb{R}^3$. For simplicity we can write also the spatio-temporal variables in vectorial form as $f_c(\mathbf{x})$ for grey scale and $\mathbf{f}_c(\mathbf{x})$ for color continuous image.

A continuous image $f_c(\mathbf{x})$ is acquired by a camera to produce a digital image $f[\mathbf{x}]$ as a function of discrete variables; the square brackets will be used to indicate this. Again, for the color image $\mathbf{f}_c(\mathbf{x})$ every color component is treated independently in the same manner producing the vector discrete image $\mathbf{f}[\mathbf{x}]$.

2.1.1 Sampling structure

A lattice (sampling structure) $\Lambda \in \mathbb{R}^D$, where $D = 2$ for still images and $D = 3$ for space-time images, is defined in terms of linear basis (column) vectors $\mathbf{v}_i$ as the set $\Lambda = \{n_1\mathbf{v}_1 + n_2\mathbf{v}_2 \cdots + n_D\mathbf{v}_D \mid n_i \in \mathbb{Z}, i = 1, 2, .., D\}$. Following the notation in [3], it can also be written in matrix form as $\Lambda = \mathrm{LAT}(\mathbf{V}_\Lambda)$ where $\mathbf{V}_\Lambda = [\mathbf{v}_1 \mid \mathbf{v}_2 \mid \cdots \mid \mathbf{v}_D]$. For example, a rectangular lattice for progressive video sampling with non-square pixels can be written as $\Lambda = \mathrm{LAT}(\mathrm{diag}(X, Y, T))$, where X, Y, T are the sampling period in the horizontal, vertical and temporal dimensions respectively. X, Y are measured in units of ph and T is measured in seconds. The unit-cell $\mathcal{P}_\Lambda$ of a lattice is that cell that when centered on every point of the lattice Λ will tile the space $\mathbb{R}^D$ with no overlapping. The volume of the unit-cell of a lattice Λ is given by $d(\Lambda) = |\det(\mathbf{V}_\Lambda)|$ [3].

The definition of a digital image $f[\mathbf{x}]$ is incomplete without defining its sampling structure. If $\mathbf{x} \in \Lambda$ and $f[\mathbf{x}]$ has finite energy, denoted by $f \in \ell^2(\Lambda)$, then the discrete space(-time) Fourier transform of $f[\mathbf{x}]$ over Λ is given by

$$F(\mathbf{u}) = \sum_{\mathbf{x}\in\Lambda} f[\mathbf{x}] \exp(-j2\pi\mathbf{u}\cdot\mathbf{x}), \quad \mathbf{u} \in \mathbb{R}^D. \tag{2.1}$$

It should be noted that the continuous space(-time) Fourier transform of $f_c(\mathbf{x})$ given by

$$F_c(\mathbf{u}) = \int_{\mathcal{W}_T} f_c(\mathbf{x}) \exp(-j2\pi\mathbf{u}\cdot\mathbf{x}) d\mathbf{x}, \quad \mathbf{u} \in \mathbb{R}^D \tag{2.2}$$

is aperiodic, as opposed to $F(\mathbf{u})$ which is periodic with a period of $\mathcal{P}_{\Lambda^*}$. This difference

arises from the fact that f_c is a continuous-space(-time) signal while f is discrete. $\mathcal{P}_{\Lambda^*}$ is a unit-cell of the lattice Λ^*, which is the reciprocal lattice of Λ, and is given by $\Lambda^* = \mathrm{LAT}((V_\Lambda^{\mathrm{T}})^{-1})$ [2]. Then the inverse Fourier transform of $F(\mathbf{u})$ is also given by

$$f[\mathbf{x}] = d(\Lambda) \int_{P_{\Lambda^*}} F(\mathbf{u}) \exp(j2\pi \mathbf{u} \cdot \mathbf{x}) d\mathbf{u}. \tag{2.3}$$

The sampling process $f[\mathbf{x}] = f_c(\mathbf{x}),\ \mathbf{x} \in \Lambda$, has an equivalent form in the frequency domain derived in [3] and is given by

$$F(\mathbf{u}) = \frac{1}{d(\Lambda)} \sum_{\mathbf{r} \in \Lambda^*} F_c(\mathbf{u} + \mathbf{r}). \tag{2.4}$$

It should be noted that all the Fourier transforms are given here in non-normalized form following the methodology developed by Dubois [3], thus $\mathbf{r} \cdot \mathbf{x} \in \mathbb{Z},\ \forall\ \mathbf{r} \in \Lambda^*,\ \mathbf{x} \in \Lambda$. For $D = 3,\ \mathbf{u} = [u, v, w]^{\mathrm{T}}$, while for $D = 2,\ \mathbf{u} = [u, v]^{\mathrm{T}}$, where u, v are the horizontal and vertical spatial frequencies and are measured in units of cycles/ph written as c/ph, and w is the temporal frequency measured as usual in units of Hz. The main rationale behind using non-normalized representation is to keep track of the geometry of the underlying sampling structure that will be used, especially when the sampling structure is non-square one.

The filtering process of a digital image $f \in \ell^2(\Lambda)$ by a digital finite-impulse-response (FIR) filter $h[\mathbf{x}],\ \mathbf{x} \in \Lambda$, is given by $g[\mathbf{x}] = h[\mathbf{x}] * f[\mathbf{x}]$, where $*$ denotes the D-dimensional convolution. The output image g will also be defined on the lattice Λ [3]. This process is given in the frequency domain as $G(\mathbf{u}) = H(\mathbf{u})F(\mathbf{u})$.

A lattice Γ is defined to be a *sublattice* of Λ if both of them have the same dimension and every point of Γ is also a point of Λ, written as $\Gamma \subseteq \Lambda$. Also Λ is called to be *superlattice* of Γ. This is true iff $(V_\Lambda)^{-1} V_\Gamma$ is an integer matrix [3]. The quantity

$d(\Gamma)/d(\Lambda)$ is called the index of Γ in Λ and is denoted by $(\Lambda : \Gamma)$ [3]. Then

$$\Lambda = \bigcup_{k=1}^{(\Lambda:\Gamma)} (\Gamma + \mathbf{c}_k), \quad k = 1, 2, \cdots, (\Lambda : \Gamma), \tag{2.5}$$

where $\mathbf{c}_k \in \Lambda$ are called the *coset representatives* of Γ in Λ. Also

$$\Gamma^* = \bigcup_{k=1}^{(\Lambda:\Gamma)} (\Lambda^* + \mathbf{d}_k), \quad k = 1, 2, \cdots, (\Lambda : \Gamma), \tag{2.6}$$

where $\mathbf{d}_k \in \Gamma^*$ are called the coset representatives of Λ^* in Γ^*. More details and notations can be found in [3].

2.1.2 Sampling of continuous images

The acquisition of images by the camera process used in this thesis is modelled as in [3]. The process is modelled ideally by filtering with a continuous-space(-time) low-pass prefilter followed by sampling on a lattice Λ. This thesis will refer to these two processes as the camera model. The prefilter will be referred to as the camera aperture whose impulse response is denoted by $h_a(\mathbf{x})$. The prefilter is used to reduce the effects of aliasing by trying to band-limit the input image $f_c(\mathbf{x})$, as known from the theory of digital signal processing. After sampling on Λ we obtain the discrete image $f[\mathbf{x}]$. By (2.4) this camera process is written in the frequency domain as

$$F(\mathbf{u}) = \frac{1}{d(\Lambda)} \sum_{\mathbf{r} \in \Lambda^*} H_a(\mathbf{u} + \mathbf{r}) F_c(\mathbf{u} + \mathbf{r}). \tag{2.7}$$

In practice $h_a(\mathbf{x})$ is governed by the physical realization of the camera aperture. Since the signal here is light and negative light is not defined, then the aperture function $h_a(-\mathbf{x})$ should be in practice a non-negative one. This eliminates the choice of the sinc function which is the impulse response of the ideal low-pass filter. The commonly

known practical models for the aperture function $h_a(-\mathbf{x})$ are:

1. The Gaussian function as in tube-type cameras.
2. The rect (box) function as in CCD cameras.
3. The circ (circular) function modelling the out-of-focus imaging.

Then practically the frequency response $H_a(\mathbf{u})$ will have a wide frequency profile. Consequently the filtering process by $H_a(\mathbf{u})$ does not perfectly confine the spectrum $F_c(\mathbf{u})$ to a unit-cell $\mathcal{P}_{\Lambda^*}$; then it is clear that in this case the summation in (2.7) will contribute spectral overlap in every $\mathcal{P}_{\Lambda^*}$. This is known as aliasing which in non-avoidable with practical cameras.

2.1.3 Reconstruction by display devices

A digital image like $f[\mathbf{x}]$ is useful for storage, transmission, and processing but in order for it to be viewed, it needs to be reconstructed back to a continuous image $\tilde{f}_c(\mathbf{x})$. Continuous images are the suitable form for viewing images by humans, which should not be mixed with the digital form of an image. The tilde superscript used here is to denote and emphasize that the reconstructed image is not perfectly the same as the original $f_c(\mathbf{x})$. Indeed, $f[\mathbf{x}]$ is suffering from aliasing, as discussed in section 2.1.2. A display device can be characterized by an analog function $\phi_{\text{dis}}(\mathbf{x})$ called the display aperture. The space $\mathbf{V}(\phi_{\text{dis}})$ is the space of all images that can be produced by this display device. This display device aperture function ϕ_{dis} acts as an analog interpolator for $f[\mathbf{x}]$. The samples $f[\mathbf{x}]$ here act as the coefficients for this reconstruction process. The reconstructed image $\tilde{f}_c(\mathbf{x})$ is given by

$$\tilde{f}_c(\mathbf{x}) = \sum_{\mathbf{d}\in\Lambda} f[\mathbf{d}] h_{\text{dis}}(\mathbf{x}-\mathbf{d}),\ \forall\ \mathbf{x} \in \mathcal{W}_T, \tag{2.8}$$

where the impulse response $h_{\text{dis}}(\mathbf{x}) = \phi_{\text{dis}}(\mathbf{x})$. This means that the term $\tilde{f}_c(\mathbf{x})$ is incomplete without specifying the associated $\mathbf{V}(\phi_{\text{dis}})$ because $f[\mathbf{x}]$ will have non-identical reconstructed images that depends on the display device. ϕ_{dis} is governed by physical realization constraints (electro-magnetic, chemical,... etc). Hence, $h_{\text{dis}}(\mathbf{x})$ cannot be an ideal low-pass filter whose passband is confined to the unit-cell $\mathcal{P}_{\Lambda^*}$ which includes $\mathbf{u} = \mathbf{0}$. This results in $\tilde{F}_c(\mathbf{u})$ that contains a non-negligible portion of the spectral replicas of $F(\mathbf{u})$.

I would like to emphasize the following, that is sometimes overlooked in the literature: *it is impossible to perfectly reconstruct* $\tilde{F}_c(\mathbf{u}) = F_c(\mathbf{u})$ *and it is improper to assume that* $F_c(\mathbf{u})$ *is band-limited for natural images acquired by physical digital imaging system whose aperture impulse response is modelled by* $h_a(\mathbf{x})$ *because:*

1. $F_c(\mathbf{u})H_a(\mathbf{u})$ *is not confined to a unit-cell of the reciprocal lattice of the imaging system.*

2. *Consequently and by (2.7),* $F(\mathbf{u})$ *has spectral overlap (aliasing).*

3. *Practically, the passband of* $H_{dis}(\mathbf{u})$ *cannot be confined to* $\mathcal{P}_{\Lambda^*}$ *located at* $\mathbf{u} = \mathbf{0}$ *so* $\tilde{F}_c(\mathbf{u})$ *contains some of the spectral replicas of* $F(\mathbf{u})$.

2.1.4 Image up-sampling

A complete treatment of the ideal process of sampling rate conversions for images can be found in [3]. The process of up-sampling an image $f_2[\mathbf{x}],\ \mathbf{x} \in \Gamma$ to a superlattice Λ is shown in Fig. 2.1. The process consists of two stages. The first is zero-insertions, such that $q[x] = \begin{cases} f_2[\mathbf{x}] & \mathbf{x} \in \Gamma; \\ 0 & \mathbf{x} \in \Lambda \setminus \Gamma. \end{cases}$ In the frequency domain this implies $Q(\mathbf{u}) = F_2(\mathbf{u})$. Since $q[\mathbf{x}]$ is defined for $\mathbf{x} \in \Lambda$ then $Q(\mathbf{u})$ is periodic with period of $\mathcal{P}_{\Lambda^*}$ and not $\mathcal{P}_{\Gamma^*}$ as it possesses after this stage. Then, it is required to filter out the undesired spectral replicas that exists in $\mathcal{P}_{\Lambda^*} \setminus \mathcal{P}_{\Gamma^*}$. Second, is to interpolate (filter) by $h[\mathbf{x}]$

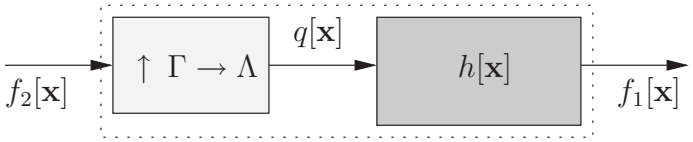

Fig. 2.1 Image up-sampling.

whose *ideal* frequency response is $H(\mathbf{u}) = \begin{cases} (\Lambda : \Gamma) & \mathbf{u} \in \mathcal{P}_{\Gamma^*}; \\ 0 & \mathbf{u} \in \mathcal{P}_{\Lambda^*} \setminus \mathcal{P}_{\Gamma^*}, \end{cases}$ in order to cut-off the undesired spectral replicas in $Q[\mathbf{u}]$. The index $(\Lambda : \Gamma)$ is also equal to the up-sampling factor. It should be noted that $H(\mathbf{u})$ is periodic with period $\mathcal{P}_{\Lambda^*}$. Both images $f_1[\mathbf{x}], f_2[\mathbf{x}]$ are then related to each other in the frequency domain by

$$F_1(\mathbf{u}) = \begin{cases} (\Lambda : \Gamma) F_2(\mathbf{u}) & \mathbf{u} \in \mathcal{P}_{\Gamma^*}; \\ 0 & \mathbf{u} \in \mathcal{P}_{\Lambda^*} \setminus \mathcal{P}_{\Gamma^*}. \end{cases} \tag{2.9}$$

In this ideal case the impulse response of $h[\mathbf{x}]$ is assumed to be a discrete sinc function. The practical sinc function can not have an infinite number of coefficients, but the underlying image $f_2[\mathbf{x}]$ is suffering from aliasing as discussed in section 2.1.2. These result in an image $f_1[\mathbf{x}]$ suffering from terrible ringing and undesirable artifacts. The sinc interpolation is not recommended in image up-sampling and other filters are used in practice. Different practical choices for the filter $h[\mathbf{x}]$ are the zero-order-hold (ZOH), linear, and cubic interpolators. These filters try to minimize the spectral leakage at the expense of a wider main lobe compromising resolution which is perceived as blur. The design of a good filter $h[\mathbf{x}]$ is always a trade off between blur and ringing in the up-sampled image $f_1[\mathbf{x}]$. This blur is acceptable if the goal is just to increase the size of the image but when a better perceived resolution is also required then better approaches that are capable of synthesizing high frequency contents are needed.

2.1.5 Image down-sampling

The process of ideal down-sampling of an image $f_1[\mathbf{x}], \mathbf{x} \in \Lambda$ to a sublattice $\Gamma \subseteq \Lambda$ as commonly treated in the literature is shown in Fig. 2.2. The process consists of two

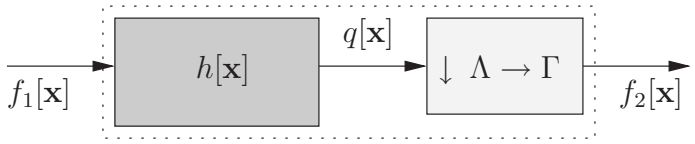

Fig. 2.2 Image down-sampling.

stages; first prefiltering by $h[\mathbf{x}]$. The *ideal* frequency response of this filter is given by

$$H(\mathbf{u}) = \begin{cases} 1 & \mathbf{u} \in \mathcal{P}_{\Gamma^*}, \\ 0 & \mathbf{u} \in \mathcal{P}_{\Lambda^*} \setminus \mathcal{P}_{\Gamma^*}. \end{cases}$$

$H(\mathbf{u})$ is periodic with a period of $\mathcal{P}_{\Lambda^*}$. The obtained intermediate image is written in the frequency domain as $Q(\mathbf{u}) = F_1(\mathbf{u})H(\mathbf{u}),\ \forall \mathbf{u} \in \mathbb{R}^D$. Second, is sub-sampling from Λ to Γ to obtain the down-sampled image $f_2[\mathbf{x}] \in \Gamma$. The relation between $F_1(\mathbf{u})$ and $F_2(\mathbf{u})$ can be derived in non-normalized form as follows;

$$f_2[\mathbf{x}] = d(\Gamma) \int_{\mathcal{P}_{\Gamma^*}} F_2(\mathbf{u}) \exp(j2\pi \mathbf{u} \cdot \mathbf{x}) d\mathbf{u},\ \mathbf{x} \in \Gamma. \tag{2.10}$$

Also,

$$q[\mathbf{x}] = d(\Lambda) \int_{\mathcal{P}_{\Lambda^*}} Q(\mathbf{u}) \exp(j2\pi \mathbf{u} \cdot \mathbf{x}) d\mathbf{u},\ \mathbf{x} \in \Lambda,$$

and using (2.6) we arrive at the relation

$$q[\mathbf{x}] = d(\Lambda) \sum_{k=1}^{(\Lambda:\Gamma)} \int_{\mathcal{P}_{\Gamma^*}} Q(\mathbf{u} + \mathbf{d}_k) \exp(j2\pi(\mathbf{u} + \mathbf{d}_k) \cdot \mathbf{x}) d\mathbf{u},\ \text{for } \mathbf{x} \in \Lambda.$$

Since, $\mathbf{d}_k \cdot \mathbf{x} \in \mathbb{Z}$ then we can write the expression for $q[\mathbf{x}]$ at the points of Γ as

$$q[\mathbf{x}] = d(\Lambda) \sum_{k=1}^{(\Lambda:\Gamma)} \int_{\mathcal{P}_{\Gamma^*}} Q(\mathbf{u} + \mathbf{d}_k) \exp(j2\pi \mathbf{u} \cdot \mathbf{x}) d\mathbf{u}, \ \mathbf{x} \in \Gamma. \tag{2.11}$$

Since $f_2[\mathbf{x}] = q[\mathbf{x}]$ at the points $\mathbf{x} \in \Gamma$, then equating (2.10) and (2.11) we arrive at the relation

$$F_2(\mathbf{u}) = \frac{1}{(\Lambda : \Gamma)} \sum_{k=1}^{(\Lambda:\Gamma)} Q(\mathbf{u} + \mathbf{d}_k).$$

If we Substitute for $Q(\mathbf{u})$, the down-sampling relation becomes

$$F_2(\mathbf{u}) = \frac{1}{(\Lambda : \Gamma)} \sum_{k=1}^{(\Lambda:\Gamma)} F_1(\mathbf{u} + \mathbf{d}_k) H(\mathbf{u} + \mathbf{d}_k). \tag{2.12}$$

It can be seen from (2.12) that unless $F_1(\mathbf{u}+\mathbf{d}_k)H(\mathbf{u}+\mathbf{d}_k)$ is confined to a unit cell $\mathcal{P}_{\Gamma^*}$ then the summation will contribute spectral overlap (aliasing) to the spectrum $F_2(\mathbf{u})$ in every $\mathcal{P}_{\Gamma^*}$. This can only be mitigated by the proper choice of a practical $H(\mathbf{u})$. A straightforward filter that can be used here is the Gaussian filter. The choice of the parameters of the Gaussian filter can be used as in [4]. Other desirable filters also exist, and we designed a new one in chapter 4 as well.

2.1.6 Arbitrary rate conversion

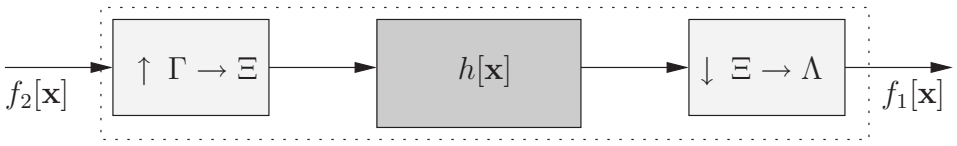

Fig. 2.3 Image arbitrary rate conversion.

Given $f_2[\mathbf{x}], \quad \mathbf{x} \in \Gamma$ it is desired to change its sampling structure to be Λ, where

neither Λ nor Γ are superlattice of the other. In this case we need a third intermediate lattice Ξ such that $\Lambda \subseteq \Xi$ and $\Gamma \subseteq \Xi$ analogous to rate conversion with rational factor in 1-D signal processing. The common superlattice Ξ with least density would be $\Xi = \Lambda + \Gamma = \{\mathbf{x} + \mathbf{y};\ \mathbf{x} \in \Lambda, \quad \mathbf{y} \in \Gamma\}$ [3]. If Ξ is not a lattice, then we could slightly modify Λ so that $\Lambda + \Gamma$ becomes a lattice. The conversion process is shown in Fig. 2.3. First, zero-insertions are performed so that the image $f_2[\mathbf{x}]$ becomes defined on Ξ. The second step is to filter (interpolate) by $h[\mathbf{x}]$. Here $h[\mathbf{x}]$ simultaneously serves the role of the prefilter for the down-sampling process. Finally, the sub-sampling from the superlattice Ξ to the desired lattice Λ is performed. The filter $h[\mathbf{x}]$ should have its passband confined to the volume enclosed by $\mathcal{P}_{\Lambda^*} \cap \mathcal{P}_{\Gamma^*}$. The *ideal* frequency response of the filter is given by $H(\mathbf{u}) = \begin{cases} (\Xi : \Gamma) & \mathbf{u} \in \mathcal{P}_{\Lambda^*} \cap \mathcal{P}_{\Gamma^*}, \\ 0 & \mathbf{u} \in \mathcal{P}_{\Xi^*} \setminus (\mathcal{P}_{\Lambda^*} \cap \mathcal{P}_{\Gamma^*}). \end{cases}$
An illustration for a simple example can be seen in Fig. 2.4. In this example $V_\Gamma = \mathrm{diag}(X, 2X)$ and $V_\Lambda = \mathrm{diag}(2X, X)$. It is clear that the least dense lattice Ξ that contains both Γ and Λ is $\Xi = \Gamma + \Lambda$ whose matrix $V_\Xi = \mathrm{diag}(X, X)$. Fig. 2.4 shows a possible (Voronoi) unit-cell for each sampling structure. The passband $\mathcal{P}_{\Lambda^*} \cap \mathcal{P}_{\Gamma^*}$ of the filter $H(\mathbf{u})$ is hashed in the figure.

The practical implementation of sampling structure conversion discussed here is performed using the polyphase implementation. This is practically effective because the implementation will always be done at the lower rate sublattice. Indeed, there is no point in calculating products of the filter coefficients by zeros. In addition, it is a waste of computation power to calculate samples that will be discarded by the sub-sampling process. Several implementations of the polyphase for many sampling structures can be found in [5].

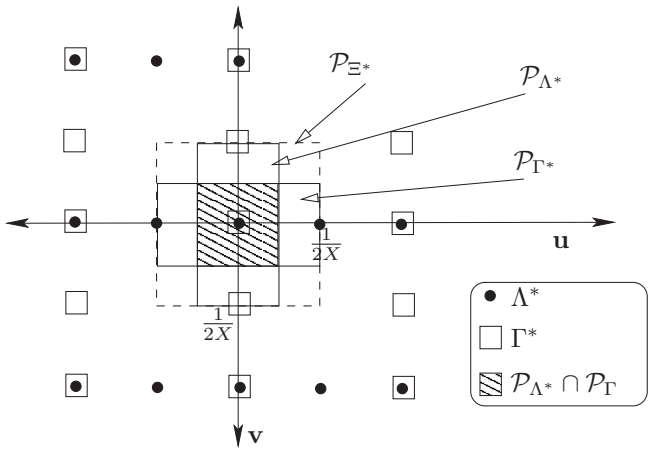

Fig. 2.4 Sample passband of $H(\mathbf{u})$.

2.2 Problem formulation

In this section I present a new formulation of the problem with a new perspective. This formulation is novel and considered to be the first contribution of this thesis. The problem formulation scenario for image magnification with higher perceived resolution is shown in Fig. 2.5. We are given a continuous space(-time) image $f_c(\mathbf{x})$ that has been acquired by a physical camera to produce a digital LR image $f_2[\mathbf{x}]$. This camera is modelled as in section 2.1.2 by filtering with a continuous space(-time) filter $h_2(\mathbf{x})$ then followed by an ideal sampling on Γ. The problem dealt with in this thesis is: *given the LR image(s)* $f_2[\mathbf{x}]$ *it is required to obtain the best perceived HR image representation defined on a denser sampling lattice* Λ. The new idea here is to assume that there exists a very high quality HR image $f_1[\mathbf{x}]$ defined on Λ that can be obtained directly from $f_c(\mathbf{x})$ by a virtual camera. This virtual camera can be modelled again as in section 2.1.2 by filtering with a continuous space(-time) filter $h_1(\mathbf{x})$ followed by an ideal sampling on Λ. It should be noted that $f_1[\mathbf{x}]$ is not given, and what we are seeking is a good estimate of it denoted by $\hat{f}_1[\mathbf{x}]$. Then formally the problem can be

phrased as: *given* $f_2[\mathbf{x}]$ *how can we obtain the best estimate* $\hat{f}_1[\mathbf{x}]$*?* "How" is the box labelled with the question mark shown in the Fig. 2.5. In the practical formulation of this problem in most of the literature, it is assumed that the physical camera aperture $h_2(\mathbf{x})$ is modelled by a rect function as in the CCD cameras. Then they assume that $h_1(\mathbf{x})$ should also be a rect function simulating the CCD camera process. The treatment of the problem in this thesis is different and sets a novel perspective for the problem formulation based on analyzing the following questions:

1. Why should we assume that $h_2(\mathbf{x})$ is a CCD camera modelled by a rect aperture? Here we assume it can be any model of existing physically realizable cameras such as the examples given in section 2.1.2.

2. Why should $h_1(\mathbf{x})$ be related by any means to $h_2(\mathbf{x})$? Furthermore, why should it model a physically realizable camera? Here we assume $h_1(\mathbf{x})$ can be any filter that need not necessarily be a model of a physically realizable camera and is independent of $h_2(\mathbf{x})$. In fact we will design $h_1(\mathbf{x})$, as will be shown later in the thesis, such that it defines nice properties of the HR image $f_1[\mathbf{x}]$.

This problem formulation scenario has opened a new research arena that addresses these problems. This will be shown specifically in:

1. Design of the theoretical camera aperture model $h_1(\mathbf{x})$ that it is adapted to the display device used ϕ_{dis}.

2. Partial answer to the question mark posed in this section by design of the accurate and correct observation model for any scenario $(h_1(\mathbf{x}), h_2(\mathbf{x}), \Lambda, \Gamma)$.

It should be noted that it is impossible to reconstruct $f_1[\mathbf{x}]$ from $f_2[\mathbf{x}]$ because a great amount of details and information that exist in $f_1[\mathbf{x}]$ are lost in $f_2[\mathbf{x}]$. However, we will try to obtain the best estimate $\hat{f}_1[\mathbf{x}]$

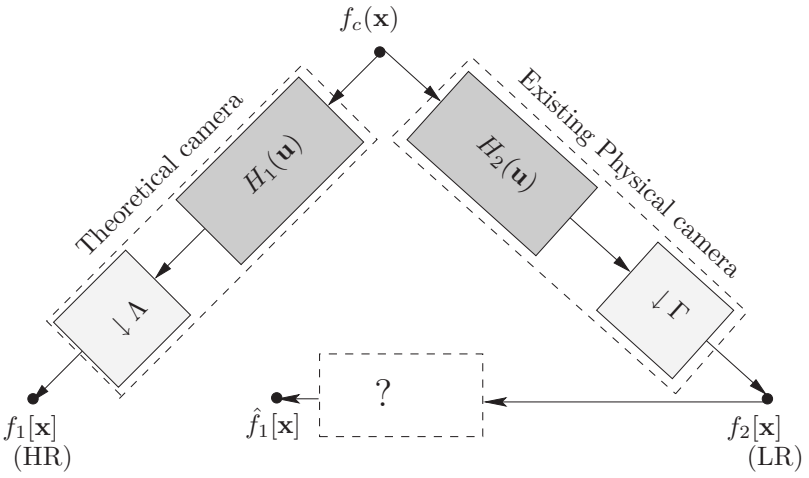

Fig. 2.5 Problem formulation scenario.

2.2.1 Ill-posed problem

According to the setup shown in Fig. 2.5, it can be shown that $f_2[\mathbf{x}]$ can be related to $f_1[\mathbf{x}]$ by down-sampling as given in 2.1.5 or generally by arbitrary rate conversion as given in 2.1.6 in the case of $\Gamma \nsubseteq \Lambda$. Without loss of generality, we will describe the case of $\Gamma \subseteq \Lambda$ because the other case will just precede by an up-sampling step to an intermediate super-lattice. A generalized derivation for this is given later in the thesis. A straightforward special-case setup for the scenario given in Fig. 2.5 was introduced in [6] and has been used continuously in most of the literature. They assumed that both $h_1(\mathbf{x})$ and $h_2(\mathbf{x})$ are rect (box) filters modelling the CCD cameras. In this case $f_2[\mathbf{x}]$ can be related to $f_1[\mathbf{x}]$ by an image down-sampling model as given in 2.1.5. Specifically, $f_2[\mathbf{x}]$ can be obtained from $f_1[\mathbf{x}]$ by filtering with a moving average filter followed by down-sampling from Λ to Γ. The moving average filter is obtained in this case because both $H_1(\mathbf{u})$ and $H_2(\mathbf{u})$ tiles each other in the frequency domain. This corresponds to averaging of the light collected by the HR sensors to obtain samples of the LR image $f_2[\mathbf{x}]$. Since the moving average pre-filter $h[\mathbf{x}]$ is LSI and the down-

sampling process is linear, but shift-variant, then both processes can be described by a linear system of equations. If we stack $f_1[\mathbf{x}]$ and $f_2[\mathbf{x}]$ into lexicographic column vectors, then we can describe the system by

$$\mathbf{f}_2 = H\mathbf{f}_1, \tag{2.13}$$

where H is a sparse matrix that combines both the filtering and the down-sampling process. Equation (2.13) is called the *observation model*. The number of rows of H is equal to the number of samples in $f_2[\mathbf{x}]$ and the number of columns is equal to the number of samples in $f_1[\mathbf{x}]$. It is clear that H has a nonempty null space $\dim(\text{Null}(H)) > 0$ [7]. This means that all the components of $f_1[\mathbf{x}]$ that lie in $\text{Null}(H)$ will not be observed in $f_2[\mathbf{x}]$. These components are the high frequencies in $F_1(\mathbf{u})$ that are perceived as fine details. Since our problem here is to obtain $\hat{f}_1[\mathbf{x}]$ from $f_2[\mathbf{x}]$, we want to "undo" the transformation given by (2.13). This is called mathematically an inverse problem. Hadamard [8] defined a problem to be well-posed if there *exists* a solution for it that is *unique* and depends *continuously* on the data. In our case here the *uniqueness is violated*; indeed, many different images $f_1[\mathbf{x}]$ can produce the same $f_2[\mathbf{x}]$ using (2.13) because when these differences lies in $\text{Null}(H)$ they will not appear at all in $f_2[\mathbf{x}]$. This classifies our problem as an *ill-posed* inverse problem. This means that $\mathbf{f}_1$ cannot be obtained from $\mathbf{f}_2$ by using simple matrix inversion of H. Equation (2.13) describes an under-determined linear system that has an infinite number of inverse solutions for $\hat{\mathbf{f}}_1$. The remedy is to incorporate additional side knowledge about the problem in hand so as to select one from these infinite number of solutions. This knowledge is called *a priori* image information to convert the problem to be well-posed. It is the selection of these *a priori* constraints that differentiates one solution approach from the others, as shown in the next section.

2.3 Previous solution approaches

2.3.1 Linear methods: re-sampling an underlying continuous space

The basic idea here is to fit a continuous image on the samples of $f_2[\mathbf{x}]$ and then re-sample it to the denser sampling structure Λ. A reconstructed continuous image $\hat{f}_c(\mathbf{x})$ is dependent on the choice of an underlying (reconstructing) continuous function $\varphi(\mathbf{x})$. Then the reconstructed continuous image $\hat{f}_c(\mathbf{x})$ becomes

$$\hat{f}_c = \sum_{\mathbf{d}\in\Gamma} c[\mathbf{d}]\varphi(\mathbf{x}-\mathbf{d}) \quad \forall \mathbf{x} \in \mathcal{W}_T, \tag{2.14}$$

where $c[\mathbf{x}]$ are the reconstruction coefficients that are derived from $f_2[\mathbf{x}]$ such that $\hat{f}_c(\mathbf{x}) = f_2[\mathbf{x}] \quad \forall \mathbf{x} \in \Gamma$. Under this framework many methods are realized, such as:

- Reconstruction by sinc function (Shannon's sampling theory);
- Linear interpolation;
- Spline based interpolation;
- Wavelet based interpolation.

Inspired by 1-D signal processing, the sinc interpolator is the optimal reconstruction function, in the least-squares sense, if the underlying LR image $f_2[\mathbf{x}]$ was obtained from $f_c(\mathbf{x})$ by bandlimiting its spectrum $F_c(\mathbf{u})$ to a unit cell $\mathcal{P}_{\Gamma^*}$ using an ideal low-pass filter. Then we can obtain $\hat{f}_c(\mathbf{x})$ by setting $\varphi(\mathbf{x}) = \mathrm{sinc}(V_\Gamma \mathbf{x})$[1] and $c[\mathbf{d}] = f_2[\mathbf{d}],\ \forall\ \mathbf{d} \in \Gamma$. The HR image $\hat{f}_1[\mathbf{x}]$ is obtained by an ideal sampling of $\hat{f}_c(\mathbf{x})$ on Λ. This is equivalent to the image up-sampling method described in 2.1.4 with the implementation of the filter $h[\mathbf{x}]$, as in Fig. 2.1, to become a discrete sinc function. The results obtained using this setup is shown in Fig. 2.7(b) where the original image $f_2[\mathbf{x}]$, shown

[1] Here, the vector argument of a function means separability; $\mathrm{sinc}(\mathbf{x}) = \prod_{i=1}^{D} \mathrm{sinc}(x_i)$, where $x_i,\ i = 1, \cdots D$ are the components of the vector $\mathbf{x}$.

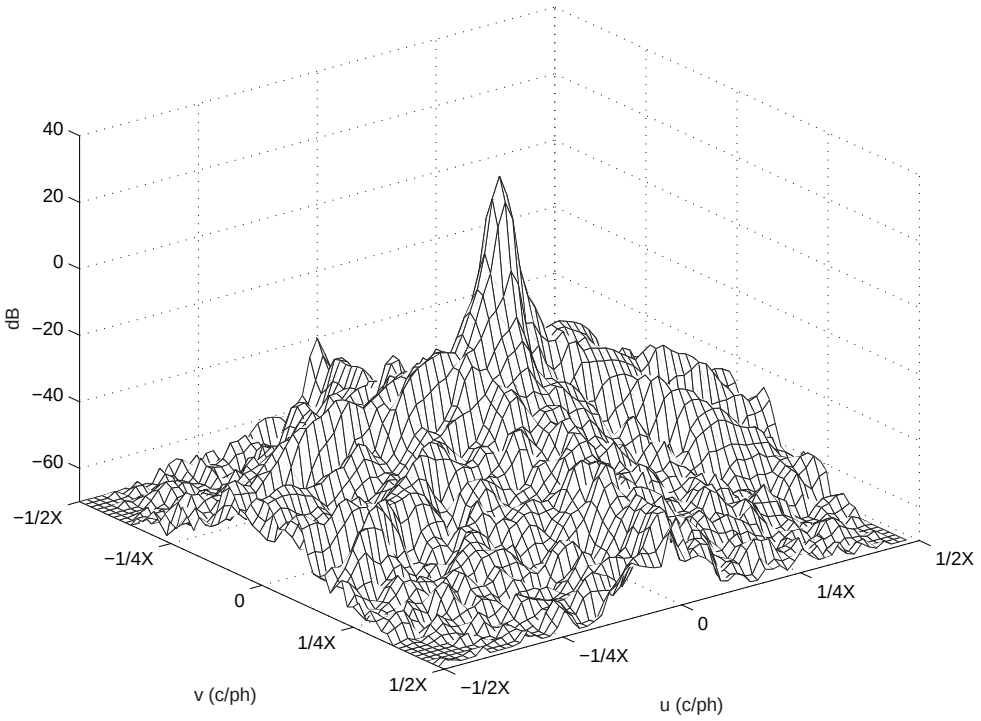

Fig. 2.6 Spectrum of the image in Fig. 2.7(a)

in Fig. 2.7(a), is up-sampled by a factor of 25 (5 in each direction) from orthogonal to orthogonal sampling structure. The implementation of this process was performed in the frequency domain, because the sinc function has infinite-impulse-response (IIR), as follows. First, zero samples were inserted to redefine the image on Λ and then the discrete Fourier transform (DFT) was calculated. This is followed by ideal low-pass filtering to eliminate all the spectral replicas. Finally, the image was converted back to the spatial domain using the inverse DFT. The result shown in Fig. 2.7(b) is not useful and suffers from severe ringing artifacts. This is expected because $f_2[\mathbf{x}]$ has a spectrum that is non-negligible at the border of a unit-cell of $\mathcal{P}_{\Gamma^*}$ as shown in Fig. 2.6. The power spectral density (PSD) of the image in Fig. 2.7(a) is plotted in Fig. 2.6. This PSD is estimated using the Welch-modified periodograms method [9] with a Blackman-Harris window [10]. With the PSD estimate plotted in the figure, a sharp cut-off by an ideal-low pass filter for interpolation will introduce very sharp frequency transition inside the band $\mathcal{P}_{\Lambda^*}$ and not at its border. Specifically, this sharp frequency transition will be at the location of the border of $\mathcal{P}_\Gamma$ in $\mathcal{P}_\Lambda$. In other words, it can be thought as the proportion of how $\mathcal{P}_\Gamma$ compares to $\mathcal{P}_\Lambda$. This in-band sharp frequency transition has the effect of introducing these oscillations seen all over the resulting image and being very obvious in the smooth regions.

The other most straightforward and least complex methods for solving the problem are the linear models. The reconstruction coefficients are set to be $c[\mathbf{x}] = f_2[\mathbf{x}]$, $\forall\, \mathbf{x} \in \Gamma$. They are commonly used and are implemented directly to represent $h[\mathbf{x}]$ as [11]:

- Zero-order-hold (pixel repeat), where φ is assumed to be piecewise constant. The result is shown in Fig. 2.7(c).
- Bilinear, where φ is assumed to be piecewise linear. The result is shown in Fig. 2.7(d).
- Bicubic, where φ is assumed to be a cubic polynomial [12]. The result is shown in Fig. 2.7(e).

The assumption here is that $f_2[\mathbf{x}]$ is free from aliasing and therefore there will be no attempt to extrapolate its spectrum when up-sampling to $\hat{f}_1[\mathbf{x}]$. Based on this assumption one is not hoping to obtain any perceived resolution gain in the magnified image. The linear approaches answer the question on how to obtain $\hat{f}_1$ from f_2 by simply using the image up-sampling method described in 2.1.4. Generally many underlying functions φ can be used which affect the results. The linear interpolation which characterizes this class is known for its inability to produce any new information. This is because this linear class assumes that the LR image samples f_2 completely represent the original continuous image f_c. In other words, f_c is assumed to be a bandlimited signal that has been sampled above the critical Nyquist rate to produce the samples $f_2[\mathbf{x}]$. The results in Fig. 2.7 are not satisfactory and are suffering from undesirable artifacts. These artifacts are perceived as

- staircasing (blocking) of oblique edges;
- blurring of the object boundaries and texture;
- ringing in the smooth regions and closer to the edges.

Another candidate of this class is embedding in spline spaces. A special case of the general splines for up-sampling by powers of 2 can be done in wavelet underlying domain. The splines [13] are usually determined by the basis $\varphi(\mathbf{x}) = \sum_{\mathbf{d}\in\Gamma} p[\mathbf{d}]\beta^n(\mathbf{x}-\mathbf{d})$ whose translations by $\mathbf{d} \in \Gamma$ form the spline Riesz basis [14]. β^n is the basic B-spline of order n and $p[\mathbf{d}]$ are the coefficients of the generating sequence. When $p[\mathbf{k}] = \delta[\mathbf{k}]$ then we obtain the basic B-splines, where $\delta[\cdot]$ is the Kronecker delta. The continuous image $\hat{f}_c$ is formed as in (2.14). The coefficients $c[\mathbf{x}]$ become control points (knots) to guide the interpolation. With the proper choice of $c[\mathbf{x}]$, then $\hat{f}_c$ can be constrained to pass through (interpolate) the samples of $f_2[\mathbf{x}]$. This is achieved as in [15] by the filtering $c[\mathbf{x}] = \mathring{\varphi}[-\mathbf{x}] * f_2[\mathbf{x}]$, where $\mathring{\varphi}$ is the dual basis of φ. This can be implemented by an IIR filter which has a number of poles dependent on the order n

(a)

(b)

(c)

(d)

(e)

Fig. 2.7 Up-sampling of (a) a portion of the cameraman image by a factor of 25 (5 in each dimension) using some linear interpolators; (b) sinc, (c) zero-order-hold, (d) bilinear, (e) bicubic.

of the B-splines. This pre-filtering has the effect of sharpening the image $f_2[\mathbf{x}]$ before interpolation. The spline family tries to ensure higher-order geometrical continuity of the data to produce homogeneous results. In the case of the basic cubic B-splines (β^3) interpolation, the second order derivatives of $\hat{f}_c$ are ensured to be minimum, which is equivalent to minimum curvature. However, the first order derivatives are not constrained. Another type of splines can be formed in a least-squares approximation sense called *smoothing splines*[13]. These minimize $\sum_{\mathbf{d}\in\Gamma}\left(\hat{f}_c(\mathbf{d}) - f_2[\mathbf{d}]\right)^2$ rather than enforcing $\hat{f}_c$ to pass through $f_2[\mathbf{d}]$, $\forall\mathbf{d}\in\Gamma$, while essentially minimizing the $(\frac{n+1}{2})^{\text{th}}$ order derivatives of $\hat{f}_c(\mathbf{d})$. This can be seen as a regularized least-squares problem that tends to minimize the oscillations around the edges. Sample results for the same image given in Fig. 2.7(a) using the cubic B-splines and the cubic smoothing splines are shown in Fig. 2.8(a) and Fig. 2.8(b), respectively. Another example is shown in Fig. 2.9 with the cubic B-splines and the smoothing splines of order 5. The results show slight enhancement over the previous interpolators. A variant presented in [16] that use a combination of β^3 and β^1 in generating φ was used for interpolating image rotations. It needs to work in conjunction with an edge-detector. The experiments for applying the approach were performed by the authors for image rotations only and was not tested for image up-sampling. Generally, splines are known to produce oscillatory edges with significant ringing near them. This is because splines enforce constraints at $\hat{f}_c(\mathbf{d})$, $\forall\mathbf{d}\in\Gamma$, and leave the rest to the smoothing regularizer ($(\frac{n+1}{2})^{\text{th}}$ order derivatives of $\hat{f}_c(\mathbf{d})$). Another analysis of these effects based on image isophotes (iso-intensity contours) can be found in [17].

In the same spirit of smoothing splines (by not enforcing interpolation of the samples of $f_2[\mathbf{x}]$), a recent variant to bilinear interpolation is given in [1]. They elected, based on theoretical analysis, not to interpolate the samples of $f_2[\mathbf{x}]$ but rather samples at sub-pixel shift of Γ. This is akin to sharpening $f_2[\mathbf{x}]$ before performing the bilinear interpolation. Though the method might provide enhancement up to the limit

of bicubic interpolation for smooth regions it provides worse results near edges. The same artifacts of this class are still evident in the result shown in Fig. 2.10.

This class performs the job in a blind fashion regardless of the image features and consequently the results have undesirable artifacts. The artifacts of this class are the results of the contradiction in the assumption about $F_2(\mathbf{u})$ that it is obtained with no aliasing and the reality that $f_2[\mathbf{x}]$, being acquired by a physical camera, has significant aliasing as discussed in section 2.1.2. This means that there is hidden (aliased) finer-detail information in $f_2[\mathbf{x}]$. This observation stimulates research to develop methods that can make use of these hidden finer details to reconstruct a better image $\hat{f}_1[\mathbf{x}]$. There are many enhancements that can be done by careful analysis and understanding of the problem as will be shown in some of the other classes, and the proposed approach in this thesis.

2.3.2 Adaptive Interpolation

Motivated by the drawbacks of the linear class, research in adaptive methods has become common. The goal of this class is to preserve the sharpness of edges in the up-sampled image $\hat{f}_1[\mathbf{x}]$. Achieving this goal leads to an HR image with a better perceived quality than those produced by the linear methods. Indeed, the significant difference is in mitigating the effects of the blurring of edges and their staircasing on the visual quality. Preserving the sharpness of edges corresponds to synthesizing new high frequency components in $\hat{F}_1(\mathbf{u})$ beyond that of its counterpart in $F_2(\mathbf{u})$. The basic concept of this class is to interpolate *along* the edges and avoid interpolating *across* them. The situation is depicted in the frequency domain in Fig. 2.11. In the figure a sample edge with a specific spatial orientation is superimposed on the profile of the frequency spectrum. We can think of edges as step functions (sharp transitions) with a specific orientation, let us assume it to be oriented along the vertical spatial axis. In the frequency domain this edge can again be superimposed on the vertical frequency

(a)

(b)

Fig. 2.8 Up-sampling of a portion of the cameraman image by a factor of 25 (5 in each dimension) using spline bases; (a) cubic B-spline, (b) cubic smoothing-spline.

(a)

(b)

(c)

Fig. 2.9 Up-sampling of (a) a portion of the tripod in the cameraman image by a factor of 25 (5 in each dimension) using spline bases; (b) cubic B-spline, (c) smoothing-spline of order 5

Fig. 2.10 Up-sampling of a portion of the cameraman image by a factor of 25 (5 in each dimension) using the method in [1].

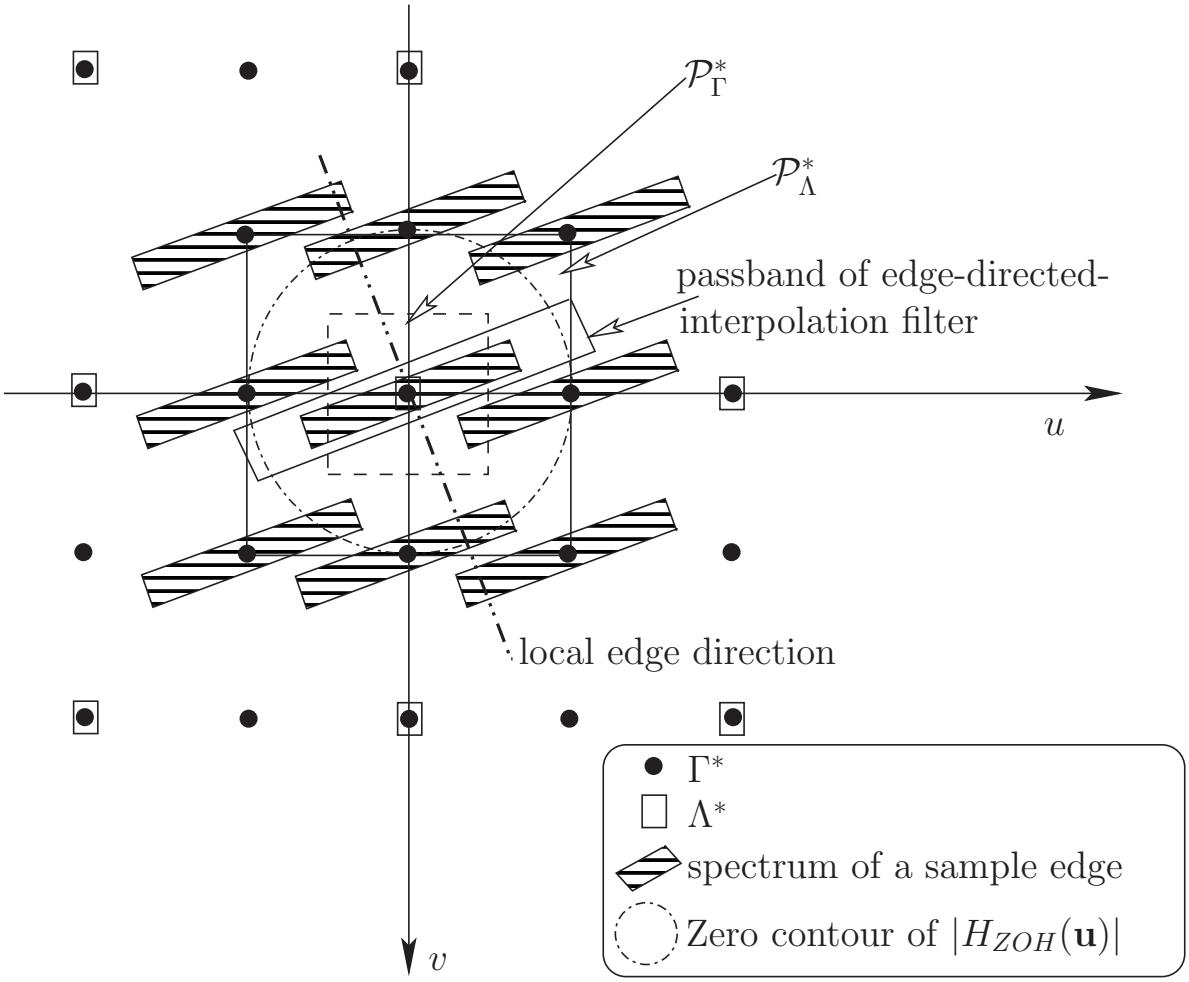

Fig. 2.11 Sample edge-directed interpolation.

axis; for illustration. Then the orientation of the profile of the frequency spectrum of an edge will be orthogonal to the spatial edge orientation. If an edge rotates in the spatial domain by an angle θ, this rotation is represented by a simple rotation matrix $A = \begin{pmatrix} \cos(\theta) & -\sin(\theta) \\ \sin(\theta) & \cos(\theta) \end{pmatrix}$ and the new edge image becomes $f_r(\mathbf{x}) = f(A\mathbf{x})$. The impact of this rotation in the frequency domain is that $F_r(\mathbf{u}) = \frac{1}{|\det A|} F(A^{-\mathrm{T}}\mathbf{u})$. Since, in this case $|\det A| = 1$ and $A^{-\mathrm{T}} = A$, therefore the profile of the spectrum will be exactly rotated in the frequency domain plane by the same angle θ. Then the orientation of the profile of the spectrum of an edge will be locally orthogonal to its orientation. The figure shows how linear interpolators like ZOH, bilinear, or of higher order introduce artifacts due to inclusion of undesired spectral replicas from adjacent unit cells. The situation is severe for diagonal edges. The figure shows how a locally edge-directed (directionally oriented) filter can compactly include all the spectrum of the edge (no blurring) without including any portion of the adjacent spectral replicas (staircasing and ringing). In other words, design requirements of the edge-directed interpolation filter are:

- Flat passband across the edge to avoid loss of resolution (blur) and maintain the edge sharpness. A directional maximally-flat filter will provide good results here. The most straightforward candidate filter here is the ZOH because it has a flatter passband compared to the linear and cubic filters.

- Sharp decay along the edge to avoid the inclusion of spectral replicas that introduce artifacts like staircasing and ringing. The straightforward filter here is the cubic one because it has a sharper transition region compared to ZOH and the linear filter.

The idea can be extended to all edges at all locations, giving rise to a space-variant filter that is dependent on the underlying data and hence this class is adaptive (and thus nonlinear). This hypothesis, if perfectly implemented, will produce significant

improvements. This class of methods exploits local image features and uses them to determine the weight of the participation of each sample of $f_2[\mathbf{x}]$ in obtaining the samples of $\hat{f}_1[\mathbf{x}]$. Two important methodologies are followed:

1. Edge-directed interpolation, where edges are identified explicitly and then are used to guide the interpolation process.

2. Local features measure, where a metric of the matching of samples of $f_2[\mathbf{x}]$ with its neighbors is used to determine their weight in the interpolation process or even the interpolation method itself.

All the approaches of this class switch to simple linear methods in the smooth regions, so the basic difference between every method in this class is in how it deploys its technique at the edges. Since there is no unified theory on how to interpolate at the edges, every method has its own technique. The evaluation of the improvement in the results produced by each method is usually assessed subjectively by visualizing the images. There is no specific attempt by this class of methods to deal with textured regions. Usually they are not detected as sharp edges and hence they are dealt with as smooth regions. In this section I will identify some of the methods of this class and briefly describe their approach.

2.3.2.1 Edge-directed interpolation

In the edge-directed interpolation group, the method to explicitly identify the edges is the main distinguishing feature among them. In [18] edges are extracted from $f_2[\mathbf{x}]$ with sub-pixel accuracy using an approximation of the Laplacian-of-Gaussian filter. The calculated edge map is then quantized to the points of Λ. Allebach and Wong [18] were aware of the fact that the edge map can never be accurate so they pre-processed $f_2[\mathbf{x}]$ to obtain another slightly altered LR image that matches the edge map they obtained. They compute local statistics from some neighboring samples that are not

separated from the underlying sample by an edge. Those samples which do not agree with their edge-based statistics are replaced by the mean of the underlying local statistics. This alteration assures the convergence of their iterative algorithm and avoids having undesired artifacts near the edges. They proceed with bilinear interpolation in smooth areas. In the areas where there is an edge, the samples of $f_2[\mathbf{x}]$ on the other side of the edge with respect to the sample of $\hat{f}_1[\mathbf{x}]$ being interpolated are discarded. They are replaced by a weighted average of the other samples of $f_2[\mathbf{x}]$ which are not isolated from the sample being interpolated from $\hat{f}_1[\mathbf{x}]$ by any edge. The obtained HR image serves as an estimate for the next iteration. The HR image obtained is pre-filtered by a moving average filter and then down-sampled to Γ simulating the sensor of a CCD camera. The error between the down-sampled iterate and the modified original is used to update the (back projection) iterate. The procedure is repeated until convergence, which is reached quickly by this method. The up-sampled images obtained by this method is demonstrated in [18] to be better than the linear methods in section 2.3.1 in terms of edge-preservedness and the global sharpness of the image.

Biancardi, Cinque, and Lombardi [19] followed the same route but instead they used bicubic interpolation to identify the position of the zero-crossings to locate the edges. In the up-sampling stage they used polynomial interpolation of a degree proportional to the up-sampling factor. The polynomial is constrained to produce a specific value for the magnitude of the gradient at the exact location of the edge identified. This value is calculated to interpolate the values of magnitude of the gradient of the neighboring samples. A different approach was followed in [20]; they used the spatial gradient of $f_2[\mathbf{x}]$ to determine the direction of the iso-luminance edges, if any, that pass through the samples. Locally the iso-luminance elements are assumed to connect samples of $f_2[\mathbf{x}]$. This information is used to interpolate the up-sampled version between these connected samples along the iso-luminance lines. Across the iso-luminance elements, averaging is used and then an ad-hoc sharpening function is

used. However, the sharpened long edges became wavy. In the same spirit but in the frequency domain, [21] used a subband decomposition. The high frequency band is further decomposed into a discrete number of directional sub-bands at different orientations. Then these directional subbands are interpolated in a 1-D fashion along their orientations. Across the orientation; either pixel repeat or averaging is used based on the strength of the transition between the lines. All the up-sampled and interpolated sub-bands are merged to synthesize back an HR image $f_2[\mathbf{x}]$ as in a filter-bank decomposition/synthesis structure. In this method there is a discrete set of orientations, and hence edges which are not aligned to these orientations, as well as textures, are not handled properly. The method relies heavily on the directional filter properties to avoid aliasing in the decomposition stage. A simple method was developed by [22] where the sub-pixel edge positions were detected based on 1-D function and then this function was used to detect edges at a discrete set of orientations. Along these directions where edges exist, a weighted averaging is performed based on the position of the interpolated samples with respect to the edge position. The results suffer from staircasing at diagonally oriented edges. A variation is presented in [23] where the edge positions are computed from a bilinearly interpolated version of $f_2[\mathbf{x}]$ and the image is segmented into regions based on the edge map and the intensity of the samples. Interpolation is performed within each segment. Their result suffers from blotching artifacts. The advantage of this group is that it preserves some of the edges and thus the interpolated image looks better than with traditional linear techniques. Indeed, preserving the major structures in the interpolated image yields better looking images.

2.3.2.2 Interpolation by exploiting local correlation

The second group does not explicitly extract the edges but rather obtains a local metric that determines the local weight of each sample of $f_2[\mathbf{x}]$ in interpolating a sample of $\hat{f}_1[\mathbf{x}]$. The problem was analyzed in [24] by the dyadic (undecimated) wavelets,

sometimes called the scale space, and the authors observed that edges possess high correlation among their wavelet coefficients across the different scales. Their coefficients are large in the fine scale and decay with a fast rate in the coarser scales. Hence, edges can be identified by this observation and the logarithm of their coefficients were extrapolated from the coarse-to-fine scales to estimate newer high-frequency subbands. The original LR image $f_2[\mathbf{x}]$ serves as the low frequency subband. Then the extrapolated new subbands along with $f_2[\mathbf{x}]$ are used in a wavelet synthesis process to provide a HR image with double the size in each dimension. The idea of across-scale correlation was used by [25] but in the spatial domain. They used the idea for all the data and not only for edges. They first obtained a down-sampled version of the LR image and measured the correlation weights of the samples across them. Then they used the obtained correlation to compute the HR image from the LR image. This resulted in deteriorations in the textured regions because the idea holds for edges, as analyzed in [24]. The authors in [26] used the covariance to be the metric that determines in a certain window how close a sample of $f_2[\mathbf{x}]$ correlates to the others. Then a weight, set to be proportional to this correlation, is used in the interpolation. It is simple and does not rely on edge-detection accuracy but it fails to preserve small regions' edges. In [27] they used an ad-hoc weighting that is based on a non-linear combination of the neighboring sample intensities and their differences. Their method is only applicable for up-sampling by a factor of 2 in each spatial dimension. Based on the scale space and the Laplacian-Gaussian pyramids, [28] used a threshold to implicitly determine edges in the high frequency zones. They sharpened these edges in the fine scale level of the pyramid by a sharpening factor and then reformed the HR image $\hat{f}_1[\mathbf{x}]$. The method is dependent on the selection of the threshold and sharpening factor to work on a subset of the edges. A simple method in [29] used the interpolation weight of a sample to be inversely proportional to the sum of the absolute values of its spatial derivatives. This measure ignored the geometric properties of images and did not

consider the orientation of the gradient. The magnitude of the gradient usually offers a reasonable compromise in this issue. Their results were shown on synthetic images. The effectiveness on natural images was not judged. Finally, switching between different linear techniques in different locations based on their statistics is performed by [30]. They identify pixels to be belonging to smooth regions by linear filtering based on Bessel's formula, and then they interpolate them using cubic B-splines β^3. They identify how close samples are to an edge by using a gradient measure and a threshold in a window around the sample to be identified. If the sample is at a noticeable edge then zero-order-hold interpolation is used to avoid blurring. Otherwise extrapolation is performed by using linear filtering.

Adaptive methods produce clearly visible edges as compared to those produced by the linear class in section 2.3.1 which are usually blurry. This enhances the overall perceived quality of the produced images which is depicted in the frequency domain by extrapolation of the spectrum of $F_2(\mathbf{u})$ by using the edge information as illustrated in Fig. 2.11. However this class has the following drawbacks:

1. It relies on good edge estimation and every implementation is sensitive to the orientations of the edges. This means that some of the edges suffer from staircasing effects based on their orientation.

2. Despite the fact that the sharpness of the edges is being enhanced by these methods, the crispness of long edges is not well handled and usually we obtain wavy edges.

3. Ringing in the smooth regions closer to edges is still a problem.

4. Most of the methods are suited for up-sampling by factors of $2^i, i \in \mathbb{Z}^+$, in each dimension.

5. This class does not address how to deal with texture.

6. There is no solid theoretical base that unifies the realization of the approaches of this class and every approach stands on its own. This affects the possibility of extending the developed methods to tackle the remaining problems listed above.

2.3.3 Regularization-based image up-sampling

In section 2.2.1 we found that we are dealing with an inverse ill-posed problem. The observation model given by (2.13) is furthermore an ideal case of the reality. We should also consider the following:

- Different types of noise that contaminate the measurements like:
  - Shot noise, due to the sensor and the electronic elements involved;
  - Quantization noise, due to discretization of the measurements;
  - Random noise.
- Observation model uncertainty, due to the fact that we may not know whether the observation model with its filter $h[\mathbf{x}]$ is correct and accurate or not. This impacts the matrix H in (2.13). Nevertheless, this thesis tackles this uncertainty and one of its major contributions is to shed light on this particular part.

Accordingly (2.13) can be written as

$$\mathbf{f}_2 = H\mathbf{f}_1 + \eta, \tag{2.15}$$

where η represents noise representing the above mentioned noise perturbations. In this class of solution methods, the approaches formulate the problem by setting objectives. These objectives are the mathematical description of our knowledge about the problem in-hand. When achieved, these objectives lead to their desired optimal[2] goal $\hat{f}_1[\mathbf{x}]$. Our

[2] This optimal is in the sense of the specific objectives set. However, globally these objectives are not the optimal measure for the ideal HR image $f_1[\mathbf{x}]$, and hence $f_1[\mathbf{x}]$ is irrecoverable as discussed before in section 2.2.

first knowledge is represented in (2.15). Hence, a straightforward objective criterion is formulated in the classical least-squares sense as

$$\begin{aligned} \hat{\mathbf{f}}_1 &= \arg\min_{\breve{\mathbf{f}}_1} \mathcal{J}_d(\breve{\mathbf{f}}_1, \mathbf{f}_2), \\ \mathcal{J}_d(\mathbf{f}_1, \mathbf{f}_2) &= \frac{1}{2}\|H\mathbf{f}_1 - \mathbf{f}_2\|^2. \end{aligned} \tag{2.16}$$

This criterion is known as the *data fidelity* term[3] and is being extensively used as important part that constitute an objective function in most image restoration techniques. An optimization problem that is solely defined in terms of the data fidelity objective criterion will have an infinite number of solutions. It only measures data that lie in the vector space spanned by the columns of H. Hence, any optimization method will find the local minimizer to the initial estimate image for $\hat{\mathbf{f}}_1$. It is impractical to construct the matrix H (because it contains a huge number of elements) and to compute its singular value decomposition (SVD). Practically, iterative optimization methods are used to arrive at the minimizer of (2.16). The implementation is done with the basic image processing operations like convolution, up-sampling, and down-sampling. To illustrate the idea of the infinite number of solutions for (2.16), I used the gradient descent method to solve (2.16) with two different initial conditions. These initial images are chosen to be:

- random Gaussian noise image with a mean and a standard deviation equal to half of the grey scale range used[4],
- a zero (black) image

[3] This $\frac{1}{2}$ is just for convenience for later evaluation of the derivatives and has no impact on the objective criterion.

[4] The values that are generated outside the grey scale range are projected to the nearest value in the range

for solving the same up-sampling problem for the image in Fig. 2.7(a). Thus, I performed the experiment twice and obtained two up-sampled images that solve (2.16) starting with both initial guesses. The solution obtained for up-sampling using the Gaussian noise image as an initial condition is shown in Fig. 2.12, and the case of the zero image converged to the ZOH interpolation as in Fig. 2.7(c). This clearly illustrates that we obtained two different results that are very dependent on the choice of the initial condition (image). Hence, we are in a great need for side knowledge about the problem to convert it to be well-posed and to obtain a useful unique solution. The use of this side (*a priori*) knowledge is formally called regularization. Regularization

Fig. 2.12 Up-sampling of a portion of the cameraman image by a factor of 25 using (2.16) only with a random noise image as an initial guess.

can be thought of as any of these equivalent interpretations:

- Incorporating additional *a priori* knowledge about the problem.
- Converting an ill-posed problem to a well-posed one.

- Selecting one of the infinite number of solutions described by the data fidelity term.

Regularization has been used in most of the image processing problems like restoration, enhancement, motion estimation, magnification with better perceived resolution, etc. The use of various regularizers existed in other sciences. These were inherited by the image processing community and their use became popular due to their success. Indeed, many desirable properties and knowledge about the problem can be defined in terms of mathematical terms that interact together in an optimization problem. A survey of the most widely used regularizers in image processing problems can be found in [31]. Here we will provide a brief survey of the following regularization methods:

1. *Generalized inverse* known as the minimum energy estimate.
2. *C-Generalized inverse* known as the *Tikhonov* regularization.
3. Statistical approaches known as the *maximum a posteriori* (MAP) estimation.
4. *Variational* approaches that includes
    - Anisotropic diffusion.
    - Bounded-total-variation.
    - Mean-curvature evolution.

2.3.3.1 Generalized inverse

The theory of the generalized inverse incorporates the most straightforward regularizer which is the unique solution with minimum energy $\|\hat{\mathbf{f}}_1\|$. Thus the problem can be formulated as

$$\begin{aligned} \hat{\mathbf{f}}_1^{\dagger} &= \arg\min_{\mathbf{g}} \Big\{ \mathcal{J}_s(\mathbf{g}) \qquad \text{s.t } \mathcal{J}_d(\mathbf{g}, \mathbf{f}_2) = 0 \Big\}, \\ \text{where } \mathcal{J}_d(\mathbf{f_1}, \mathbf{f}_2) &= \|H\mathbf{f}_1 - \mathbf{f}_2\|^2, \qquad \mathcal{J}_s(\mathbf{f}_1) = \|\mathbf{f}_1\|^2. \end{aligned} \tag{2.17}$$

The generalized inverse solution $\hat{\mathbf{f}}_1^{\dagger}$ is known as the pseudo-inverse or the Moore–Penrose solution. The result $\hat{\mathbf{f}}_1^{\dagger}$ for image up-sampling can be obtained using the SVD. In restoration problems where both $\hat{f}_1$ and f_2 belongs to the same sampling structure the generalized inverse is not useful due to the introduction and amplification of noise by the very small singular values of H. A regularization method is to use only the singular values with sufficiently large values. This is called truncated SVD [32]. However in our problem of image up-sampling, the matrix H is full row rank [7]! This means that the generalized inverse can be used directly for the reconstruction of the HR image without having the introduction and amplification of spurious noise. The result of up-sampling using the pseudo-inverse is shown in Fig. 2.13, where $h[\mathbf{x}]$ is chosen to be a moving average filter. The original LR image, a portion of the cameraman, given in Fig. 2.13(a) is up-sampled by a factor of 25 and the result is shown in Fig. 2.13(b). The reason that the LR image used here is small is due to the memory requirement to store the matrix H which is huge in size and computing its SVD. In this specific example $f_2[\mathbf{x}]$ is of size 25×25 pixels, the associated H matrix for up-sampling by a factor of 25 is of size $625 \times 15625 = 9765625$! It is obvious that the result in this case is exactly the ZOH up-sampling. This result can be explained in terms of the generalized inverse as $\hat{\mathbf{f}}_1^{\dagger} = (H^{\mathrm{T}}H)^{-1}H^{\mathrm{T}}\mathbf{f}_2$. The matrix H represents a linear-shift-variant system as opposed to the restoration problems where H represents an LSI system. In the case of up-sampling, H is a block Toeplitz matrix with circulant blocks. For the special case of the moving-average prefilter, the structure of H can be exploited using the Kronecker product [7] and then it becomes straightforward to show that $H^{\mathrm{T}}H = I/(\Lambda : \Gamma)^2$, where I denotes an identity matrix. The solution is then $\hat{\mathbf{f}}_1^{\dagger} = (\Lambda : \Gamma)^2 H^{\mathrm{T}}\mathbf{f}_2$ which is the ZOH up-sampling. If we inspect $\mathcal{J}_s$ we find that it tries to find the estimate with the minimum energy. Although this is a very general objective criterion, it is not suitable for images. Generally, the spectrum of images bears a decaying exponential shape as shown in the sample of Fig. 2.6. Hence,

it is not wise to impose a minimum energy criterion with the same weight all-over the spectrum as the one specified by $\mathcal{J}_s$ in 2.17. In fact, the data fidelity criterion provides a good knowledge about $\hat{F}_1(\mathbf{u})$ in the band $\mathcal{P}_{\Gamma^*}$ so we want a regularizer that provides suitable knowledge that is focused on $\mathcal{P}_{\Lambda^*} \setminus \mathcal{P}_{\Gamma^*}$ without greatly affecting $\mathcal{J}_d$ in its band of operation. This can be achieved by a smoothness cost function $\mathcal{J}_s$ that has different weights within the spectrum of f_1.

(a)

(b)

Fig. 2.13 Up-sampling of (a) portion of the cameraman image by a factor of 25 using (b) the pseudo-inverse.

2.3.3.2 C-Generalized inverse

A well-known and widely-used regularizer is the Tikhonov regularizer, also called C-Generalized inverse. It defines the smoothness criterion as $\mathcal{J}_s(\mathbf{f}_1) = \|C\mathbf{f}_1\|_W^2$, where C can be a linear operator. W is a weighing matrix which usually incorporates knowledge about the noise statistics in the image. The common choice of W is then a diagonal matrix which can also be the identity matrix in the general sense of absence of any knowledge. According to the discussion about the drawbacks of the generalized inverse, a preferable choice of C is a high-pass operator. Hence, $\mathcal{J}_s$ will measure the energy of the high-frequency components in the spectrum. Imposing minimization of $\mathcal{J}_s$ here will provide a control on noise amplification and avoid the development of outlier

high-frequency patterns. Then the Tikhonov regularized image up-sampling becomes

$$\begin{aligned} \hat{\mathbf{f}}_1^{(\mathrm{Tik})} &= \arg\min_{\mathbf{g}} \Big\{ \mathcal{J}_d(\mathbf{g}, \mathbf{f}_2) + \lambda \mathcal{J}_s(\mathbf{g}) \Big\}, \\ \text{where } \mathcal{J}_d(\mathbf{f}_1, \mathbf{f}_2) &= \frac{1}{2}\|H\mathbf{f}_1 - \mathbf{f}_2\|^2, \qquad \mathcal{J}_s(\mathbf{f}_1) = \frac{1}{2}\|C\mathbf{f}_1\|_W^2, \end{aligned} \tag{2.18}$$

λ is a regularization parameter which establishes the trade-off between $\mathcal{J}_d$ (data fidelity) and $\mathcal{J}_s$ (smoothness of the solution). This optimization problem can be solved iteratively using a gradient descent method [33] as follows:

$$\hat{\mathbf{f}}_1^{(k+1)} = \Big[\hat{\mathbf{f}}_1 + \Delta\tilde{t} \Big(-\lambda C^{\mathrm{T}} W^{\mathrm{T}} W C \hat{\mathbf{f}}_1 - H^{\mathrm{T}} \big(H\hat{\mathbf{f}}_1 - \mathbf{f}_2 \big) \Big) \Big]^{(k)}. \tag{2.19}$$

The superscript (k) denotes the iteration number and $\Delta\tilde{t}$ is the artificial time step which is also known as the relaxation parameter. The convergence of iteration (2.19) is sensitive to the choice of $\Delta\tilde{t}$ which depends on the largest eigenvalue of H. An analysis for the choice of $\Delta\tilde{t}$ that ensures convergence for some basic regularizers can be found in [32]. A common choice of the high-pass filter represented by C that is used in image restoration and in super-resolution is the Laplacian filter (second-order derivative). The magnitude of the frequency response of the Laplacian filter is shown in Fig. 2.14. However, better high-pass filters can be designed which can offer a better match to the up-sampling factor $(\Lambda : \Gamma)$ and be well adapted to the nature of the volume $\mathcal{P}_{\Lambda^*} \setminus \mathcal{P}_{\Gamma^*}$. The result $\hat{\mathbf{f}}_1^{(\mathrm{Tik})}$ for the same up-sampling experiment of the image in Fig. 2.7(a) using (2.19) and $\lambda = 0.3$ is shown in Fig. 2.15. The result shown is not satisfactory and looks blurry everywhere. It is of comparable quality to that of the spline interpolation. This is natural because a high pass filter does not differentiate between noise and edges, they both are high frequency components. In this regularization $\mathcal{J}_s$ is a blind measure of the high frequency components. This results in blurred edges while minimizing the introduction of noise into $\hat{\mathbf{f}}_1^{(\mathrm{Tik})}$.

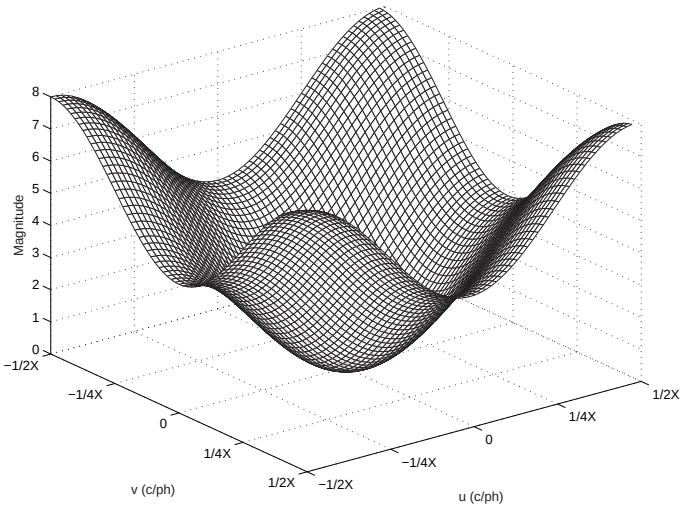

Fig. 2.14 Magnitude of the frequency response of a Laplacian filter over a unit-cell.

Fig. 2.15 Up-sampling of a portion of the cameraman image by a factor of 25 using the C-generalized inverse.

2.3.3.3 Statistical regularization

In an elegant paper, Geman and Geman [34] first used the *Markov random field* (MRF) in image restoration and thereafter it has been continuously used until now. The basic idea is that the conditional probability of the MRF is suitable to describe the local nature of the image objects and a pixel can be described in terms of a neighborhood around it. The Hammersley-Clifford theorem proved the equivalence of the MRF and the Gibbs (Boltzman) distribution. Hence, the Gibbs distribution is used as a practical generating distribution for MRF. Images are also characterized by sharp discontinuities, and these can be modelled in the Gibbs-MRF using line fields that describe edge crossings. In statistical regularized image up-sampling, the approach of Schultz and Stevenson is an important and successful one. They modelled the image as a realization of a random process, specifically MRF. They used the Huber function in modelling the clique potentials of the Gibbs-MRF, for the following reasons:

- The quadratic form in calculating the clique potentials is computationally desirable because it leads to a convex objective function that can be minimized with gradient descent methods. On the contrary, the edge-preserving potential using the line fields leads to non-convex objective that will require a costly stochastic optimization technique like graduated-non-convexity or simulated annealing. It should be noted that there are other MRF approaches that try to preserve edges while maintaining a convex objective function as in [35].

- To account for the quadratic penalty for edges, the Huber function switches from quadratic to linear when its argument reaches a certain threshold. Hence, the objective function will still be convex, all the while allowing edges to be part of the admissible solution.

The authors in [6] called the model as Huber-MRF (HMRF). They assumed that the image estimate $\hat{f}_1$ is a realization of a HMRF. They formulated a MAP estimation

problem that maximizes the conditional density, $\hat{\mathbf{f}}_1 = \arg\max_{\mathbf{g}} \log P(\mathbf{g} \mid \mathbf{f}_2)$. Using Bayes' rule, this MAP criterion was converted to a minimization problem as

$$\begin{aligned} \hat{\mathbf{f}}_1 &= \arg\min_{\mathbf{g}} \Big\{ \mathcal{J}_d(\mathbf{g}, \mathbf{f}_2) + \frac{1}{\lambda} \mathcal{J}_s(\mathbf{g}) \Big\}, \\ \text{where } \mathcal{J}_d(\mathbf{f}_1, \mathbf{f}_2) &= \frac{1}{2\sigma^2} \|H\mathbf{f}_1 - \mathbf{f}_2\|^2, \qquad \mathcal{J}_s(\mathbf{f}_1) = \sum_{c \in \mathfrak{C}_\Lambda} \mathcal{V}_c(\mathbf{f}_1). \end{aligned} \tag{2.20}$$

The regularization parameter λ was chosen to be the temperature parameter of the Gibbs distribution. $\mathcal{V}_c$ denotes the clique potential for a clique c in the clique system $\mathfrak{C}_\Lambda$ defined over Λ, and η in (2.15) is assumed to an identically distributed independent Gaussian noise with variance σ^2. They used a second-order neighborhood system and defined the potential in terms of the sum of all the Huber functions on its second-order derivative argument, calculated by the numerical central difference. Thus the clique potential at a specific clique c of $\mathfrak{C}_\Lambda$ is given by $\mathcal{V}_c(\mathbf{f}_1) = \sum_{m=0}^{3} \rho_T(d_m(\mathbf{f}_1, c))$, where ρ is the Huber function with its threshold ξ. The second-order derivative operator d_m is calculated at the four main orientations indexed by m using the central difference. All the terms are differentiable and this optimization problem is solved iteratively using a gradient descent method as follows:

$$\hat{\mathbf{f}}_1^{(k+1)} = \Big[\hat{\mathbf{f}}_1 + \Delta\tilde{t} \Big(-\nabla_{\hat{\mathbf{f}}_1} \mathcal{J}_s(\hat{\mathbf{f}}_1, \xi) - \frac{\lambda}{\sigma^2} H^{\mathrm{T}} \big(H\hat{\mathbf{f}}_1 - \mathbf{f}_2 \big) \Big) \Big]^{(k)}, \tag{2.21}$$

where $\nabla_{\hat{\mathbf{f}}_1}$ denotes the gradient of the associated criterion ($\mathcal{J}_s$). The results demonstrated by the authors in [6] provided enhancement over linear methods and Tikhonov regularization method and the Gaussian MRF. The edges produced in the resulting images are clear. This method was also extended by the same authors for super-resolution from image sequences which showed further success too. However, the drawbacks of the method are

1. It has three tuning parameters; λ, σ, and ξ that have to be adjusted to provide enhanced results for different images, which is considered to be an associated

difficulty with the method.

2. The choice of the Huber function for preserving edges proved to provide enhanced results but again the line fields are considered to be the best for edge-preservation with MRF. It is analogous to how edge-directed interpolation compares to linear interpolation. It should be noted that line-fields were used by [36] in the super-resolution up-sampling from a LR sequence.

3. The use of HMRF reduced the strength of MRF in modelling texture. Texture can be successfully modelled in MRF using the Ising model [34].

4. Steep edges with sharp transitions are still not fully modelled by HMRF.

Another approach using the MRF image model for image restoration was proposed by Bouman and Sauer in [35]. Their design goal was to define an edge-preserving MRF that yields a convex optimization problem. They proposed raising the clique potential to the power $1 < p < 2$ instead of setting $p = 2$ in most of the MRF approaches or using the Huber function that needs an ad-hoc choice of the Huber parameter ξ as in [6]. The advantages of their approach ($1 < p < 2$) are as follows:

1. The associated objective function is convex and can be minimized with gradient methods without the need of costly stochastic optimization methods;

2. It provides some ability to preserve edges as long as the value of p is close to 1.

The authors demonstrated the ability to preserve edges in the images restored by their approach. Their results were presented for synthetic images only, and we do not know the effectiveness of their approach for natural images. In section 3.2 I will analyze and discuss a claim that full edge-preservedness is achievable for the case when $p = 1$. However, the associated objective function becomes non-differentiable at the origin and more complicated mathematical tools like calculus of variations are needed to minimize this objective function.

MRF is a successful image model; this is due to the relevance of the conditional probability in modelling the local independence of pixels belonging to a region from other regions in natural images. The associated implementation difficulties are the need for a stochastic optimization method like simulated annealing to arrive at the global minimum and the need of training images to completely utilize the model, especially in modelling the normalization quantity of the energy of the Gibbs distribution.

2.3.3.4 Variational regularization

Perhaps the most interesting regularizer is the variational one. The variational regularizer has its roots in thermodynamics, diffusion and studies of the heat equation. Its application to image processing is witnessed by the following landmark papers:

1. Perona and Malik [37] used anisotropic diffusion in scale-space for edge detection;
2. Rudin, Osher, and Fatemi (ROF) [38] defined the total-variation regularizer for image denoising;
3. Alvarez, Lions, and Morel [39] who introduced evolution by mean curvature for image restoration.

Since then it has been a hot topic in image denoising, restoration, segmentation, motion estimation, computer vision, and up-sampling for the past decade. All of these formulations with different names are different forms of a unified functional variational regularizer which is given by

$$\mathcal{J}_s(\tilde{\hat{f}}_1) = \int_{\mathcal{W}_T} \mathfrak{L}\big(\|\nabla_{\mathbf{x}} \tilde{\hat{f}}_1(\mathbf{x})\|\big) d\mathbf{x}. \tag{2.22}$$

If we assume that we have a continuous version of the estimate $\hat{f}_1$ and we will denote it by $\tilde{\hat{f}}_1$, then the regularizer for this continuous image $\tilde{\hat{f}}_1$ is defined over the open

set $\mathcal{W}_T$ as given by (2.22), where $\nabla_{\mathbf{x}}$ denotes the gradient. The functional $\mathfrak{L}$ is non-negative, monotonically increasing, and its derivative $\mathfrak{L}'(\cdot) > 0$ except for $\mathfrak{L}'(0) = 0$ [40]. The minimization of (2.22) is a problem of calculus of variations [41]. Using Euler's equation, the minimizer is the steady-state solution of the nonlinear parabolic [42] partial differential equation (PDE) given by:

$$\frac{\partial \tilde{\hat{f}}_1}{\partial \tilde{t}} = \operatorname{div}\left(\frac{\mathfrak{L}'\big(\|\nabla_{\mathbf{x}} \tilde{\hat{f}}_1(\mathbf{x}, \tilde{t})\|\big)}{\|\nabla_{\mathbf{x}} \tilde{\hat{f}}_1(\mathbf{x}, \tilde{t})\|} \nabla_{\mathbf{x}} \tilde{\hat{f}}_1(\mathbf{x}, \tilde{t}) \right). \tag{2.23}$$

Here, $\tilde{t}$ is an *artificial time* parameter for the evolution process of this initial value problem, and div denotes the divergence operator.

One of the variational forms is the anisotropic diffusion for image processing. The anisotropic diffusion was not introduced as a variational objective but rather from a different formulation. This formulation was inherited from the diffusion process of materials in physical medium, then it was successful in the field of image processing too. We will first survey the anisotropic diffusion process and its dynamics then show its relation to the general variational formulation given in (2.22). The anisotropic diffusion process was introduced by Perona and Malik [37] for edge detection and is given by

$$\frac{\partial \tilde{\hat{f}}_1}{\partial \tilde{t}} = \operatorname{div}\Big(c(\|\nabla_{\mathbf{x}} \tilde{\hat{f}}_1(\mathbf{x}, \tilde{t})\|) \nabla_{\mathbf{x}} \tilde{\hat{f}}_1(\mathbf{x}, \tilde{t}) \Big), \tag{2.24}$$

where $c(\cdot)$ is called the conductance of the diffusion process. The proper choice of a monotonically decreasing function $c(\cdot)$ leads to [37]:

- Maximum principle, which means that no new spurious transitions will be introduced, after performing the diffusion process, that were not in the original image. This will avoid introduction of noise outlier patterns;
- Sharpening of edges, because the conductance coefficients will prevent smoothing across the edges and will only smooth along the edges.

Different choices of the function $c(\cdot)$ lead to different behaviors of the diffusion process. This has been extensively studied in the literature and the approaches of anisotropic diffusion are seen to continuously produce new designs for $c(\cdot)$. It should be noted that if $c(\cdot) =$ constant, then by the divergence theorem [43] (2.24) will reduce to the isotropic diffusion equation

$$\frac{\partial \tilde{\hat{f}}_1}{\partial \tilde{t}} = \triangle \tilde{\hat{f}}_1(\mathbf{x}, \tilde{t}), \tag{2.25}$$

where $\triangle$ denotes the linear second-order elliptic partial differential Laplacian operator. By Green's theorem [43] the solution of (2.25) is the successive filtering of an initial image by a Gaussian filter with increasing value of its standard deviation (spread). This gives an insight on the dynamics of the anisotropic diffusion. The conductance $c(\cdot)$ produces low weights for large values of the magnitude of the gradient, thus slowing down the smoothing process and preserving edges. In smooth regions it is almost isotropically symmetric and reduces the diffusion process to the isotropic one (2.25) mimicking Gaussian filtering. The most interesting issue in anisotropic diffusion is its analogy with the MRF regularizer as deduced in [37]. It gains the advantage of using the MRF in the regularization without the need for a complex stochastic optimization method to arrive at a minimum; rather the optimization is achieved at low computational cost. However, the achieved minimum is not guaranteed to be the global minimum that can be obtained from a stochastic optimization method. The results of using anisotropic diffusion in different image processing problems showed success in preserving edge and contours defining objects while maintaining the smoothness in smooth regions. It is accompanied with the following difficulties:

1. The choice of the stopping criterion for the diffusion iterative process is challenging.

2. The choice of the properties of the conductance function $c(\cdot)$ is a governing factor, and an improper choice might lead to an unstable diffusion process. Analysis of

different choices of $c(\cdot)$ applied for image denoising can be found in [44, 45, 40].

3. Other than the maximum principle and edge preservations given in [37], there is no theoretical basis that describes what is the best way to choose $c(\cdot)$ and to extend the method to deal with texture.

Comparing (2.23) and (2.24), it is easy to deduce that $c(\|\nabla_{\mathbf{x}}\tilde{\tilde{f}}_1(\mathbf{x})\|) = \frac{\mathfrak{L}'\left(\|\nabla_{\mathbf{x}}\tilde{\tilde{f}}_1(\mathbf{x})\|\right)}{\|\nabla_{\mathbf{x}}\tilde{\tilde{f}}_1(\mathbf{x})\|}$ which indicates that the anisotropic (nonlinear) diffusion proposed by [37] can be obtained by setting $\mathfrak{L}(s) = \int_{\mathcal{W}_T} sc(s)d\mathbf{x}$.

If we set $\mathfrak{L}(\|\nabla_{\mathbf{x}}\tilde{\tilde{f}}_1(\mathbf{x})\|) = \|\nabla_{\mathbf{x}}\tilde{\tilde{f}}_1(\mathbf{x})\|$ in (2.22) we arrive at $\mathcal{J}_s$ that defines the so-called *total-variation norm*. It is the L_1-norm of the magnitude of the spatial gradient. This was the regularizer introduced by Rudin, Osher, and Fatemi in [38] and sometimes called the *ROF* model. The evolution equation (2.23) becomes

$$\frac{\partial\tilde{\tilde{f}}_1}{\partial\tilde{t}} = \operatorname{div}\left(\frac{\nabla_{\mathbf{x}}\tilde{\tilde{f}}_1(\mathbf{x},\tilde{t})}{\|\nabla_{\mathbf{x}}\tilde{\tilde{f}}_1(\mathbf{x},\tilde{t})\|}\right) = \kappa, \tag{2.26}$$

where κ is the mean curvature of $\tilde{\tilde{f}}_1(\mathbf{x},\tilde{t})$. The results of minimizing the total-variation norm showed remarkable enhancement in all its applications in the different fields of use for image processing. The space of all signals that have bounded total-variation norm (BTV) has been described in [38] as the "proper" space for image processing and as the "right" regularizer in [31]. *Indeed, BTV is the only known space until now that permits discontinuities as part of its admissible solutions.* This means that contours of boundaries are not penalized. The total-variation norm is a measure of the sum of the lengths of all the level lines in the image defined for discrete finite number of levels. *Thus the minimization of the total-variation norm leads to an image whose iso-intensity contours are the least oscillatory.* In this thesis, I will pursue the research using the total-variation regularizer due to its success. Since this regularizer is our chosen one here and the most interesting, the next chapter is dedicated to provide details of its dynamics and discuss the mathematical tools needed for it. It should

be noted that the solution of (2.26) leads to parabolic PDEs optimization problem. Perhaps this is the reason that makes some researchers reluctant to use the total-variation norm to avoid the need to enter another field in mathematics. Fortunately, the total-variation norm has been studied for a long time in other sciences and there is a rich literature and numerical methods that are developed and made available. In this thesis, we will see also contributions to the numerics of minimizing the total-variation norm, which are:

- Producing new approximations to the partial derivatives that are deduced from the properties of the device used to display (reconstruct) $\hat{f}_1[\mathbf{x}]$;
- New choice of the evolution process properties for minimizing $\mathcal{J}_d$ and $\mathcal{J}_s$ that allows the process to be initiated by any initial value condition (image), including constant intensity images, and to proceed without being trapped in any local minima. This leads to a stable solution with a unique minimizer.

Similarly the evolution by mean curvature in [39] is just the ROF model but the Euler equation is multiplied by the magnitude of the gradient. This leads to the evolution equation

$$\frac{\partial \tilde{\hat{f}}_1}{\partial \tilde{t}} = \operatorname{div}\left(\frac{\nabla_{\mathbf{x}} \tilde{\hat{f}}_1(\mathbf{x},\tilde{t})}{\|\nabla_{\mathbf{x}} \tilde{\hat{f}}_1(\mathbf{x},\tilde{t})\|}\right)\|\nabla_{\mathbf{x}} \tilde{\hat{f}}_1(\mathbf{x},\tilde{t})\| = \kappa\|\nabla_{\mathbf{x}} \tilde{\hat{f}}_1(\mathbf{x},\tilde{t})\|. \tag{2.27}$$

This model is very similar in its properties to the ROF model when the magnitude of the gradient is non-zero. Osher, one of the authors of the ROF model, along with Sethian, have already developed (2.27) earlier in [46] which was not dedicated for image processing.

Before closing the regularization section, it should be noted that the choice of the regularization parameter is one of the associated difficulties. However, there are many methods for choosing the regularization parameter. A collection of some of the commonly used methods can be found in [31]. A recent paper for the choice of the

regularization parameter for image up-sampling based on cross-validation is reported in [47].

Chapter 3

Variational Formulation for Image Up-sampling

Variational regularizers that were briefly discussed in section 2.3.3 have been widely used in various image processing applications. However, their usage in the image up-sampling problem is limited. In this chapter we shall discuss a variational formulation for the grey-scale image up-sampling problem. This formulation might be applicable for the color image up-sampling case if each color channel is treated separately. Also, the vectorial variational formulation for color images will be surveyed and discussed separately in this thesis.

As discussed in section 2.3.3, the problem is formulated by two objective criteria that are set on the metrics $\mathcal{J}_s$ and $\mathcal{J}_d$ that interact together. When $\mathcal{J}_s$ has a variational form then this interaction represents a constrained variational problem which is usually formulated in a Lagrangian framework [41], and its solution is achieved by the numerical implementation of the Euler–Lagrange equation. This will be the main focus of this chapter. Sections 3.2–3.5 will provide in-sight details of the previous variational schemes that were used for image denoising and restoration. The drawbacks and numerical challenges for these approaches will be discussed in section 3.5.

My proposed variational formulation for the problem of grey-scale image up-sampling will be given in section 3.6. The use of this formulation is new for the image up-sampling problem, and furthermore it treats many of the drawbacks of the previous formulations that are discussed in section 3.5. Before going into the details and the dynamics of this formulation, in section 3.1 we will first give a brief survey of the previous approaches that used the variational formulation in solving the grey-scale image up-sampling problem.

3.1 Previous variational formulations of image up-sampling

Most of the reported scalar variational formulation approaches made use of the ROF model in defining $\mathcal{J}_s$, but the data fidelity $\mathcal{J}_d$ has been oversimplified. It was assumed that the samples of the LR images should have the same grey-value level in the HR image. This is equivalent to setting the observation model to be a unit sample impulse. This route was taken by [48, 49, 50, 51, 52] with which I disagree. In fact, the observation model relates an area of the HR image to a sample in the LR image simulating the sensor process in integrating light. This has been suggested by many researchers in the field [6, 18] and even as part of the conclusions by the authors of one of these papers themselves [49]. This will also be shown and proved in chapter 4. The impact of the choice of the unit sample impulse function as an observation model is reducing the number of constraints on the samples of the HR image. The set of all samples $\{\hat{f}_1[\mathbf{x}] \mid \mathbf{x} \in \{\Lambda \setminus \Gamma\}\}$ in the HR image which are not related by equality to samples in the LR image, are synthesized under the discretion of the smoothness criterion $\mathcal{J}_s$. This has a negative impact on the stability of the solution near the edges, the textured regions, and the heavy dependency of the results on the choice of the initial estimate. This simplification of the observation model came as a straightforward extension of the variational formulation in the denoising problem without going into the details of dealing with the constraints as I shall do in this

chapter. To mitigate the problem of dependency on the initial guess, every approach added extra constraints on the solution space. This lacks a theoretical basis. It is preferable to have a well-formulated problem from the beginning than trying to come up with ad-hoc constraints.

The authors in [51, 52] followed the anisotropic diffusion idea for the regularization part. They ran the diffusion process backward in the artificial time. This was done by choosing the conductance function $c(\cdot)$ in (2.24) to have some negative-valued regions. This has the effect of sharpening many patterns including the edges. The choice of the negative values for some regions of $c(\cdot)$ is proven to violate the stability of the diffusion process by a theorem in [40]. Indeed, the diffusion process is irreversible, hence the backward diffusion in artificial time is an ill-posed problem. The authors were aware of this ill-posedness and mentioned that the stability is achievable for just very limited circumstances. They declared the inadequacy of the method for textured regions. The results also show the development of spurious patterns in some smooth regions like clouds in the sky.

The exception from the above methods in solving the variational formulation that is associated with data constraint in image up-sampling was done in [53]. However they avoided dealing with the derivative of the down-sampling operation in the $\mathcal{J}_d$ criterion by reverting the problem to a restoration framework that was previously handled by others. They obtained an HR image estimate from the observed LR image by using the discrete sinc interpolator. This estimate served as their observation data instead of the LR image given. They assumed that the observation model is a moving average blurring filter. The rationale behind this approach is to bring the observation model as a measure between two images at the same sampling structure Λ, avoiding the need to have the down-sampling operation as part of the observation model. This formulation is solved in a similar way to the previous variational formulations for image restoration problems. It is known that the sinc interpolator produce Gibbs' phenomena as shown

before in Fig. 2.7(b). The authors resorted to over-regularization to get rid of these ringing artifacts, which finally resulted in a blurred image especially in the textured regions.

3.2 Unconstrained variational formulation

In order to proceed with the whole problem formulation we will first analyze the general variational regularizer. Recall the general functional formulation given in (2.22) which is minimized using Euler's equation as the steady-state solution of the evolution process given in (2.23). Factoring the divergence operator, or using the eigenvalue decomposition of the Hessian of $\mathfrak{L}(\|\nabla_{\mathbf{x}}\tilde{\tilde{f}}_1)\|)$ as done in [40] we obtain

$$\frac{\partial \tilde{\tilde{f}}_1}{\partial \tilde{t}} = \frac{\mathfrak{L}'\big(\|\nabla_{\mathbf{x}}\tilde{\tilde{f}}_1(\mathbf{x},\tilde{t})\|\big)}{\|\nabla_{\mathbf{x}}\tilde{\tilde{f}}_1(\mathbf{x},\tilde{t})\|}\kappa\|\nabla_{\mathbf{x}}\tilde{\tilde{f}}_1(\mathbf{x},\tilde{t})\| + \mathfrak{L}''\big(\|\nabla_{\mathbf{x}}\tilde{\tilde{f}}_1(\mathbf{x},\tilde{t})\|\big)\kappa^{\perp}\|\nabla_{\mathbf{x}}\tilde{\tilde{f}}_1(\mathbf{x},\tilde{t})\|. \tag{3.1}$$

At a specific artificial time instant, κ is the mean curvature of $\tilde{\tilde{f}}_1(\mathbf{x})$ and $\kappa^{\perp}$ can be thought as the dual mean curvature [40]. In other words, $\kappa\|\nabla_{\mathbf{x}}\tilde{\tilde{f}}_1(\mathbf{x})\|$ is the second-order directional derivative in the direction that is orthogonal to the gradient $\nabla_{\mathbf{x}}\tilde{\tilde{f}}_1(\mathbf{x})$, and $\kappa^{\perp}\|\nabla_{\mathbf{x}}\tilde{\tilde{f}}_1(\mathbf{x})\|$ is the second-order directional derivative in the direction of the gradient $\nabla_{\mathbf{x}}\tilde{\tilde{f}}_1(\mathbf{x})$. The geometric interpretation of (3.1) is very interesting and sheds light on the dynamics of variational regularizers. The evolution process is seen as an energy dissipation process in two orthogonal directions. This dissipation process diffuses $\tilde{\tilde{f}}_1(\mathbf{x},\tilde{t})$ along the direction of the gradient and along the orthogonal direction to the gradient. The diffusion process of the grey-values of $\tilde{\tilde{f}}_1(\mathbf{x},\tilde{t})$ along the direction of the spatial gradient (orthogonal to the image contours) is seen as a kind of averaging across both sides of the image contours. This has the effect of blurring contours and smoothing the image as in the case of linear interpolators, which is an undesirable action and is required to be suppressed. The diffusion process of $\tilde{\tilde{f}}_1(\mathbf{x},\tilde{t})$ along the orthogonal direction to the gradient (along the image contours) is seen as edge-directed

filtering as shown before in Fig. 2.11. This will preserve the location and the intensity strength of the contours, all the while smoothing along them and maintaining their crispness, which represent a desirable requirement. Both requirements can be satisfied in this geometrical sense if we let $\mathfrak{L}^{\shortparallel}(\cdot)$ vanish while maintaining a non-zero $\mathfrak{L}^{\shortmid}(\cdot)$. Intuitively, it seems that choosing $\mathfrak{L}(\cdot)$ as a non-zero linear function will do the job. This means that a possible desirable function is $\mathfrak{L}(\|\nabla_{\mathbf{x}}\tilde{\hat{f}}_1(\mathbf{x})\|) = \|\nabla_{\mathbf{x}}\tilde{\hat{f}}_1(\mathbf{x})\|$. This choice leads to the evolution process given by

$$\frac{\partial \tilde{\hat{f}}_1}{\partial \tilde{t}} = \kappa = \operatorname{div}\left(\frac{\nabla_{\mathbf{x}}\tilde{\hat{f}}_1(\mathbf{x},\tilde{t})}{\|\nabla_{\mathbf{x}}\tilde{\hat{f}}_1(\mathbf{x},\tilde{t})\|}\right). \tag{3.2}$$

This is exactly the evolution process of the ROF model given in (2.26). This analysis provides sufficient evidence about the success one would expect using the ROF variational scheme.

The ROF regularizer, $\mathcal{J}_s(\tilde{\hat{f}}_1) = \int_{\mathcal{W}_T} \|\nabla_{\mathbf{x}}\tilde{\hat{f}}_1(\mathbf{x})\| d\mathbf{x}$, that we have chosen in this thesis has also unique mathematical interpretations:

- It defines a space of BTV signals with possible discontinuities. This is a suitable space for natural images because they usually contains sharp discontinuities at the borders separating different objects;

- Its minimizer is an image which has the least oscillatory iso-intensity contours. This means that the solution with crisp contours is preferable to the oscillatory and jagged ones. This will be desirable for maintaining crisp edges if the observed data in the LR image agrees.

From a signal processing perspective, the evolution process given by (3.2) is fully an implicit local edge-directed interpolation process that is performed without the need for any explicit edge detection technique. To understand this statement let us consider the family of variational regularizers of the form $\mathfrak{L}(\|\nabla_{\mathbf{x}}\tilde{\hat{f}}_1(\mathbf{x})\|) = \|\nabla_{\mathbf{x}}\tilde{\hat{f}}_1(\mathbf{x})\|^p$, where

$1 \leq p \leq 2$ is a real number. The Euler equation for this family of regularizers is simply given by

$$p\|\nabla_{\mathbf{x}}\tilde{\hat{f}}_1(\mathbf{x})\|^{p-2}\kappa\|\nabla_{\mathbf{x}}\tilde{\hat{f}}_1(\mathbf{x})\| + p(p-1)\|\nabla_{\mathbf{x}}\tilde{\hat{f}}_1(\mathbf{x})\|^{p-2}\kappa^{\perp}\|\nabla_{\mathbf{x}}\tilde{\hat{f}}_1(\mathbf{x})\| = 0. \tag{3.3}$$

The case when $p = 2$ will lead to having the L.H.S. of (3.3), after simple manipulation, become a symmetric Laplacian operator $\triangle\tilde{\hat{f}}_1(\mathbf{x})$. This means that we arrive at the PDE of isotropic diffusion given by (2.25)! More interesting than the analogy to isotropic diffusion is that this process will dissipate energy from $\tilde{\hat{f}}_1(\mathbf{x})$ in all directions by the same weight. This is due to the fact that the Laplacian operator is symmetric as shown in Fig. 2.14. According to Green's theorem, the solution to this PDE is simply the successive convolution with a Gaussian filter. This means that our interpolation filter has a frequency response which is also a Gaussian. Since the Gaussian filter is isotropic and recalling the concept presented in Fig. 2.11, then it acts as a simple linear interpolator. The case when $p = 1$ (total-variation norm) as given above describes dissipation of energy from $\tilde{\hat{f}}_1(\mathbf{x})$ that is locally along the orthogonal direction to the gradient $\nabla_{\mathbf{x}}\tilde{\hat{f}}_1$ and is suppressed along the direction of the gradient because $(p-1) = 0$ in this and only this case. Hence, we can build for it the following mental model: a 1-D approximation of the Laplacian operator (filter) has been oriented along the local edge (contour) direction. In the spatial domain the local impulse response of this filter become very localized along the direction of the gradient and with a non-negligible spread along the orthogonal direction. Recalling Fig. 2.11, then the profile of the frequency response of this filter will be spread along the profile of the spectrum of the underlying edge. This is exactly an ideal edge-directed interpolation filter. It is obvious that in smooth regions, where the gradient vanishes ($\|\nabla_{\mathbf{x}}\hat{f}_1(\mathbf{x})\| \approx 0$), the regularizer will have no impact and the process will be purely dependent on some associated data fidelity term. When p varies from 1 (maximum edge-directed preservedness) to 2 (isotropic smoothness), we will have a mix of effects. The interesting cases might

be for values of p closer to 1 ($p = 1 + \epsilon$). This might open up interesting areas like how to choose an optimal value of p that enhances some aspects of the results over that obtained from minimizing the total-variation norm. We did not consider the case of ($p < 1$) because this leads to non convex functional [54]. In this thesis we are interested in the case of $p = 1$ because of the following:

- its uniqueness as a pure edge-directed operation with no blurring;
- it is well analyzed mathematically and geometrically;
- the availability of stability analysis and numerical techniques for it.

The evolution process by mean curvature (3.2) has been extensively studied and we will give a brief discussion about it. The best framework to understand it is through the concept of level sets and propagation of fronts. These will be handled in the next section

3.3 The level set method and propagation of fronts

The *level set method* (LSM) is concerned with the evolution (propagation) of fronts at a certain spatially-variant speed along the normal direction to the front. This evolution changes the position and the topology of the front as it propagates in artificial time. The set of all positions in artificial time that a front occupies during its evolution is called its level set.

Several questions arise here: why do we care about LSM? and what has this got to do with images? The answer is that images can be fully described by their iso-intensity contours—contours that have equal grey-scale value. These iso-intensity contours are sometimes named in the literature as *fronts* or *isophotes*. To illustrate the concept, I plotted the isophotes of the sample image that was given in Fig. 2.7(a) with two different plots as shown in Fig. 3.1. The first plot is in dense isophotes where the grey-values of the image were grouped into 50 quantization levels producing 50 isophotes,

and the second is just a sketchy one with only 5 isophotes. This is just for illustration, but when it comes to implementation the isophotes can be thought of being quantized with a huge number of levels, specifically related to the resolution of the word length of the machine used. It can be seen from Fig. 3.1 that even with few isophotes the image contents are visible, and more interesting is the identification of some features. For instance, the effect of aliasing along the border of the camera handle looks like wavy isophotes; this is barely noticeable in the original image but becomes severe when this image is up-sampled. Then the fronts of the LSM, in the case of images, are the iso-intensity contours of the image. If we let the image isophotes propagate with different types of motion with special characteristics, then we can obtain results like straightening out oscillatory contours, shrinking an isolated noise within a smooth region so that it vanishes as in morphological operations, preserving the boundaries of small objects,... etc.

The level-set equation is a modern form of the G-equation that describes the evolution of the front of a flame in the field of combustion [54]. It was brought to many other fields, including image processing, by Osher and Sethian [46]. They derived its general form as

$$\frac{\partial \tilde{\hat{f}}_1(\mathbf{x},\tilde{t})}{\partial \tilde{t}} + \nu(\mathbf{x},\tilde{t})\|\nabla_{\mathbf{x}} \tilde{\hat{f}}_1(\mathbf{x},\tilde{t})\| = 0, \tag{3.4}$$

where $\tilde{t}$ is again an artificial time parameter for the evolution process and $\nu(\cdot)$ is the speed of the evolution along the normal direction. There are several types of evolutions (motions) which are described by the properties of the speed ν [55]. In the problem of regularized image up-sampling of a grey-scale still image we are interested in preserving edges and controlling the introduction of spurious noise, all the while essentially maintaining the data constraints. These interests can be interpreted in my proposed scheme by a hybrid motion, dependent on the local properties of the fronts and their position as will be discussed in the subsequent sections.

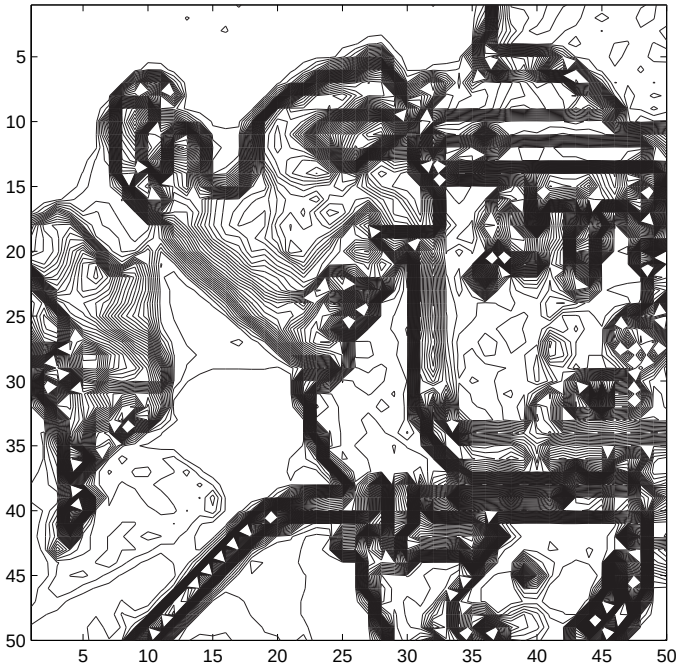

(a)

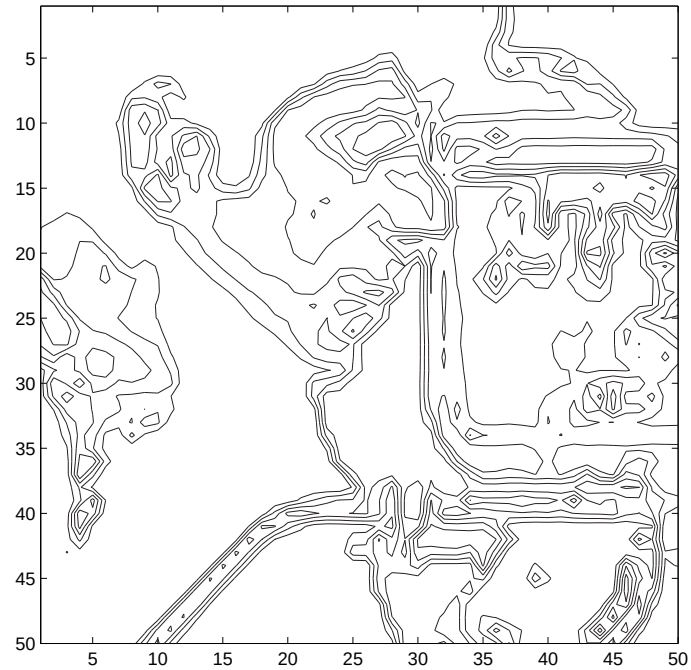

(b)

Fig. 3.1 Isophotes of a portion of the cameraman image (a) dense 50 quantization levels (b) sketchy: 5 quantization levels.

3.3.1 Motion under curvature

Motion under curvature means that the LSM evolves the fronts with speed

$$\nu(\mathbf{x}, \tilde{t}) = \nu_s(\mathbf{x}, \tilde{t}) = -\kappa, \tag{3.5}$$

where κ is the curvature of the front at artificial time $\tilde{t}$. In case of scalar grey-scale images the curvature is given by

$$\kappa = \operatorname{div}\left(\frac{\nabla_{\mathbf{x}}\tilde{\hat{f}}_1(\mathbf{x}, \tilde{t})}{\|\nabla_{\mathbf{x}}\tilde{\hat{f}}_1(\mathbf{x}, \tilde{t})\|}\right) = \frac{\tilde{\hat{f}}_{1_{xx}}\tilde{\hat{f}}_{1_y}^2 - 2\tilde{\hat{f}}_{1_x}\tilde{\hat{f}}_{1_y}\tilde{\hat{f}}_{1_{xy}} + \tilde{\hat{f}}_{1_{yy}}\tilde{\hat{f}}_{1_x}^2}{\left(\tilde{\hat{f}}_{1_x}^2 + \tilde{\hat{f}}_{1_y}^2\right)^{3/2}}, \tag{3.6}$$

where the suffix denotes the spatial partial derivative. The evolution given by the speed (3.5) is known as phase field reaction process, and it can be approximated numerically as given in [54] by central differences. However, in this thesis we will develop new approximations of the partial derivatives based on the properties of the display (reconstruction) device. A nice geometric study of this type of evolution can be found in [55]. Variants of this type of evolution like volume preserving curvature and the second-order derivative of the curvature are also given in [55]. Another variant based on min/max curvature is given in [56]. These ideas might be powerful with the possibility of providing good results, but their geometrical features and applications in image processing are still immature. The evolution by mean curvature with its connection to anisotropic diffusion has well-established geometrical features. It has been demonstrated in [55] that the evolution of fronts by this kind of motion is characterized by the following:

1. Any arbitrarily shaped closed front with arbitrary concavities and convexities (wrinkles) will evolve to form a convex hull by means of the following motions:
   (a) Concavities will be pushed outwards.
   (b) Convexities will be pulled inwards

2. This convex hull will shrink in artificial time until it becomes a point that vanishes.

If we assume that an arbitrary initial image $\tilde{\hat{f}}_1$ is processed by equations (3.4,3.5), then its iso-intensity contours will undergo an evolution process under mean curvature. The extent of this evolution process is governed by the artificial time $\tilde{t}$ of the evolution; in practice this is interpreted as iterations as will be shown later. This means that extended time evolution process under mean curvature will shrink all the image isophotes until the image becomes a constant one. It should be noted that there will be another type of motion that enforces the data fidelity $\mathcal{J}_d$ such that the collapse of the image isophotes is not reached at convergence of the evolution process. The discussed geometrical properties of the evolution under mean curvature will have the following impacts on images that undergo this process:

- It will straighten out the fronts, removing the oscillations along the edges *regardless of their orientation*;
- It will shrink down isolated noise patterns that exist in smooth regions;
- Textures will undergo a mix of smoothing and sharpening that is not easy to analyze because textures have different patterns. However, overall textures will not be deteriorated like in all the previously discussed classes in section 2.3.

3.3.2 Position dependent motion

This type of motion is independent of the front geometrical features but is governed by external constraints. These external constraints are position dependent. If the data fidelity criterion $\mathcal{J}_d$ given in (2.16) is used here, then it will enforce spatial constraints on the HR image fronts. These constraints are given mainly in terms of the samples of the LR image and the properties of H, η. The motion that is dependent on the position of the front acts as a projection on the data constraints. It was developed

for image restoration problem [57]. Its form for image up-sampling problem is very similar and I write it as

$$\nu_d(\mathbf{x},\tilde{t}) \triangleq \lambda \frac{\mathbf{H}^{\mathrm{T}}(\mathbf{H}\hat{\mathbf{f}}_1 - \mathbf{f}_2)}{\|\nabla_{\mathbf{x}}\tilde{\hat{f}}_1(\mathbf{x},\tilde{t})\|}. \tag{3.7}$$

The LSM evolution described by a speed $\nu(\mathbf{x},\tilde{t}) = \nu_d(\mathbf{x},\tilde{t})$ is called convection diffusion. Its evolution is similar to an iterative back projection of the residual error to the estimate $\hat{f}_1$. The properties of this evolution are similar to those that have been explained before in section 2.3.3. The parameter λ is a weighting parameter that controls the strength of the interaction of this motion on the evolution process.

3.3.3 Time derivative

The LSM evolution equations given until now involve a continuum time derivative. This artificial time derivative is usually implemented numerically using the forward Euler method so that the LSM general equation becomes

$$\tilde{\hat{f}}_1^{(n+1)}(\mathbf{x}) = \left[\tilde{\hat{f}}_1(\mathbf{x}) - \Delta T\Big(\nu(\mathbf{x})\|\nabla_{\mathbf{x}}\tilde{\hat{f}}_1(\mathbf{x})\|\Big)\right]^{(n)}, \tag{3.8}$$

where ΔT is an artificial time step that should satisfy numerical stability conditions as given in [54]. The superscript (n) denotes the iteration number. Thus, starting with an initial estimate $\tilde{\hat{f}}_1^{(0)}$ this initial value PDE problem is solved iteratively by (3.8). Higher order numerical schemes for implementing the time derivative based on Runge–Kutta method is given in [54]. With forward Euler time discretization a Courant–Friedreichs–Lewy (CFL) condition for stability is given by

$$\Delta T\big(\frac{2}{(\Delta x)^2} + \frac{2}{(\Delta y)^2}\big) < 1, \tag{3.9}$$

where Δx and Δy are the spatial-domain discretization steps which could be simply that of the underlying sampling structure.

3.4 Constrained variational formulation

The constrained variational formulation has been used in image denoising, as in the ROF model given in [38] and in image restoration as in [57]. Their formulation is given using our notation as follows

$$\begin{aligned}
\hat{\mathbf{f}}_1 = \arg\Big\{ \min_{\mathbf{g}} \int_{\mathcal{W}_T} \|\nabla_{\mathbf{x}} \tilde{\mathbf{g}}(\mathbf{x})\| d\mathbf{x}, \qquad \text{s.t. } \frac{1}{2}\|H\mathbf{g} - \mathbf{f}_0\|^2 = \sigma^2 \Big\}, \\
g[\mathbf{d}] = \tilde{g}(\mathbf{d}), \quad \forall \mathbf{d} \in \Lambda, \\
\tilde{g}(\mathbf{x}) = \sum_{\mathbf{d}\in\Lambda} g[\mathbf{d}]\psi(\mathbf{x}-\mathbf{d}), \quad \forall \mathbf{x} \in \mathcal{W}_T \\
g \in \ell^2(\Lambda), \quad f_0 \in \ell^2(\Lambda),
\end{aligned} \tag{3.10}$$

where σ^2 is the variance of the distribution of the identically-independent zero-mean noise η and f_0 is the measured noisy and/or blurred image. Both f_1 and f_0 are defined over the same sampling structure Λ. Such equality constraints are called holonomic constraints [41]. For the denoising problem, the matrix H is an identity matrix. For the deblurring problem, the blur *point spread function* (PSF) is represented by the impulse response of the filter $h[\mathbf{x}]$. The matrix H, in this case, is the convolution matrix for this filter $h[\mathbf{x}]$ and it has a Toeplitz structure. Then the transposed matrix H^{T} is the convolution matrix for the spatial-reversal filter $h[-\mathbf{x}]$. In the noise free case, we set $\sigma^2 = 0$. In a general sense, ψ is a continuous operator that generates the continuous image $\tilde{f}_1$ from the samples $f_1[\mathbf{x}]$ and formally the definition of a spatial gradient for this continuous image is valid. In the literature, ψ was not discussed or dealt with or it was implicitly assumed to be a piece-wise smooth function. The gradients $\nabla_{\mathbf{x}}\tilde{f}_1(\mathbf{x})$ were estimated by finite differences from the discrete samples of $f_1[\mathbf{x}]$. In all the implementations for the variational formulation in the literature, it is assumed that the samples $\hat{f}_1$ are exactly those values of a continuous signal $\tilde{\hat{f}}_1$ at the corresponding grid locations. The problem given by (3.10) is converted to an

unconstrained minimization problem using the Lagrangian formulation

$$\hat{\mathbf{f}}_1 = \arg\min_{\mathbf{g}} \Big\{ \int_{\mathcal{W}_T} \|\nabla_{\mathbf{x}} \tilde{g}(\mathbf{x})\| d\mathbf{x} + \mu(\tilde{g}) \big(\frac{1}{2} \|H\mathbf{g} - \mathbf{f}_0\|^2 - \sigma^2 \big) \Big\}, \tag{3.11}$$

where μ is a Lagrange multiplier. In this case of holonomic constraint, μ is mathematically a function of the iterate $\tilde{g}$ which ensures that the constraint is satisfied at any artificial time instant of the implementation. The minimization of this unconstrained problem is the steady-state solution of the PDEs that arise from the Euler–Lagrange equations, and is given as follows.

$$\frac{\partial \tilde{\hat{f}}_1}{\partial \tilde{t}} = \kappa - \mu(\tilde{\hat{f}}_1) H^{\mathrm{T}} (H\hat{\mathbf{f}}_1 - \mathbf{f}_0). \tag{3.12}$$

Using the Euler forward method these PDEs are converted to the solution of the following iterative process

$$\hat{\mathbf{f}}_1^{(n+1)} = \Big[\hat{\mathbf{f}}_1 + \Delta T \Big(\kappa - \mu H^{\mathrm{T}} (H\hat{\mathbf{f}}_1 - \mathbf{f}_0) \Big) \Big]^{(n)}. \tag{3.13}$$

The holonomic constraint is not explicitly enforced in (3.13). It is implicitly implemented in the Lagrange multiplier. Following the method in [38] for the computation of μ that satisfies the constraints in (3.10), it has to be calculated at each iteration. It can be given for the noise free case ($\sigma = 0$) [57] by

$$\mu^{(n)} = \left[\frac{\int_{\mathcal{W}_T} \kappa h[-\mathbf{x}] * (h[\mathbf{x}] * \hat{f}_1[\mathbf{x}] - f_0[\mathbf{x}]) d\mathbf{x}}{\|H^{\mathrm{T}} (H\hat{\mathbf{f}}_1 - \mathbf{f}_0)\|^2} \right]^{(n)}. \tag{3.14}$$

At this point what is left is the numerical implementations of the partial derivatives in the mean curvature term κ. This is the most critical and tricky part, that should be done with care. Generally, the numerical implementation of PDEs should take into account the domain of dependence of the underlying data [54]. In the case of the

parabolic term κ, the domain of dependence is all the surrounding spatial data with no bias towards a specific direction [42]. Hence, the most suitable discretization advised in [54, 55] for the curvature term is the second-order central differences. According to the assumption in (3.10) that $\hat{f}_1[\mathbf{x}] = \tilde{\hat{f}}_1(\mathbf{x}), \quad \forall \mathbf{x} \in \Lambda$, then the continuum formulation is reduced in the implementation to be executed on the points of Λ using the samples of $\hat{f}_1$. In all of these implementations in the literature it is assumed that Λ is a rectangular lattice. If we assume this special case, where Λ is rectangular, then we have $V_\Lambda = [\mathbf{v}_1 \mid \mathbf{v}_2]$ and $\mathbf{v}_1 = [X, 0]^{\mathrm{T}}, \quad \mathbf{v}_2 = [0, Y]^{\mathrm{T}}$, and $\Delta x = X$ and $\Delta y = Y$. Recalling (3.6), we have five partial derivatives to implement. These five partial derivatives are given in terms of our lattice notation as follows:

$$
\begin{aligned}
\tilde{\hat{f}}_{1_x}(\mathbf{d}) &= \frac{\hat{f}_1[\mathbf{d}+\mathbf{v}_1] - \hat{f}_1[\mathbf{d}-\mathbf{v}_1]}{2X} + \mathbf{O}[X^2], \\
\tilde{\hat{f}}_{1_y}(\mathbf{d}) &= \frac{\hat{f}_1[\mathbf{d}+\mathbf{v}_2] - \hat{f}_1[\mathbf{d}-\mathbf{v}_2]}{2Y} + \mathbf{O}[Y^2], \\
\tilde{\hat{f}}_{1_{xx}}(\mathbf{d}) &= \frac{\hat{f}_1[\mathbf{d}+\mathbf{v}_1] - 2\hat{f}_1[\mathbf{d}] + \hat{f}_1[\mathbf{d}-\mathbf{v}_1]}{X^2} + \mathbf{O}[X^2], \\
\tilde{\hat{f}}_{1_{yy}}(\mathbf{d}) &= \frac{\hat{f}_1[\mathbf{d}+\mathbf{v}_2] - 2\hat{f}_1[\mathbf{d}] + \hat{f}_1[\mathbf{d}-\mathbf{v}_2]}{Y^2} + \mathbf{O}[Y^2], \\
\tilde{\hat{f}}_{1_{xy}}(\mathbf{d}) &= \frac{\hat{f}_1[\mathbf{d}+\mathbf{v}_1+\mathbf{v}_2] + \hat{f}_1[\mathbf{d}-\mathbf{v}_1-\mathbf{v}_2] - \hat{f}_1[\mathbf{d}+\mathbf{v}_1-\mathbf{v}_2] - \hat{f}_1[\mathbf{d}-\mathbf{v}_1+\mathbf{v}_2]}{4XY} + \mathbf{O}[XY], \\
&\quad \forall \mathbf{d} \in \Lambda.
\end{aligned}
\tag{3.15}
$$

The asymptote for the truncation error is denoted by the order $\mathbf{O}[\cdot]$. These partial derivatives can be efficiently implemented by a simple convolution process. Thus, the second-order approximation of the partial derivatives becomes

$$
\tilde{\hat{f}}_{1_{(\cdot)}}(\mathbf{d}) = \hat{f}_1[\mathbf{d}] * h_{(\cdot)}[\mathbf{d}], \ \forall \mathbf{d} \in \Lambda.
$$

The impulse responses of the filters $h_{(\cdot)}[\mathbf{d}]$ for the implementation of each of the partial

derivatives are given as follows:

$$\begin{aligned} h_x &= [\ 0.5 \quad \mathbf{0} \quad -0.5\ ], \\ h_y &= [\ 0.5 \quad \mathbf{0} \quad -0.5\ ]^{\mathrm{T}}, \\ h_{xx} &= [\ 1 \quad \mathbf{-2} \quad 1\ ], \\ h_{yy} &= [\ 1 \quad \mathbf{-2} \quad 1\ ]^{\mathrm{T}}, \\ h_{xy} &= \begin{pmatrix} 1 & 0 & -1 \\ 0 & \mathbf{0} & 0 \\ -1 & 0 & 1 \end{pmatrix} /4. \end{aligned} \tag{3.16}$$

The bold number indicates the central position $\mathbf{x} = \mathbf{0}$. It should be noted that we are using a top-to-bottom orientation, i.e, the positive vertical direction points downwards. The problem given in (3.10) is fully solved by the set of equations (3.13), (3.14), and (3.15).

3.5 Numerical challenges for the total variation formulation

The numerical implementation for the formulation of the denoising/deblurring problem using the total variation, given in section 3.4, has some numerical difficulties. These difficulties have been addressed by some techniques in the literature. In this section we will discuss these difficulties and their remedies and the side effects of some of these remedies. In our formulation in this thesis we will make use of some of these remedies and develop ours that would eliminate the side effects of those methods developed in the literature. The four challenges for the implementation are given as follows:

1. At the formulation level, the L_1-norm objective criterion $\mathcal{J}_s$ is non-differentiable at $\|\nabla_{\mathbf{x}} \tilde{\tilde{f}}_1\| = 0$ which occurs in the smooth regions of the image;

2. The curvature term appearing in the evolution equation (3.13) is stiff and destabilizes the solution;

3. The initialization and the calculation of (3.14) is problematic;

4. The second-order approximation (3.15) which is numerically reliable, relies on the assumptions that $\hat{f}_1[\mathbf{x}] = \tilde{\hat{f}}_1(\mathbf{x}), \quad \forall \mathbf{x} \in \Lambda$, and that Λ is rectangular. These two assumptions are not representing the reality.

The first major problem is that the L_1-norm associated with the total variation regularizer is by nature non-differentiable at a zero-valued argument ($\|\nabla_{\mathbf{x}} \tilde{\hat{f}}_1\| = 0$). Although the L_1-norm is continuous at the origin, its left derivative ($\mathfrak{L}`(0-\epsilon)$) is not equal to its right derivative ($\mathfrak{L}`(0-\epsilon)$) and thus the derivative does not exist at the origin. This means that the convex objective function that we are dealing with is non-differentiable at the origin. It was this challenge that made most researchers reluctant to use the L_1-norm and instead use the ℓ_2-norm in most regularized image processing problems. The ℓ_2-norm is continuously differentiable and is minimized by traditional linear optimization techniques, but it sacrifices the quality of the resulting image. This is due to the fact that it leads to non-directional regularizer that smooths the images blindly regardless of the existing edges, as discussed in section 3.2. A common practice for getting around the aforementioned problem is to replace the magnitude of the gradient $\|\nabla_{\mathbf{x}} \tilde{\hat{f}}_1\| = \sqrt{\tilde{\hat{f}}^2_{1_{(x)}} + \tilde{\hat{f}}^2_{1_{(y)}}}$ by an approximation $\|\nabla_{\mathbf{x}} \tilde{\hat{f}}_1\| = \sqrt{\tilde{\hat{f}}^2_{1_{(x)}} + \tilde{\hat{f}}^2_{1_{(y)}} + \epsilon^2}$, where ϵ is a small real number chosen according to the machine precision. This alteration totally changes the total variation regularizer to another differentiable objective criterion. Although it seems that the change is minor, in fact it is severe because given $\mathfrak{L}(\|\nabla_{\mathbf{x}} \tilde{\hat{f}}_1\|) = \sqrt{\tilde{\hat{f}}^2_{1_{(x)}} + \tilde{\hat{f}}^2_{1_{(y)}} + \epsilon^2}$ and recalling the generalized analysis (3.1) we realize that $\mathfrak{L}`(\|\nabla_{\mathbf{x}} \tilde{\hat{f}}_1\|) = \|\nabla_{\mathbf{x}} \tilde{\hat{f}}_1\| / \sqrt{\|\nabla_{\mathbf{x}} \tilde{\hat{f}}_1\|^2 + \epsilon^2}$ and $\mathfrak{L}``(\|\nabla_{\mathbf{x}} \tilde{\hat{f}}_1\|) = \epsilon^2 / \left(\|\nabla_{\mathbf{x}} \tilde{\hat{f}}_1\|^2 + \epsilon^2\right)^{3/2}$. It is clear that $\mathfrak{L}``$ does not vanish for small values of $\|\nabla_{\mathbf{x}} \tilde{\hat{f}}_1\|$ which is severe and is against all the formulations and analysis that has been done. Additionally, we have

$\mathfrak{L}'(\cdot) < 1$ for small values of $\|\nabla_{\mathbf{x}}\tilde{\hat{f}}_1\|$. The authors of [58] provided a mathematical analysis of the problem. They criticized the above mentioned alteration and developed a general adaptive LSM algorithm to deal with this problem. The conclusion of their result, applied to our problem here, is that one would resort to the sub-gradient of the objective function at these locations of non-differentiability. The sub-gradient means the gradient of the other differentiable terms in the objective function. In the implementation, this means that we simply set the value of the mean curvature $\kappa = 0,\ \forall\|\nabla_{\mathbf{x}}\tilde{\hat{f}}_1\| = 0$. In fact this is exactly what has been done in [57] as an ad-hoc remedy but turned out to be correct as provided in [58]. This is what we will follow in this thesis.

The evolution process by mean curvature in (3.13) is equivalent to a LSM evolution with speed $\nu_s = -\frac{\kappa}{\|\nabla_{\mathbf{x}}\tilde{\hat{f}}_1\|}$. Comparing this speed to that given by (3.5), it is apparent that the evolution is not fully under the mean curvature. The evolution becomes dependent on the curvature of the level sets and the magnitude of the derivatives [54] and is not acting anymore like morphological operators for noise removal [39]. Another mathematical aspect is that the curvature term κ is stiff, which means that it changes continuously and in an inconsistent way with changes in $\|\nabla_{\mathbf{x}}\tilde{\hat{f}}_1\|$. The authors in [57] have chosen to multiply the Euler–Lagrange equation by $\|\nabla_{\mathbf{x}}\tilde{\hat{f}}_1\|$ and thus (3.13) becomes

$$\hat{\mathbf{f}}_1^{(n+1)} = \left[\hat{\mathbf{f}}_1 + \Delta T\Big(\kappa\|\nabla_{\mathbf{x}}\tilde{\hat{f}}_1\| - \mu H^{\mathrm{T}}(H\hat{\mathbf{f}}_1 - \mathbf{f}_0)\|\nabla_{\mathbf{x}}\tilde{\hat{f}}_1\|\Big)\right]^{(n)}. \tag{3.17}$$

This newer model provides a stable (non-stiff) system which is analytically the same as (3.13) except for the smooth regions where $\|\nabla_{\mathbf{x}}\tilde{\hat{f}}_1\| = 0$. In their argument in [54], the authors found this modification to have another numerical advantage which is to have a larger time step ΔT that makes the process converge quickly. However, when $\|\nabla_{\mathbf{x}}\tilde{\hat{f}}_1\| = 0$ we cannot multiply both sides of the Euler–Lagrange equation by a zero quantity as they mentioned. This leads to the fact that all constant images become stationary points for the evolution process in (3.17). This means that the process will

be deemed convergent for the constant images because it cannot move in any gradient direction. The authors dealt with this problem by starting the evolution process with an initial estimate that is the output of other restoration techniques like the Wiener method. However the objective function is now multi-modal and the solution depends on the choice of the initial estimate. In this thesis we will have a different treatment that solves this problem.

The third problem is the calculation of μ given by (3.14). There are two associated problems which are the initialization of $\hat{f}_1^{(0)}$ and the computation of μ. One should start with an initial estimate that satisfies the data fidelity criterion and this might be a problem for some applications. However the real problem is the intimidating computational cost of (3.14) at every iteration. The common practice to deal with this problem is to rely on a fixed value for μ based on the user's experience with the problem. In general the choice of the regularization parameter for regularized techniques is always a problem. In our treatment we do not require exact equality to zero but rather minimization of the data fidelity criterion and hence we will use a fixed value for μ.

The last problem is the numerical methods of calculating the partial derivatives. It is assumed that the samples $\hat{f}_1[\mathbf{x}] = \tilde{\hat{f}}_1(\mathbf{x}), \quad \forall \mathbf{x} \in \Lambda$, and that Λ is rectangular. The case of rectangular grid is not applicable for applications that deal with non-rectangular grids, like demosaicking of color-filter-array and other similar applications. When we are dealing with a rectangular grid and we cannot find a model to relate $\tilde{\hat{f}}_1(\mathbf{x})$ to $\hat{f}_1[\mathbf{x}]$ then perhaps the assumption $\hat{f}_1[\mathbf{x}] = \tilde{\hat{f}}_1(\mathbf{x}), \quad \forall \mathbf{x} \in \Lambda$, combined with (3.15) would be the way to do. However, the powerful part in the total variation regularizer is that it is formulated in the continuous domain and the images that we perceive are continuous and so it makes a lot of sense to seek a reasonable realistic formulation other than $\hat{f}_1[\mathbf{x}] = \tilde{\hat{f}}_1(\mathbf{x}), \quad \forall \mathbf{x} \in \Lambda$, combined with (3.15). The proposed method here will show a new formulation for dealing with a realistic solution for this

problem.

3.6 Proposed variational formulation for grey-scale image up-sampling

In the last few sections, we dealt with the variational formulation for problems related to ours and discussed the associated numerical difficulties and approaches to solve them. We surveyed the previous variational formulations for image up-sampling and we found that their formulation is incomplete for the data fidelity criterion. In this section, we will provide a completely new treatment for the problem and provide new numerical approaches to improve some of the previous numerical treatments. As far as I know, my joint paper [59] provides the only complete variational formulation for the image up-sampling problem that involves two different sampling structures $(\Lambda,\ \Gamma)$ simultaneously in the formulation and the solution. I propose the following formulation for regularized grey-scale image up-sampling:

$$\boxed{\begin{aligned} &\hat{\mathbf{f}}_1 = \arg\min_{\mathbf{g}} \left\{ \lambda \int_{\mathcal{W}_T} \|\nabla_{\mathbf{x}}(g_\varphi)(\mathbf{x})\| d\mathbf{x} + \frac{1}{2}\|H\mathbf{g} - \mathbf{f}_2\|^2 \right\}, \\ &(g_\varphi)(\mathbf{x}) \triangleq \sum_{\mathbf{d}\in\Lambda} g[\mathbf{d}]\phi_{\text{dis}}(\mathbf{x}-\mathbf{d}),\ \forall \mathbf{x} \in \mathcal{W}_T, \\ &g \in \ell^2(\Lambda), \quad f_2 \in \ell^2(\Gamma), \quad (g_\varphi) \in L^2(\mathcal{W}_T). \end{aligned}} \tag{3.18}$$

The matrix H performs both the filtering by a digital filter $h[\mathbf{x}]$ defined on Λ and down-sampling from Λ to Γ. In this section we will assume that the impulse response of the filter $h[\mathbf{x}]$ is known. Finding $h[\mathbf{x}]$ is one of the topics of the next chapter. In this proposed formulation we define the continuous image that the total variation regularizer is dealing with to be the image that is displayed to the viewer. This displayed continuous image is reconstructed from the samples of the discrete image $\hat{f}_1[\mathbf{x}]$ by a display device. This display device is characterized by a modelling function

ϕ.

The minimization of (3.18) is obtained as the steady state solution of the PDE that is developed from the Euler–Lagrange equation similar to the treatment given by (3.12). This resulting PDE is solved using the LSM equation given by (3.4). I used two types of motions with different spatially-variant speeds are used that interact simultaneously to provide the solution for (3.18). These two motions are proposed to have speeds

$$\begin{aligned} \nu_s &= -\lambda\kappa, \\ \nu_d &= \frac{H^{\mathrm{T}}(H\hat{\mathbf{f}}_1 - \mathbf{f}_2)}{\|\nabla_{\mathbf{x}}\tilde{\hat{f}}_1(\mathbf{x})\|}, \end{aligned} \tag{3.19}$$

where H^{T} performs both the up-sampling operation from Γ to Λ followed by filtering with the time-reversal filter $h[-\mathbf{x}]$[1]. The parameter λ serves as a regularization parameter and will be set to a constant value according to the discussion in section 3.5. The numerical implementation of the artificial time derivative in the LSM is given by the forward Euler method. Hence these hybrid motions and the time derivative discretization provide my iterative up-sampling method as

$$\hat{\mathbf{f}}_1^{(n+1)} = \left[\hat{\mathbf{f}}_1 + \Delta T\Big(\lambda\|\nabla_{\mathbf{x}}(\hat{f}_{1_\varphi})\|\kappa - H^{\mathrm{T}}(H\hat{\mathbf{f}}_1 - \mathbf{f}_2)\Big)\right]^{(n)}, \tag{3.20}$$

The spatial partial derivatives are analytically derived in the spatial domain pro-

[1] H^{T} does not involve any DC gain ($\Lambda : \Gamma$). It is involved in an iterative filtering process an not a single stage interpolation.

viding the following:

$$
\begin{aligned}
(\hat{f}_{1_\varphi})_x(\mathbf{x}) &= \sum_{\mathbf{d}\in\Lambda} \hat{f}_1[\mathbf{d}]\phi_x(\mathbf{x}-\mathbf{d}),\\
(\hat{f}_{1_\varphi})_y(\mathbf{x}) &= \sum_{\mathbf{d}\in\Lambda} \hat{f}_1[\mathbf{d}]\phi_y(\mathbf{x}-\mathbf{d}),\\
(\hat{f}_{1_\varphi})_{xx}(\mathbf{x}) &= \sum_{\mathbf{d}\in\Lambda} \hat{f}_1[\mathbf{d}]\phi_{xx}(\mathbf{x}-\mathbf{d}),\\
(\hat{f}_{1_\varphi})_{yy}(\mathbf{x}) &= \sum_{\mathbf{d}\in\Lambda} \hat{f}_1[\mathbf{d}]\phi_{yy}(\mathbf{x}-\mathbf{d}),\\
(\hat{f}_{1_\varphi})_{xy}(\mathbf{x}) &= \sum_{\mathbf{d}\in\Lambda} \hat{f}_1[\mathbf{d}]\phi_{xy}(\mathbf{x}-\mathbf{d}),\\
&\forall \mathbf{x}\in\mathcal{W}_T.
\end{aligned}
\tag{3.21}
$$

It is clear that if we have an analytic continuous model ϕ for the display device that we are using, then we can compute the partial derivatives for all $\mathbf{x}\in\mathcal{W}_T$ and not only on Λ. If we inspect (3.21) we find that the value of the partial derivative at any position $\mathbf{x}\in\mathcal{W}_T$ is theoretically dependent on all the samples of $\hat{f}_1[\mathbf{d}]$. However, when $\phi(\mathbf{x}-\mathbf{d}), \quad \forall \mathbf{d}\in\Lambda$ forms a Riesz basis, then practically it decays quickly providing a compact support function, which is the case with practical display devices. Hence, one need only perform the summation in (3.21) for a small number of samples depending on the order of the accuracy required. This leads to the fact that we can numerically approximate (3.21) at points of Λ using a simple convolution process as follows:

$$
\begin{aligned}
(\varphi_{\hat{f}_1})_{(\cdot)}(\mathbf{d}) &= \hat{f}_1[\mathbf{d}] * h_{(\cdot)}[\mathbf{d}],\\
h_{(\cdot)}[\mathbf{d}] &= \phi_{(\cdot)}(\mathbf{d}),\ \mathbf{d}\in\Lambda.
\end{aligned}
\tag{3.22}
$$

The order of accuracy can be increased by letting $h_{(\cdot)}$ have more coefficients, but this will increase the computational cost. However, $\phi_{(\cdot)}$ decays fast and usually a few coefficients are sufficient.

We derive $h_{(\cdot)}$ for a typical CRT display device which is usually modelled by a

Gaussian function $\phi(\mathbf{x}) = \frac{1}{2\pi r^2} \exp\left(-\frac{\|\mathbf{x}\|^2}{2r^2}\right)$.

I proposed a new formulation for the grey-scale image up-sampling problem and derived its numerical solution scheme. This numerical scheme treats drawbacks in the similar formulation for other close problems like denoising and deblurring in the literature. The new formulation here assumes knowledge of the observation model and a given display device aperture. The design of the observation model and adaptation to the properties of the display device aperture for the grey-scale image up-sampling problem will be dealt with in the next chapter.

Chapter 4

Observation Model for Regularized Image Up-sampling

A moving average filter is often used as an observation model for regularized image up-sampling. This chapter investigates whether this is a correct and accurate model for most circumstances, and investigates the feasibility of other options. In this chapter I present a novel theoretical analysis of the regularized image up-sampling problem focusing on the data fidelity term. I start with the formulation of the physical acquisition processes the image has undergone and develop a generalized design for the correct and accurate data fidelity term for regularized image up-sampling.

4.1 Introduction

According to the problem formulation in section 2.2, a continuous image is acquired by a physical camera to produce a lower-resolution (LR) image(s). The physical camera is modelled as a continuous-space(-time) filter followed by sampling on a lower-density sampling lattice. It is desired to obtain a higher-resolution (HR) version of that image sampled on a denser sampling lattice. The HR image is obtained, in principle, from the continuous image through a theoretical, and not necessarily a physically realizable,

camera specifying desired properties of the image. The scenario is shown in Fig. 4.1. The theoretical camera is also modelled as a continuous-space(-time) filter followed by sampling on a denser sampling lattice. Our focus, in this chapter, is to find and design an observation model that can best produce the LR image from the HR image. This observation model is used in the data fidelity term $\mathcal{J}_d$ for the regularized up-sampling process. We study the possibility of obtaining such observation models for any scenario for both cameras. The results presented in this chapter are for some existing physical cameras and arbitrary theoretical cameras. As far as I know, our paper [60] is the first to perform this study and offer a generalized design of this observation filter for arbitrary scenarios. Image up-sampling and super-resolution is an ill-posed problem that can be solved by combining a data fidelity term $\mathcal{J}_d$ with a regularization term $\mathcal{J}_s$. Much research has focused on the regularization term, which might involve different *a priori* constraints, to pick one solution with desirable properties from the infinite number of possible solutions. A data fidelity metric $\mathcal{J}_d$ used for most image interpolation and super-resolution research [61, 36, 62, 63] is the special case proposed in [6]. Their model supposed that the LR image was obtained from the continuous image by a CCD camera whose aperture is modelled by a rect function [11]. If the HR image is also obtained by a rect aperture, then the modelling observation filter is the discrete moving average.

The motivation in pursuing this study is that an accurate data observation model leads to a better definition of the solution space which is indeed a critical factor for a better quality up-sampling [64]. Our analysis involves continuous and discrete signals at different rates and sampling aliasing; thus we chose the frequency domain analysis. Tsai and Huang [65] provided a frequency domain analysis relating the HR image and a group of translated LR images. However, they did not consider the aperture physical degradation and assumed it to be a unit sample impulse. We have performed the design in an optimization framework and also used a power spectral density model

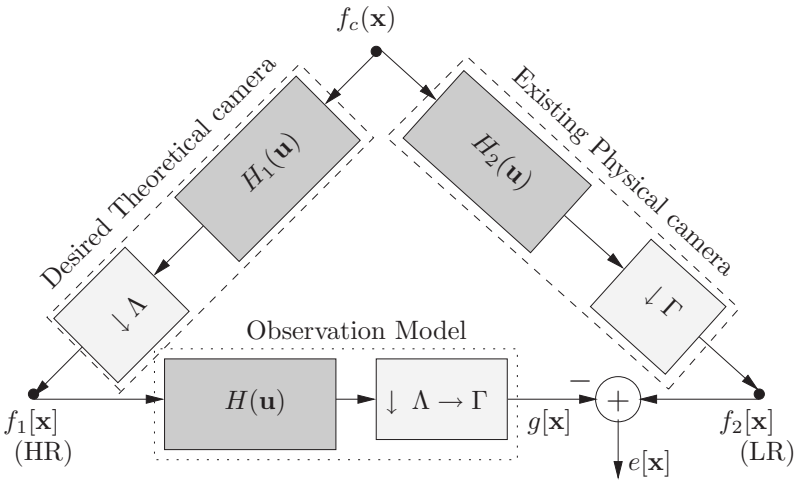

Fig. 4.1 Scenario for image up-sampling.

(PSD) for the continuous image.

4.2 Problem statement

Let $f_c(\mathbf{x})$ be a continuous-space(-time) image that is sampled on two different lattices Λ and Γ. We assume that $\Gamma \subset \Lambda$, and so $\Lambda^* \subset \Gamma^*$. The superscript * denotes the reciprocal lattice. In cases where neither Λ nor Γ is a subset of the other, then an intermediate lattice is introduced as in rate conversion by a rational factor, as discussed in section 2.1.6. The sampling aperture impulse responses for sampling on Λ and Γ are $h_1(\mathbf{x})$ and $h_2(\mathbf{x})$ respectively, yielding the sampled images $f_1[\mathbf{x}]$ and $f_2[\mathbf{x}]$. We seek a model to relate $f_2[\mathbf{x}]$ to $f_1[\mathbf{x}]$. The situation is illustrated in Fig. 4.1 where $g[\mathbf{x}]$ is the model of $f_2[\mathbf{x}]$ and $e[\mathbf{x}] = f_2[\mathbf{x}] - g[\mathbf{x}]$ is the modelling error. Here, $g[\mathbf{x}]$ is assumed to be obtained by LSI filtering of $f_1[\mathbf{x}]$ on Λ, followed by down-sampling to Γ.

4.3 Design of the observation model

Assume that $f_c(\mathbf{x})$ has a continuous-space Fourier transform $F_c(\mathbf{u})$. According to (2.7), then $f_1[\mathbf{x}]$ and $f_2[\mathbf{x}]$ are related to $f_c(\mathbf{x})$ in the frequency domain by

$$\begin{aligned} F_1(\mathbf{u}) &= \frac{1}{d(\Lambda)} \sum_{\mathbf{r}\in\Lambda^*} F_c(\mathbf{u}+\mathbf{r}) H_1(\mathbf{u}+\mathbf{r}) \\ F_2(\mathbf{u}) &= \frac{1}{d(\Gamma)} \sum_{\mathbf{s}\in\Gamma^*} F_c(\mathbf{u}+\mathbf{s}) H_2(\mathbf{u}+\mathbf{s}) \end{aligned} \tag{4.1}$$

where $d(\cdot)$ is the unit-cell volume of its argument lattice. If we denote $\frac{d(\Gamma)}{d(\Lambda)} = \frac{d(\Lambda^*)}{d(\Gamma^*)} =$ by $(\Lambda : \Gamma)$, then $\Gamma^* = \bigcup_{k=1}^{(\Lambda:\Gamma)} (\Lambda^* + \mathbf{d}_k)$ where $\mathbf{d}_k \in \Gamma^*, k = 1, \ldots, (\Lambda : \Gamma)$ are the coset representatives of Λ^* in Γ^* as discussed in section 2.1.1. From (2.12), it follows that

$$G(\mathbf{u}) = \frac{1}{(\Lambda : \Gamma)} \sum_{k=1}^{(\Lambda:\Gamma)} F_1(\mathbf{u}+\mathbf{d}_k) H(\mathbf{u}+\mathbf{d}_k). \tag{4.2}$$

Since $H(\mathbf{u}+\mathbf{r}) = H(\mathbf{u})$ for any $\mathbf{r} \in \Lambda^*$ and if we substitute from (4.1) into (4.2), then it follows that (4.2) can be written as

$$G(\mathbf{u}) = \frac{1}{d(\Gamma)} \sum_{\mathbf{s}\in\Gamma^*} F_c(\mathbf{u}+\mathbf{s}) H_1(\mathbf{u}+\mathbf{s}) H(\mathbf{u}+\mathbf{s}). \tag{4.3}$$

Thus, $g[\mathbf{x}]$ can be obtained in one step by filtering $f_c(\mathbf{x})$ with the LSI continuous-space(-time) filter whose frequency response is $H_1(\mathbf{u})H(\mathbf{u})$ and sampling on Γ. It should be noted that $H_1(\mathbf{u})$ is aperiodic while $H(\mathbf{u})$ is periodic, because h_1 is a continuous filter while h is a digital one. We can also write the Fourier transform of the error $e[\mathbf{x}]$ as

$$E(\mathbf{u}) = \frac{1}{d(\Gamma)} \sum_{\mathbf{s}\in\Gamma^*} F_c(\mathbf{u}+\mathbf{s}) \Big(H_2(\mathbf{u}+\mathbf{s}) - H_1(\mathbf{u}+\mathbf{s}) H(\mathbf{u}+\mathbf{s}) \Big). \tag{4.4}$$

Thus, $e[\mathbf{x}]$ can be obtained by filtering $f_c(\mathbf{x})$ with the LSI continuous-space(-time) filter whose frequency response is $H_2(\mathbf{u}) - H_1(\mathbf{u})H(\mathbf{u})$ followed by sampling on Γ.

If we assume that $f_c(\mathbf{x})$ is a realization of a continuous-space(-time) stationary random field with power spectral density (PSD) $S_f(\mathbf{u})$, then the error $e[\mathbf{x}]$ is a realization of a discrete-space stationary random field with PSD that can be written as given in [3] by

$$\begin{aligned} S_e(\mathbf{u}) =& \frac{1}{d(\Gamma)} \sum_{\mathbf{s}\in\Gamma^*} S_f(\mathbf{u}+\mathbf{s}) \\ & \times |H_2(\mathbf{u}+\mathbf{s}) - H_1(\mathbf{u}+\mathbf{s})H(\mathbf{u}+\mathbf{s})|^2. \end{aligned} \tag{4.5}$$

The corresponding mean square error (MSE) is

$$\begin{aligned} \sigma_e^2 =& \int_{\mathcal{P}_{\Gamma^*}} S_e(\mathbf{u}) d\mathbf{u} \\ =& \frac{1}{d(\Gamma)} \sum_{\mathbf{s}\in\Gamma^*} \int_{\mathcal{P}_{\Gamma^*}} S_f(\mathbf{u}+\mathbf{s}) \\ & \times |H_2(\mathbf{u}+\mathbf{s}) - H_1(\mathbf{u}+\mathbf{s})H(\mathbf{u}+\mathbf{s})|^2 d\mathbf{u}. \end{aligned} \tag{4.6}$$

Thus the best modelling filter $H_0(\mathbf{u})$ in the MSE sense satisfies

$$\mathbf{h_0} = \arg\min_{\mathbf{h}} \sigma_e^2 \tag{4.7}$$

where $H(\mathbf{u}) = \Sigma_{\mathbf{x}\in\Lambda} h[\mathbf{x}] \exp(-j2\pi\mathbf{u}\cdot\mathbf{x})$ which is a finite sum for FIR filters, and real for zero-phase filters. We can assume that the integrals in (4.6) are non-negligible for only a few $\mathbf{s} \in \Gamma^*$ in the vicinity of $\mathbf{u} = \mathbf{0}$. This is reasonable because the aperiodic frequency response of the continuous filters $H_1(\mathbf{u})$ and $H_2(\mathbf{u})$ will decay rapidly in the neighborhood of $P_{\Lambda^*}, P^*_{\Gamma}$, respectively. This is dictated by the physical aperture prefilter characteristics in cutting down aliasing. Fixing some number N of independent coefficients for $H(\mathbf{u})$, σ_e^2 is just a real function of the N unknowns, and

our objective function (4.6) can be minimized with a general optimization routine, or optimized analytically since it can be written as a quadratic form in $h[\mathbf{n}]$.

4.4 Analytic optimization

While the provided general formulation is applicable to 2 or 3 dimensions, we now consider the specific case of spatial (2-D) image up-sampling. Assume that Λ is a lattice that admits quadrantal symmetry [66]. Suppose $h[\mathbf{x}]$ has quadrantal symmetry, and the independent coefficients[1] ($h'[\mathbf{x}]$) are in the quadrant $\mathcal{Q}$, so that $H(\mathbf{u}) = \sum_{\mathbf{x}\in\mathcal{Q}} h'[\mathbf{x}]\cos(2\pi ux)\cos(2\pi vy)$. If $H_1(\mathbf{u})$ and $H_2(\mathbf{u})$ are real, then expanding the terms of (4.6) yields

$$\begin{aligned}
\sigma_e^2 =& \frac{1}{d(\Gamma)}\sum_{\mathbf{s}\in\Gamma^*}\int_{\mathcal{P}_{\Gamma^*}} S_f(\mathbf{u}+\mathbf{s})H_2^2(\mathbf{u}+\mathbf{s})d\mathbf{u} \\
&- \frac{2}{d(\Gamma)}\sum_{\mathbf{x}\in\mathcal{Q}} h'[\mathbf{x}]\sum_{\mathbf{s}\in\Gamma^*}\int_{\mathcal{P}_{\Gamma^*}}\Big[S_f(\mathbf{u}+\mathbf{s})H_1(\mathbf{u}+\mathbf{s}) \\
&\times H_2(\mathbf{u}+\mathbf{s})\cos(2\pi(u+s_x)x)\cos(2\pi(v+s_y)y)\Big]d\mathbf{u} \\
&+ \frac{1}{d(\Gamma)}\sum_{\mathbf{x}\in\mathcal{Q}}\sum_{\breve{\mathbf{x}}\in\mathcal{Q}} h'[\mathbf{x}]h'[\breve{\mathbf{x}}]\sum_{\mathbf{s}\in\Gamma^*}\int_{\mathcal{P}_{\Gamma^*}}\Big[S_f(\mathbf{u}+\mathbf{s}) \\
&\times H_1^2(\mathbf{u}+\mathbf{s})\cos(2\pi(u+s_x)x)\cos(2\pi(v+s_y)y) \\
&\times \cos(2\pi(u+s_x)\breve{x})\cos(2\pi(v+s_y)\breve{y})\Big]d\mathbf{u}
\end{aligned} \tag{4.8}$$

where, $\mathbf{s} = [s_x, s_y]^{\mathrm{T}}$. If we stack $h'[\mathbf{x}]$ into a lexicographic vector $\mathbf{h}'[\mathbf{x}]$, then (4.8) can be simply written as

$$\sigma_e^2 = \mathbf{h'}^{\mathrm{T}} D\mathbf{h'} + \mathbf{b}^{\mathrm{T}}\mathbf{h'} + c \tag{4.9}$$

[1] Recall from section 2.1 that for $D = 2$, $\mathbf{x} = [x\ y]^{\mathrm{T}}$

where the elements of the vector $\mathbf{b}$ and the matrix D can be determined by numerical integration. Then, σ_e^2 is easily minimized with

$$\boxed{\mathbf{h'}_0 = -\frac{1}{2}D^{-1}\mathbf{b}.} \tag{4.10}$$

4.5 Power spectral density model of the image

Several models for the PSD of the continuous image $S_f(\mathbf{u})$ exist. In the estimation of $S_f(\mathbf{u})$ I used parametric and non-parametric methods.

4.5.1 Parametric model for PSD estimation

Since $S_f(\mathbf{u}) \triangleq F.T\{R_f(\mathbf{x})\}$, I used the basic model for the autocorrelation of continuous images defined by $R_f(x,y) \triangleq \sigma^2 \exp(-\alpha_1|x|)\exp(-\alpha_2|y|)$, where $\sigma^2 = R_f(0,0)$ is the autocorrelation with zero lag and α_1, α_2 are parameters. Calculating the 2-D Fourier transform of $R_f(x,y)$ and extending one of the 1-D Fourier transform formulas in [67], I derived the PSD to be

$$S_f(u,v) = 4\sigma^2 \frac{\alpha_2}{4\pi^2 v^2 + \alpha_2^2} \frac{\alpha_1}{4\pi^2 u^2 + \alpha_1^2}. \tag{4.11}$$

A plot for the estimated PSD for $\alpha_1 = \alpha_2 = 0.98$ is given in Fig. 4.2(a).

4.5.2 Non-parametric PSD estimation

In our simulations we used the Welch-modified periodogram method [9], using a Blackman-Harris window, to estimate the PSD from a very high resolution image of size 3390×2436. The window size was 64 with 8 samples of overlap. The estimated PSD $S_f(\mathbf{u})$ is given in Fig. 4.2(b).

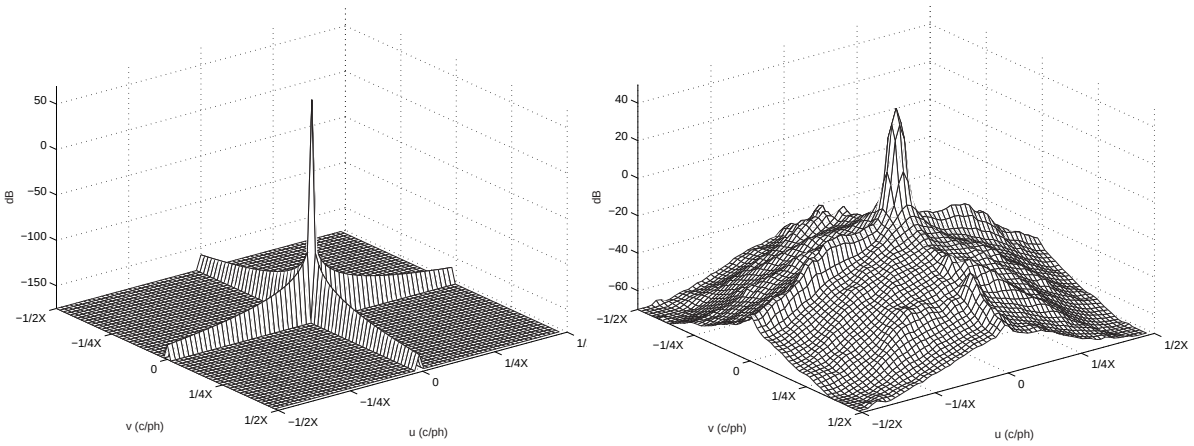

(a) (b)

Fig. 4.2 Image power spectral density estimates $S_f(\mathbf{u})$ by two different methods. (a) parametric estimate from an auto-correlation model (b)Welch-modified periodogram.

4.6 Simulations and experiments

The impulse responses of most physical camera apertures are modelled by a 2-D Gaussian, rect, or circ function. Hence, I designed the basic experiment scenarios with the Gaussian and rect functions for H_2. I will name each scenario according to the aperture used for H_1 and H_2 respectively and the value of $(\Lambda : \Gamma)$; in other words if H_1 is a Gaussian, H_2 is a rect function, and $(\Lambda : \Gamma) = 25$, then we call it Gauss-Rect($\downarrow 25$). The sample scenarios in this section are Gauss-Gauss($\downarrow 25$), Rect-Rect($\downarrow 25$), Rect-Gauss($\downarrow 25$), and Gauss-Rect($\downarrow 25$). The sampling lattices are given by $V_\Lambda = \mathrm{diag}(X, X)$ and $V_\Gamma = \mathrm{diag}(5X, 5X)$. For each scenario I obtained an FIR modelling filter $h[\mathbf{x}]$ described in the first row in Table 4.1. Inspecting the magnitude of the frequency response of the modelling filters obtained for different scenarios, we can observe the following:

1. We only obtained the moving average filter as a modelling filter for the scenario Rect-Rect($\downarrow 25$).

2. For the Rect-Gauss($\downarrow 25$) and Gauss-Gauss($\downarrow 25$) scenarios we obtained modelling filters which are far from being a moving average filter.

3. The magnitude of the frequency response of the modelling filters obtained for scenarios having the same filter H_2 tends to have close characteristics in their passband, while the stopband shape is different. This is clear by comparing Fig. 4.4(a) and Fig. 4.4(b).

4. The major difference among modelling filters obtained for different scenarios is mainly in the stopband. This is due to the aliasing components introduced by the down-sampling process involved.

A general conclusion is that using an incorrect modelling filter in the observation model for image up-sampling problem will have its greatest impact in measuring the high frequency components but it will not deviate much in measuring the low frequency components.

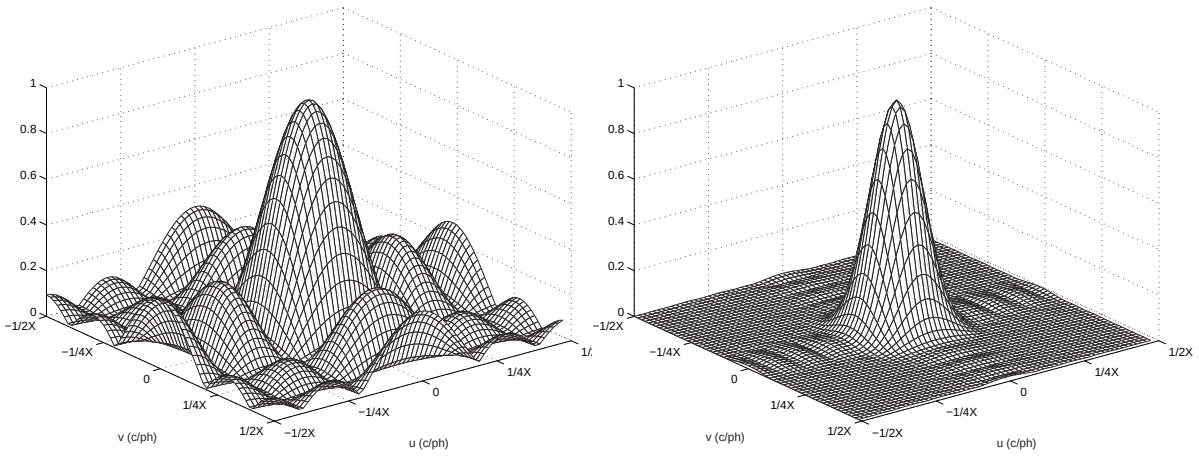

(a) (b)

Fig. 4.3 Magnitude of the frequency response for the observation model $H(\mathbf{u})$ for two scenarios. (a) Gauss-Rect ($\downarrow 25$), (b) Rect-Gauss ($\downarrow 25$).

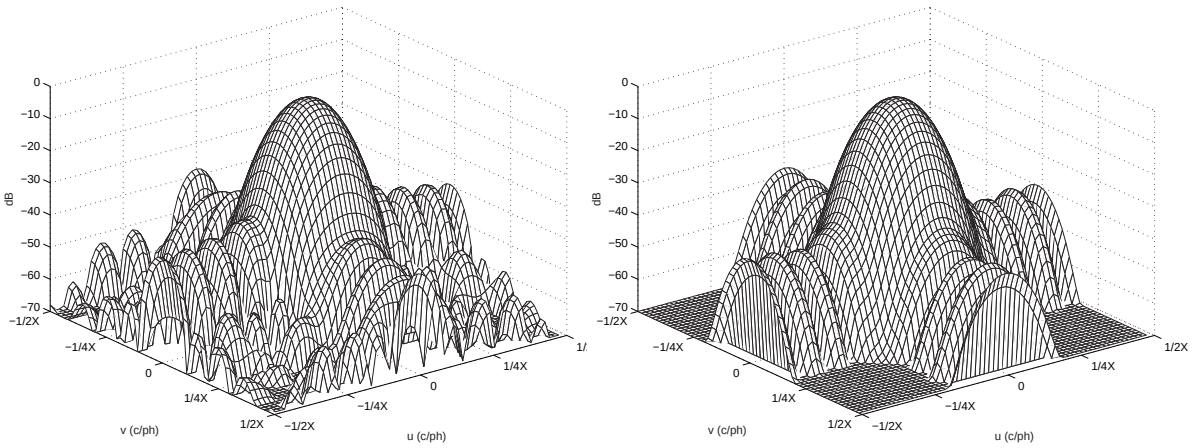

(a) (b)

Fig. 4.4 Magnitude of the frequency response for the observation model $H(\mathbf{u})$ for two scenarios in (dB). (a) Rect-Gauss ($\downarrow 25$), (b) Gauss-Gauss ($\downarrow 25$).

In order to verify the results obtained I ran a simulation of each scenario and used the modelling filter obtained to measure the actual modelling error $e[\mathbf{x}]$ on the images as follows:

1. Start with a very high resolution image simulating the continuous signal $f_c(\mathbf{x})$.

2. Select two large sub-sampling factors to simulate the ratio between Λ and Γ.

3. Simulate $h_1(\mathbf{x})$ and $h_2(\mathbf{x})$ by the appropriate digitally designed Gaussian or moving average filter. For Gaussian filters we can choose the appropriate cut-off angular frequency as given in [4], in accordance with the chosen sub-sampling factor(s).

4. The very-high-resolution image is filtered by $h_1(\mathbf{x})$ and $h_2(\mathbf{x})$ providing 2 filtered versions of $f_c(\mathbf{x})$.

5. Down-sample the filtered images by the chosen sub-sampling factors. The images obtained are used to simulate $f_1[\mathbf{x}]$ and $f_2[\mathbf{x}]$. The large down-sampling factors

are used to minimize the error between the digital simulation and the reality of the continuous spectrum analysis, simulating the sampling on both lattices Λ and Γ, respectively. We chose Λ and Γ to be rectangular for the basic experiments, where $\Lambda = \mathrm{LAT}(\mathrm{diag}(X, Y))$.

6. Obtain $g[\mathbf{x}]$ by filtering $f_1[\mathbf{x}]$ with $h[\mathbf{x}]$, obtained in different ways, followed by down-sampling from Λ to Γ.

7. Measure the actual modelling error $e[\mathbf{x}] = f_2[\mathbf{x}] - g[\mathbf{x}]$.

8. Compute the peak-signal-to-noise ratio (PSNR) using $e[\mathbf{x}]$.

The computed PSNR value for each scenario is given in Table 4.1. For comparison's sake I also chose some reasonable filters to be the modelling filter $h[\mathbf{x}]$, and measured the actual modelling error. The simulations are repeated for each of these different choices of $h[\mathbf{x}]$ for the four basic scenarios. The chosen filters are as follows:

1. The moving average and the Gaussian filters because intuitively they seem to be suitable for some scenarios like the Rect-Rect and the Gauss-Gauss respectively.

2. A filter with maximally flat passband and monotonically decreasing transition and stopband. This filter was chosen because it produces images with no ringing artifacts while not compromising resolution as much as many other filters, like the Gaussian ones. I chose two filters with two different angular cut-off frequencies of $\pi/4$ and $\pi/8$ which are around the critical cut-off angular frequency $\pi/5$ for these case-study scenarios.

For all the Gaussian filters used as modelling filters, I optimized the variance that maximizes the PSNR of the result because I found that the results change drastically with the choice of the variance of this Gaussian function! The choice of the optimal variance of the Gaussian function was obtained by running a 1-D search that provides the maximum PSNR result for each scenario. The values of these optimal variances

for each scenario are given in the footnotes of Table 4.1. All the PSNR measures for all scenarios with all filters are shown in Table 4.1.

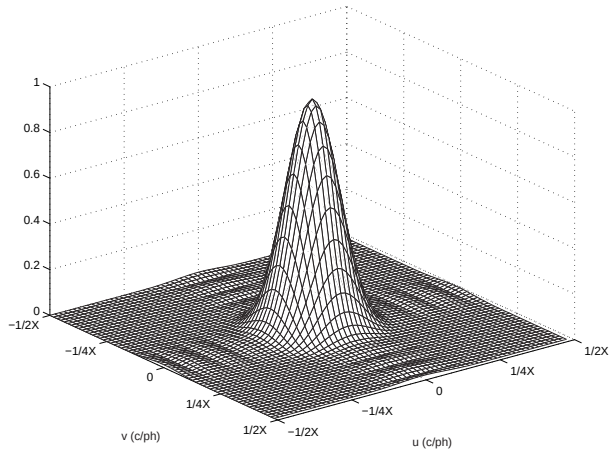

Fig. 4.5 Magnitude of the frequency response for the observation model $H(\mathbf{u})$ for Gauss-Gauss ($\downarrow 25$).

I wanted to obtain the upper bound on the PSNR value that can be obtained for this simulation for each scenario. I achieved this by obtaining a modelling filter using the images $f_1[\mathbf{x}]$ and $f_2[\mathbf{x}]$ themselves, and solving a numerical optimization problem, directly from the images. Here I used the least squares method because the problem is overdetermined. The problem is simply formulated as

$$h = \arg\min_{\breve{h}} \|\breve{H}\mathbf{f}_1 - \mathbf{f}_2\|^2, \tag{4.12}$$

where the matrix $\breve{H}$ performs both the filtering by the argument filter $\breve{h}$ and down-sampling from Λ to Γ. Thus, $\breve{H}$ is a block diagonal matrix formed from the coefficients of $\breve{h}$. The simulated modelling filter obtained was also used to compute the modelling error which appears in the first row of results in Table 4.1 and is named *simulated optimization*. This helped in obtaining an upper bound on the PSNR that can be obtained from the simulation experiment. However, it can't be practically used since

in real applications $f_1[\mathbf{x}]$ is not available, and it results in a modelling filter that is biased towards the specific features of the underlying image.

Comparing the results in Table 4.1 we observe the following:

1. In the Rect-Rect scenario, the result is almost a moving average filter to some numerical approximation which agrees with the result in [6]. The reason that we did not obtain exactly the moving average filter as a modelling filter is accounted for the following:

   (a) Numerical approximations that are involved in the numerical integration.

   (b) Simulation approximations as using H_1 and H_2 as discrete approximation of continuous-space filters and simulating the sampling process by sub-sampling with large factors.

   However, a PSNR of 58.39 as compared to 63.22 of the moving average is still a very good result and the difference in results cannot be distinguished by human eyes.

2. For the Gauss-Gauss scenario the method designed a Gaussian-like modelling filter with the optimized variance of the Gaussian function. The result is almost similar to the manually optimized Gaussian filter, which is a good indication on the performance of the method in this scenario. It should be noted that in practice we cannot manually optimize the variance of the Gaussian filter because the HR image f_1 is not available.

3. For the Rect-Gauss and the Gauss-Rect scenarios we obtained new modelling filters that are neither a simple moving average nor a Gaussian filter. Both of them failed to provide a reasonable performance in these scenarios.

We were able to formulate a generalized design for the observation model and succeeded in obtaining the optimal observation model for important scenarios in im-

age up-sampling and super-resolution. Furthermore, our method allows us to solve for any desired scenarios, e.g., standards conversion posing known physical specifications or up-sampling to images acquired with nice a theoretical aperture specifying desired properties of the image. With our optimal modelling filter tightening the relation between the HR and LR, we can cut down noise amplification during the regularized up-sampling process. This leads to relaxing the smoothness (regularization) constraint(s) and helps in obtaining less blurred (over smoothed) results, if a suitable regularizer is selected.

4.7 Design of the theoretical camera

We have been able to design the observation model, specifically $h[\mathbf{x}]$ for a given $h_2(\mathbf{x})$ and a chosen $h_1(\mathbf{x})$. The question is: what should we choose for $h_1(\mathbf{x})$? Recalling our main problem of image up-sampling in Fig. 2.5, we have not described or (constrained) the continuous image that will be further reconstructed (displayed) from $f_1[\mathbf{x}]$. In fact, the display device is an important factor in the overall perceived quality of the image. In this section we design the optimal prefilter for the theoretical camera ($h_1(\mathbf{x})$) for any given display reconstruction aperture. The design goal is to minimize the error in the least-squares sense between the original continuous signal $f_c(\mathbf{x})$ and the displayed continuous signal $\tilde{f}_1(\mathbf{x})$. The continuous signal $\tilde{f}_1(\mathbf{x})$ is reconstructed by the display device from the samples $f_1[\mathbf{x}]$. The scenario is depicted in Fig. 4.6. In [68] I extended Unser's formulation for finding this prefilter [14] to arbitrary lattice structures, not necessarily rectangular. The optimization problem that is to be addressed in this

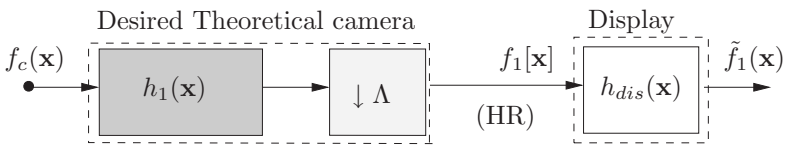

Fig. 4.6 Design of the theoretical camera.

section is given by

$$\begin{aligned} h_1 &= \arg\min_{\check{h}} \|\tilde{f}_1 - f_c\|^2, \\ \text{where } \tilde{f}_1(\mathbf{x}) &= \sum_{\mathbf{d}\in\Lambda} f_1[\mathbf{d}]\phi(\mathbf{x}-\mathbf{d}),\ \forall \mathbf{x} \in \mathbb{R}^D, \\ \text{and } f_1[\mathbf{x}] &= \big(\check{h} * f_c\big)(\mathbf{x}),\ \mathbf{x} \in \Lambda. \end{aligned} \tag{4.13}$$

In order to proceed with the optimization problem (4.13), we need first to introduce some definitions and then proceed with the solution.

4.7.1 Riesz basis on arbitrary lattice

In this section we will focus on the properties of the Riesz basis for arbitrary sampling structures. Unser [14] discussed these properties of the Riesz basis for integer translates of a given function on $\mathbb{Z}$. The extension for orthogonal lattice (cartesian grid) with separability is straightforward. The authors in [69] followed the same discussion for the properties of the Riesz basis for hexagonal lattices. A further safeguard condition was introduced in [14] and was also used in [69] that will be discussed in the next section.

From (4.13), we see that the displayed image is a linear combination of shifted versions of the display's unit-sample response, where all the shifts lie in the sampling lattice Λ. Assume that the input image has finite energy, $f_c \in L^2(\mathbb{R}^D)$. Let $\mathcal{T}_{\mathbf{d}}$ be the shift operator on $L^2(\mathbb{R}^D)$, such that $\mathcal{T}_{\mathbf{d}} f_c(\mathbf{x}) = f_c(\mathbf{x}-\mathbf{d})$, and define $\phi_{\mathbf{d}} \triangleq \mathcal{T}_{\mathbf{d}}\phi$. We define the display subspace to be

$$\mathbf{V}(\phi,\Lambda) \triangleq \left\{ \sum_{\mathbf{d}\in\Lambda} c[\mathbf{d}]\phi_{\mathbf{d}} : c \in \ell^2(\Lambda) \right\}, \tag{4.14}$$

where the sampling structure of the theoretical camera is Λ as shown before in Fig. 4.1. Thus $\tilde{f}_1 \in \mathbf{V}(\phi,\Lambda)$ for all $f_1 \in \ell^2(\Lambda)$. Under mild conditions that hold for practical

display devices, the set $\{\phi_{\mathbf{d}} : \mathbf{d} \in \Lambda\}$ forms a Riesz basis for $\mathbf{V}(\phi, \Lambda)$. In the space(-time) domain, the condition is

$$\alpha\|f_1\|^2 \leq \left\|\sum_{\mathbf{d}\in\Lambda} f_1[\mathbf{d}]\phi_{\mathbf{d}}\right\|^2 \leq \beta\|f_1\|^2,\ \forall f_1 \in \ell^2(\Lambda), \tag{4.15}$$

where α and β are real numbers such that $0 < \alpha \leq \beta < \infty$ [70]. The corresponding frequency domain condition can be derived as follows:

$$\begin{aligned}
&\alpha \int_{\mathcal{P}_{\Lambda^*}} |F_1(\mathbf{u})|^2 d\mathbf{u} \leq \int_{\mathbb{R}^D} |F_1(\mathbf{u})|^2 |\Phi(\mathbf{u})|^2 d\mathbf{u} \leq \beta \int_{\mathcal{P}_{\Lambda^*}} |F_1(\mathbf{u})|^2 d\mathbf{u} \\
&\alpha \int_{\mathcal{P}_{\Lambda^*}} |F_1(\mathbf{u})|^2 d\mathbf{u} \leq \sum_{r\in\Lambda^*} \int_{\mathcal{P}_{\Lambda^*}} |F_1(\mathbf{u}+\mathbf{r})|^2 |\Phi(\mathbf{u}+\mathbf{r})|^2 d\mathbf{u} \leq \beta \int_{\mathcal{P}_{\Lambda^*}} |F_1(\mathbf{u})|^2 d\mathbf{u} \\
&\alpha \int_{\mathcal{P}_{\Lambda^*}} |F_1(\mathbf{u})|^2 d\mathbf{u} \leq \int_{\mathcal{P}_{\Lambda^*}} |F_1(\mathbf{u})|^2 \Big|\sum_{r\in\Lambda^*} \Phi(\mathbf{u}+\mathbf{r})\Big|^2 d\mathbf{u} \leq \beta \int_{\mathcal{P}_{\Lambda^*}} |F_1(\mathbf{u})|^2 d\mathbf{u} \\
&\qquad \forall \mathbf{u} \in \mathbb{R}^D.
\end{aligned} \tag{4.16}$$

It should be noted that $F_1(\mathbf{u})$ is periodic with periodicity of $\mathcal{P}_{\Lambda^*}$, while $\Phi(\mathbf{u})$ is aperiodic. Hence a sufficient condition is to have

$$\alpha \leq \sum_{r\in\Lambda^*} |\Phi(\mathbf{u}+\mathbf{r})|^2 \leq \beta,\ \forall \mathbf{u} \in \mathbb{R}^D, \tag{4.17}$$

as given in [14]. However, it can be shown that a necessary condition is

$$\grave{\alpha} \leq \sum_{r\in\Lambda^*} |\Phi(\mathbf{u}+\mathbf{r})|^2 \leq \grave{\beta},\ \forall \mathbf{u} \in \mathbb{R}^D, \tag{4.18}$$

for some $0 < \grave{\alpha} \leq \grave{\beta} < \infty$. Thus $\{\phi_{\mathbf{d}} : \mathbf{d} \in \Lambda\}$ forms a Riesz basis if and only if $\sum_{r\in\Lambda^*} |\Phi(\mathbf{u}+\mathbf{r})|^2$ is positive and finite $\forall \mathbf{u} \in \mathcal{P}_{\Lambda^*}$. This condition can easily be verified for any given display response ϕ. In other words, $\{\phi_{\mathbf{d}} : \mathbf{d} \in \Lambda\}$ forms a Riesz basis for $\mathbf{V}(\phi, \Lambda)$ if and only if $\sum_{\mathbf{r}\in\Lambda^*} |\Phi(\mathbf{u}+\mathbf{r})|^2$ is positive and bounded on any unit cell of Λ^*. The Riesz basis condition (4.15) ensures that the display transformation is stable

and that $\tilde{f}_1 \in L^2(\mathbb{R}^D)$ for all $f_1 \in \ell^2(\Lambda)$.

With this setup, our problem is to find, for each $f_c \in L^2(\mathbb{R}^D)$, the element $\tilde{f}_1 \in \mathbf{V}(\phi, \Lambda)$ such that $\|f_c - \tilde{f}_1\|^2$ is minimized; this is simply the projection of f_c onto $\mathbf{V}(\phi, \Lambda)$. In order to find the optimal $\tilde{f}_1$, we need the reciprocal basis (sometimes called the dual basis) for $\mathbf{V}(\phi, \Lambda)$ [71].

4.7.2 Minimum error sampling

The solution for the problem (4.13) is given through the framework of the theorems that will be developed in this section. These theorems generalize the result that was given in [14] to arbitrary sampling structure Λ. In addition I will prove that the solution also forms a Riesz basis for the generalized case; this part was given without proof for the 1-D case by [14].

Theorem 1 (Riesz bases on arbitrary lattices). *For any space $\mathbf{V}(\phi, \Lambda)$ on arbitrary lattice Λ with Riesz basis $\{\phi_{\mathbf{d}} : \mathbf{d} \in \Lambda\}$ there exists a reciprocal basis* [2] *$\{\overset{\circ}{\phi}_{\mathbf{e}} : \mathbf{e} \in \Lambda\}$ that form a Riesz basis that spans this space.*

Proof. Assume $\exists\ \overset{\circ}{\phi} \in \mathbf{V}(\phi, \Lambda)$ such that $\langle \overset{\circ}{\phi}, \phi_{\mathbf{d}} \rangle = \delta[\mathbf{d}], \forall \mathbf{d} \in \Lambda$.
Since $\overset{\circ}{\phi} \in \mathbf{V}(\phi, \Lambda)$, then it can be written as a linear combination of $\phi_{\mathbf{d}},\ \mathbf{d} \in \Lambda$, as

$$\overset{\circ}{\phi}(\mathbf{x}) = \sum_{\mathbf{g} \in \Lambda} p[\mathbf{g}] \phi(\mathbf{x} - \mathbf{g}) \overset{\text{F.T.}}{\leftrightarrow} \overset{\circ}{\Phi}(\mathbf{u}) = P(\mathbf{u}) \Phi(\mathbf{u}), \tag{4.19}$$

where $P(\mathbf{u})$ is periodic and $\Phi(\mathbf{u})$ is aperiodic. From the above condition on $\overset{\circ}{\phi}$ we get $\langle \sum_{\mathbf{g} \in \Lambda} p[\mathbf{g}] \phi_{\mathbf{g}}, \phi_{\mathbf{d}} \rangle = \delta[\mathbf{d}]$, which can be written as

$$\sum_{\mathbf{g} \in \Lambda} p[\mathbf{g}] \langle \phi_{\mathbf{g}}, \phi_{\mathbf{d}} \rangle = \delta[\mathbf{d}].$$

[2] Reciprocal basis means that $\langle \overset{\circ}{\phi}_{\mathbf{e}}, \phi_{\mathbf{d}} \rangle = \delta[\mathbf{d} - \mathbf{e}]\ \forall \mathbf{d}, \mathbf{e} \in \Lambda$ [71].

The inner product in the above expression is simply the autocorrelation of ϕ at $\mathbf{d}-\mathbf{g}$ which will be denoted as $\mathcal{R}_\phi[\mathbf{d}-\mathbf{g}]$. Then it follows that what we have is just a convolution $(p * \mathcal{R}_\phi)[\mathbf{d}] = \delta[\mathbf{d}]$. Taking the Fourier transform on Λ for both sides we get

$$P(\mathbf{u})\frac{1}{d(\Lambda)}\sum_{\mathbf{r}\in\Lambda^*}|\Phi(\mathbf{u}+\mathbf{r})|^2 = 1$$
$$\Longrightarrow P(\mathbf{u}) = \frac{1}{\frac{1}{d(\Lambda)}\sum_{\mathbf{r}\in\Lambda^*}|\Phi(\mathbf{u}+\mathbf{r})|^2}.$$

Since the denominator is finite and non-zero (by definition of the Riesz basis (4.18)), then $P(\mathbf{u})$ exists and $0 < P(\mathbf{u}) < \infty,\ \forall \mathbf{u} \in \mathcal{P}_{\Lambda^*}$. This proves that the assumption that there exists $\overset{\circ}{\phi} \in \mathbf{V}(\phi,\Lambda)$ holds and further more $\overset{\circ}{\phi}$ is unique. By the translation-invariant nature of $\mathbf{V}(\phi,\Lambda)$, then we have $\overset{\circ}{\phi}_{\mathbf{e}} \in \mathbf{V}(\phi,\Lambda),\ \forall \mathbf{e} \in \Lambda$. From the orthogonality above it follows easily that $\langle \overset{\circ}{\phi}_{\mathbf{e}}, \phi_{\mathbf{d}} \rangle = \delta[\mathbf{d}-\mathbf{e}]$.
Substituting for $P(\mathbf{u})$ in (4.19) we get

$$\overset{\circ}{\Phi}(\mathbf{u}) = \frac{\Phi(\mathbf{u})}{\frac{1}{d(\Lambda)}\sum_{\mathbf{r}\in\Lambda^*}|\Phi(\mathbf{u}+\mathbf{r})|^2}. \tag{4.20}$$

To prove that $\{\overset{\circ}{\phi}_{\mathbf{e}} : \mathbf{e} \in \Lambda\}$ forms a Riesz basis we can evaluate the summation $\sum_{\mathbf{s}\in\Lambda^*}|\overset{\circ}{\Phi}(\mathbf{u}+\mathbf{s})|^2$ and verify that it satisfies (4.18). Since the denominator of the R.H.S. in (4.20) is finite and positive then it follows that

$$\sum_{\mathbf{s}\in\Lambda^*}|\overset{\circ}{\Phi}(\mathbf{u}+\mathbf{s})|^2 = \frac{1}{\left(\frac{1}{d(\Lambda)}\sum_{\mathbf{r}\in\Lambda^*}|\Phi(\mathbf{u}+\mathbf{r})|^2\right)^2}\sum_{\mathbf{s}\in\Lambda^*}|\Phi(\mathbf{u}+\mathbf{s})|^2$$
$$= \frac{(d(\Lambda))^2}{\sum_{\mathbf{r}\in\Lambda^*}|\Phi(\mathbf{u}+\mathbf{r})|^2}.$$

It is clear that the result is finite and positive. This implies that $\{\overset{\circ}{\phi}_{\mathbf{e}}\}$ is a Riesz basis.

Finally, we need to prove that $\text{span}(\overset{\circ}{\phi}_{\mathbf{e}}) = \mathbf{V}(\phi,\Lambda)$. Any function $\tilde{f} \in \mathbf{V}(\phi,\Lambda)$ can

be written as $\tilde{f} = \sum_{\mathbf{d}\in\Lambda} c[\mathbf{d}]\phi_{\mathbf{d}}$, where $c[\mathbf{d}] = \langle \tilde{f}, \overset{\circ}{\phi}_{\mathbf{d}} \rangle$ [71].
Hence,

$$\sum_{\mathbf{d}\in\Lambda} \langle \tilde{f}, \phi_{\mathbf{d}} \rangle \overset{\circ}{\phi}_{\mathbf{d}} = \sum_{\mathbf{d}\in\Lambda} (c * \mathcal{R}_{\phi})[\mathbf{d}] \overset{\circ}{\phi}_{\mathbf{d}}.$$

The R.H.S. can be shown to be equal to $\tilde{f}$ in the frequency domain by taking the Fourier transform of the R.H.S. and substituting for $\overset{\circ}{\Phi}(\mathbf{u})$ from (4.20). Therefore, we can write $\tilde{f} = \sum_{\mathbf{d}\in\Lambda} \langle \tilde{f}, \phi_{\mathbf{d}} \rangle \overset{\circ}{\phi}_{\mathbf{d}}$. This means that any function in $\mathbf{V}(\phi, \Lambda)$ can be uniquely written as a linear combination of $\{\overset{\circ}{\phi}_{\mathbf{e}}\}$. This completes the proof. □

We arrived at a result that the reciprocal basis for $V(\phi, \Lambda)$ has the same form $\{\overset{\circ}{\phi}(\mathbf{x} - \mathbf{d}) : \mathbf{d} \in \Lambda\}$ and $\overset{\circ}{\phi}$ is given by (4.20). Now we are ready to find the solution of (4.13). This will be done in the framework of the following theorem.

Theorem 2 (Minimum error sampling on arbitrary lattice). *If a continuous-space(-time) signal $f_c \in L^2(\mathbb{R}^D)$ is sampled on a lattice Λ with a prefilter $h_1(\mathbf{x})$ and the result is displayed with aperture $\phi(\mathbf{x})$ as shown in Fig. 4.6, then the prefilter $h_1(\mathbf{x})$ that minimizes $\|f_c - \tilde{f}_1\|^2$ has frequency response*

$$\boxed{H_1(\mathbf{u}) = \frac{\Phi^*(\mathbf{u})}{\frac{1}{d(\Lambda)} \sum_{\mathbf{r}\in\Lambda^*} |\Phi(\mathbf{u} + \mathbf{r})|^2}} \tag{4.21}$$

Proof. The minimization of the error $\|f_c - \tilde{f}_1\|^2$ is determined by the projection theorem [71] using an orthogonal projection $\mathfrak{P}_{\mathbf{V}(\phi,\Lambda)} : L^2(\mathbb{R}^D) \to \mathbf{V}(\phi, \Lambda)$. This projection of f_c onto $\mathbf{V}(\phi, \Lambda)$ is given by $\mathfrak{P}_{\mathbf{V}(\phi,\Lambda)} f_c = \tilde{f}_1 = \sum_{\mathbf{d}\in\Lambda} \langle f_c, \overset{\circ}{\phi}_{\mathbf{d}} \rangle \phi_{\mathbf{d}}$. This projection can be conceptually implemented by three operations:

1. computation of $\langle f_c, \overset{\circ}{\phi}_{\mathbf{g}} \rangle$, $\forall \mathbf{g} \in \mathbb{R}^D$ which is equivalent to LSI filtering of f_c with $h_1(\mathbf{x}) = \overset{\circ}{\phi}(-\mathbf{x})$. For a given display aperture ϕ this filter is given in terms of the reciprocal basis by Theorem 1 as $H_1(\mathbf{u}) = \frac{\Phi^*(\mathbf{u})}{\frac{1}{d(\Lambda)} \sum_{\mathbf{r}\in\Lambda^*} |\Phi(\mathbf{u}+\mathbf{r})|^2}$;

2. sampling of $\left(\langle f_c, \overset{\circ}{\phi}_{\mathbf{g}}\rangle\right),\ \forall \mathbf{g} \in \mathbb{R}^D$ on Λ. This corresponds to $f_1[\mathbf{d}] = \left(\langle f_c, \overset{\circ}{\phi}_{\mathbf{d}}\rangle\right),\ \forall \mathbf{d} \in \Lambda$;

3. synthesis of the displayed image $\sum_{\mathbf{d}\in\Lambda} f_1[\mathbf{d}]\phi_{\mathbf{d}}$.

□

Because $h_1(\mathbf{x}) = \overset{\circ}{\phi}(-\mathbf{x})$ is our theoretical camera prefilter that minimizes the reconstruction MSE for a given reconstruction display device with filter $H_{\text{dis}}(\mathbf{u}) = \Phi(\mathbf{u})$ it serves as the solution of (4.13). This solution is accompanied by the condition that $h_{\text{dis}}(\mathbf{x}) = \phi(\mathbf{x})$ should generate a Riesz basis for the space of continuous signals that can be produced by the display device $\mathbf{V}(\phi, \Lambda)$.

There are interesting discussions on the results of both theorems and I will discuss few of them.

- **Generalization of Unser's result [14]**: If $D = 1$, $\Lambda = \text{LAT}([X])$ then $\Lambda^* = \{k/X : k \in \mathbb{Z}\}$. The normalized frequency is also given by $U = u/X$. This reduces (4.21) to $H_1^*(U/X) = \frac{H_{\text{dis}}(U/X)}{\frac{1}{X}\sum_{k\in\mathbb{Z}} |H_{\text{dis}}((U+k)/X)|^2}$, which is exactly Unser's formula for 1-D or higher dimensional rectangular lattice [14].

- **Generalization for orthonormal bases**: Orthonormal bases are a special case of the generalized Riesz bases. If $\{\phi_{\mathbf{d}} : \mathbf{d} \in \Lambda\}$ are orthonormal then $\langle \phi_{\mathbf{d}}, \phi_{\mathbf{g}}\rangle = \delta[\mathbf{d} - \mathbf{g}]$. This inner product represents autocorrelation $\mathcal{R}_\phi$ with lags $(\mathbf{d} - \mathbf{g})$. This means that $\mathcal{R}_\phi[\mathbf{d}] = \delta[\mathbf{d}]$. Taking the Fourier transform on Λ and substituting in (4.20) then the reciprocal basis satisfies $\overset{\circ}{\Phi}(\mathbf{u}) = \Phi(\mathbf{u})$. This is true for any orthonormal basis (orthogonal bases can be normalized). If $\phi(\mathbf{x}) = \text{sinc}(\mathbf{x})$ then $\overset{\circ}{\phi}(\mathbf{x}) = \text{sinc}(\mathbf{x})$ which is the classical Shannon sampling theory. The same applies for a rect function. The rect function is of interest to us here because it models the characteristics of the TFT display devices. Hence,

for displaying images on a TFT display the best theoretical camera, in the MSE sense, is to have $h_1(\mathbf{x}) = \text{rect}(\mathbf{x})$ [3].

- **Relaxing the safeguard in [14]**: On top of the Riesz basis requirement for ϕ, a safeguard condition, called partitioning of the unity, was given in [14] as $\sum_{d\in\Lambda} \phi(\mathbf{x}+\mathbf{d}) = 1,\ \forall \mathbf{x} \in \mathbb{R}^D$. In fact this is a very strong condition that is satisfied by few basis functions like spline family. This led the results in [14, 69] to be pivoted around splines. The rationale behind this safeguard condition is the ability to represent signals as closely as possible from their samples. However, this safeguard condition *is not* satisfied by practical CRT monitors. Indeed, for a constant sampled input image the output displayed image is not a constant signal but rather is fluctuating. If we try a simple experiment to generate a constant full intensity image using a CRT, then we will obtain a fluctuating image intensity. Indeed, we show the plot of the L.H.S. of this condition using a model of a practical Gaussian beam response h_{dis} of a typical CRT in Fig. 4.7. The fluctuation is clear. Theorem 1 applies to general Riesz bases so we do not require this safeguard here. Hence, practically we require $\sum_{d\in\Lambda} \phi(\mathbf{x}+\mathbf{d}) \neq \mathbf{0}, \forall \mathbf{x} \in \mathbb{R}^D$. Without the requirement of Unser's safeguard condition we can now extend the minimum error sampling theory for arbitrary non-separable lattices for more general class of functions ϕ. An admissible choice for ϕ is now a Gaussian function simulating typical CRT monitors.

We assume separability of the Gaussian beam, hence the results are presented for 1-D. The optimal filter was designed using (4.21) and the results for designing the optimal pre-filter of the theoretical camera for some display devices are shown in Fig. 4.10. The selection of the optimal standard deviation is device dependent. I ran a simulation for the whole process for different standard deviation values for

[3] $\text{rect}(\mathbf{x}) = \text{rect}(-\mathbf{x})$, so $H_1^*(\mathbf{u}) = H_1(\mathbf{u})$

the Gaussian beam. I started by a super-high-resolution image and performed the following four steps:-

1. Pre-filter the image simulating f_c using a digitally designed approximation for $H_1(\mathbf{u})$, that is the corresponding solution for a selected standard deviation for the Gaussian display H_{dis}. I used a FIR filter designed using the windowing technique using the Blackman-Harris window.

2. Down-sample it to Λ.

3. Up-sample to the original lattice of the super-high-resolution again

4. Interpolate the up-sampled image by reconstruction with the display aperture.

5. Compute the MSE between the interpolated image and the original one.

I ran this procedure several times for different assumptions on the value of the standard deviation of the Gaussian function modelling the display aperture. I measured the MSE expressed as PSNR for each run, and the plot is shown in Fig. 4.8. The result for the maximum PSNR was found to occur when setting the standard deviation σ_{dis} of the Gaussian function to the value 0.36 of a pixel. The interpolated image obtained for running the experiment for this value of σ_{dis} also looked visually the best based on my personal preference as a human viewer in terms of edge sharpness, contour crispness, no ringing in smooth regions, and no ringing near edges. Also the optimal standard deviation obtained agrees with the technical characteristics obtained in [72]. The magnitude of the frequency response for the overall designed Anti-aliasing-Sampling-Reconstruction system $H_1(\mathbf{u})H_{\text{dis}}(\mathbf{u})$ for one case is shown in Fig. 4.9. This shows the response of the system that minimizes the error $\|\tilde{f}_1 - f_c\|^2$ in the MSE sense. A 2-D plot of the magnitude of the frequency response of a theoretical camera that is optimally designed for a CRT whose Gaussian aperture has standard deviation of 0.36 pixel is shown in Fig. 4.11(a). A plot in dB is shown in Fig. 4.11(b), of size 11

unit-cells of $\mathcal{P}_{\Lambda^*}$, indicates that the designed filter has a frequency response that is monotonically decreasing.

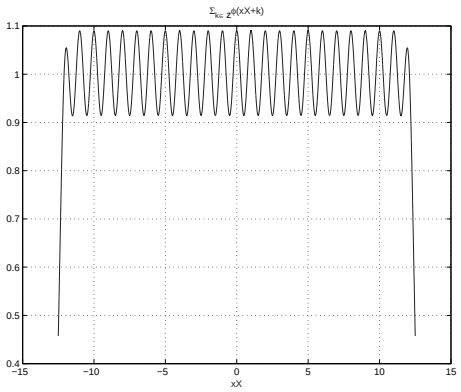

Fig. 4.7 Partitioning of unity is not satisfied by typical CRT display; Gaussian with $\sigma_{\text{dis}} = 0.53$ pixel.

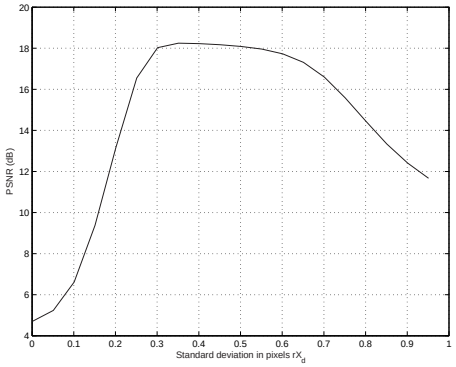

Fig. 4.8 PSNR in (dB) for reconstruction by displays with different Gaussian standard deviations.

4.7.3 More on CRT modelling

The model for CRT display device aperture is a Gaussian function [72]. The standard deviation for this Gaussian function model was found in [72] to be around 0.375 of a pixel. This value complies with the subjective visual tests that I have performed and still to be further investigated. However, there is a very important factor that is

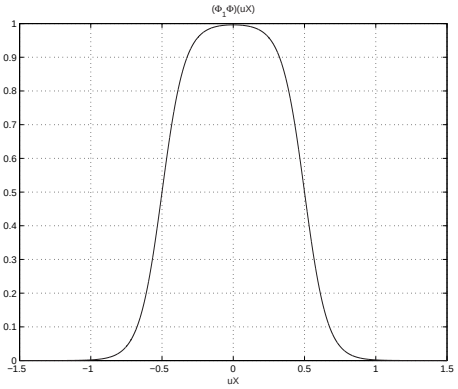

Fig. 4.9 Magnitude of the frequency response for the overall designed Anti-aliasing-Sampling-Reconstruction system for $\sigma_{\text{dis}} = 0.4$ pixel.

usually ignored in the literature for modelling the CRT display aperture. It is the effect of the digital-to-analog converter cascaded with the CRT aperture in the horizontal direction. The way a CRT operates is that it sweeps the horizontal scan lines in a continuous mode while it operates in a discrete fashion vertically from one scan line to the other. In the horizontal direction the digital data of the image $f_1[\mathbf{x}]$ are converted by a digital-to-analog device to form a continuous signal that is filtered by the Gaussian aperture of the CRT. Then in the horizontal direction the cascade effect to these two processes has to be considered. In a preliminary investigation, I assumed that the digital-to-analog device is the commonly-used sample-and-hold and I also tried others like linear and cubic ones. I convolved both the model of digital-to-analog converter with the Gaussian function modelling the CRT aperture. Then I performed a 1-D optimization search for the standard deviation of another Gaussian function that can closely model the cascade effect of these two processes. A 1-D plot of the magnitude of the frequency response of the display Gaussian aperture, cascaded process, and the approximating Gaussian are shown in Fig. 4.12. The digital-to-analog converter used is sample-and-hold and the Gaussian function used is of standard deviation 0.36 of a pixel. The resulting approximating Gaussian is found to have a standard deviation which is $4/3 \times 0.36$ of a pixel in this case. It is clear that the effect of this cascade

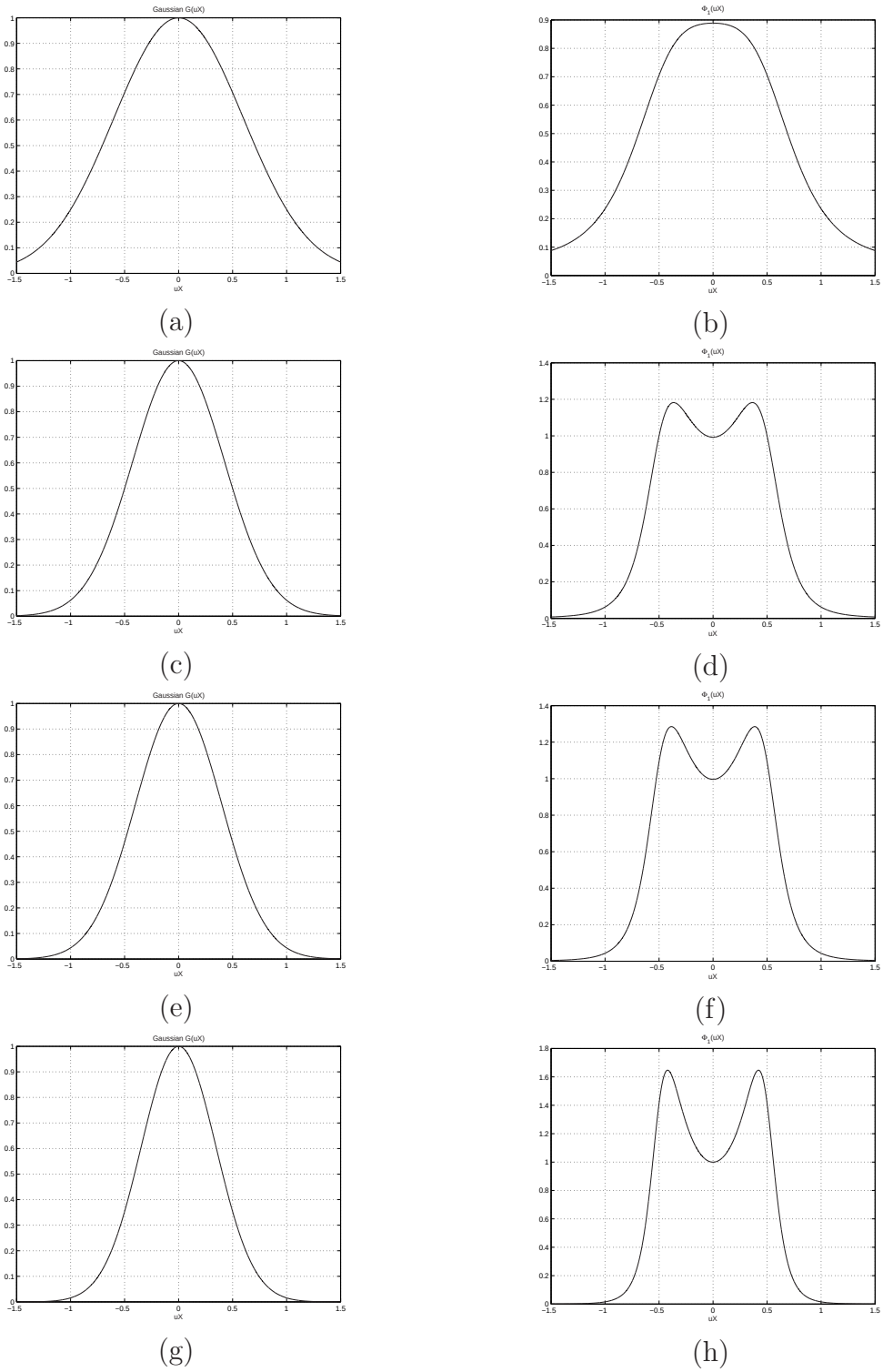

Fig. 4.10 Magnitude of the frequency responses for different display reconstruction Gaussian filters $H_{\text{dis}}(\mathbf{u})$ with different standard deviations σ_{dis} (a)0.24, (c) 0.47, (e) 0.53, (g) 0.71 of a pixel, and the magnitude of the frequency response of the corresponding optimal theoretical camera pre-filter (b, d, f, h) $H_1(\mathbf{u})$ for (a, c, e, g) respectively.

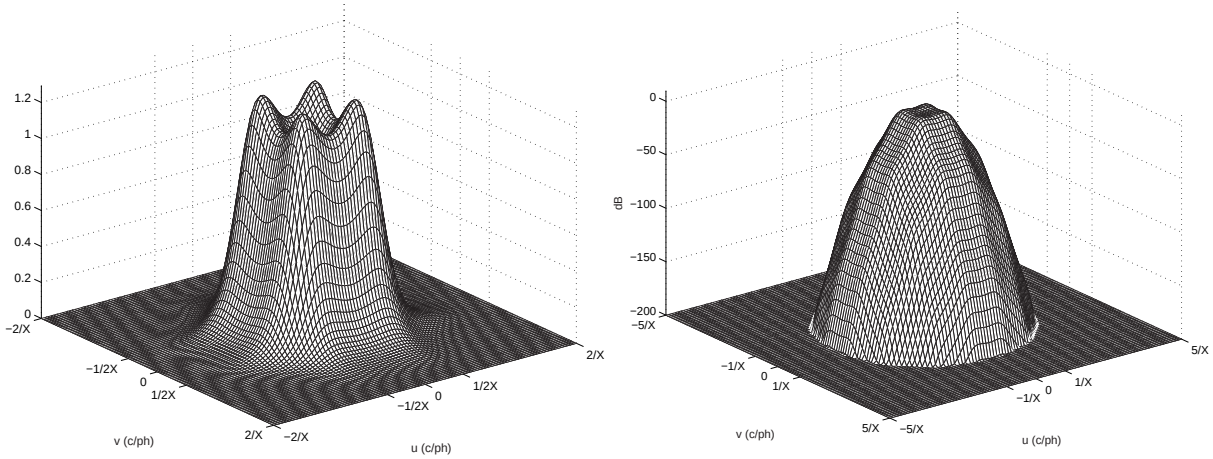

(a) (b)

Fig. 4.11 Magnitude of the frequency responses for the theoretical camera's filter $H_1(\mathbf{u})$ for a Gaussian model CRT with standard deviation 0.36 of a pixel (a) magnitude, (b) dB plot.

process is changing in the Gaussian aperture function in the horizontal direction. For this given example I obtained the optimal 2-D theoretical camera. The contour plot of the magnitude of its frequency response is shown in Fig. 4.13. It is clear that the profile of the frequency response is more stretched in the horizontal direction than that of the vertical direction. *This means that more resolution will be allowed in the horizontal direction and perhaps more aliasing.* The subjective quality of a down-sampled version of a very-high resolution image in effect to this correction in the modelling showed some enhancement. It should be noted that I compared the down-sampled image from the very-high resolution one obtained by the optimal theoretical camera and by using the best methods in Matlab and Photoshop. The subjective quality of the down-sampled image by the optimal theoretical camera was much better in many aspects. There was less aliasing and better perceived resolution in the image down-sampled by the optimal theoretical camera. These results need to be further investigated on a larger set of images.

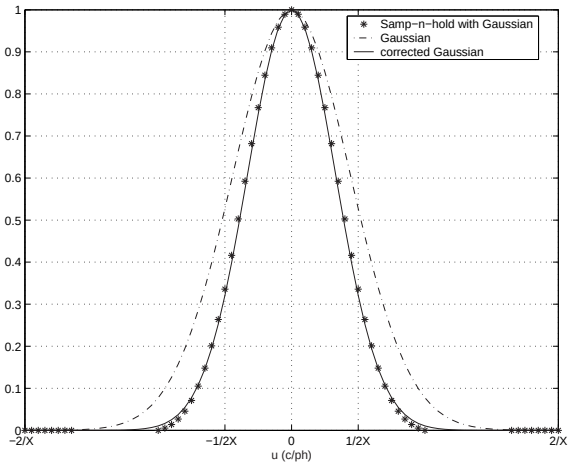

Fig. 4.12 Cascade effect of a sample-and-hold digital-to-analog converter and a Gaussian function with standard deviation $\sigma_{\text{dis}} = 0.36$ pixel.

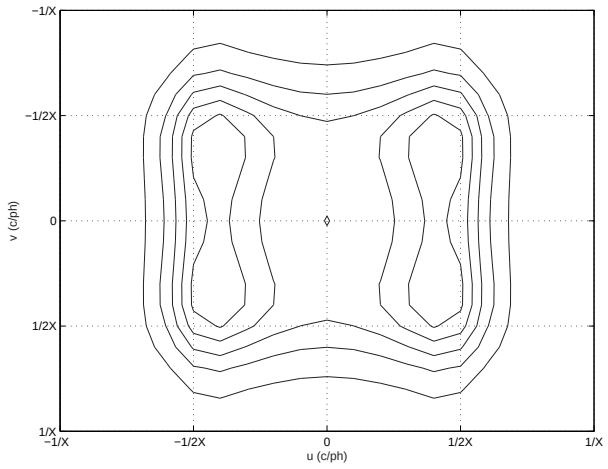

Fig. 4.13 Optimal theoretical camera for the cascade effect of a sample-and-hold digital-to-analog converter and a Gaussian function with standard deviation $\sigma_{\text{dis}} = 0.36$ pixel.

4.7.4 Case Study for hexagonal lattice.

In this section I will describe an experiment for designing the optimal aperture of the theoretical camera using (4.21) for images defined on a hexagonal lattice Λ with sampling matrix $V_\Lambda = \begin{pmatrix} 2X & X \\ 0 & X \end{pmatrix}$, where X is measured in units of picture height (ph). This sampling structure is the one used for sampling the green channel in typical color-filter-array CCD cameras. The associated display system $\phi(\mathbf{x})$ using a CRT is shown in Fig. 4.14. The display system consists of three stages: first, up-converting the sampling structure to a rectangular one with $V_\Xi = \mathrm{diag}(X, X)$ using a digital process. Second, converting the image in the horizontal direction to an analog signal using a 1-D digital-to-analog converter (DAC). This DAC is implemented in the graphics card and I assumed the sample-and-hold type. Third, displaying the 1-D analog signal on the CRT which is modelled by a convolution with a Gaussian function [72]. The selection of the standard deviation of the Gaussian function modelling the CRT was found based on our empirical experiments, as given in the previous section, to be 0.36 of the scan line spacing which also agrees with the technical characteristics obtained in [72]. Cascading these processes, which involves digital and analog components, results in a display aperture ϕ defined on the hexagonal structure Λ whose unit-sample response is plotted in Fig. 4.15. The corresponding 2-D plot of the magnitude of the frequency response of the designed optimal theoretical camera in the MSE sense is shown in Fig. 4.16.

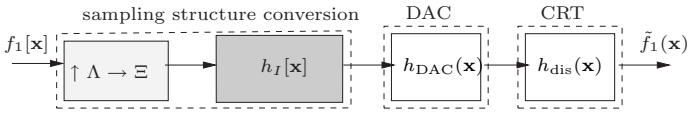

Fig. 4.14 Sample display system ϕ.

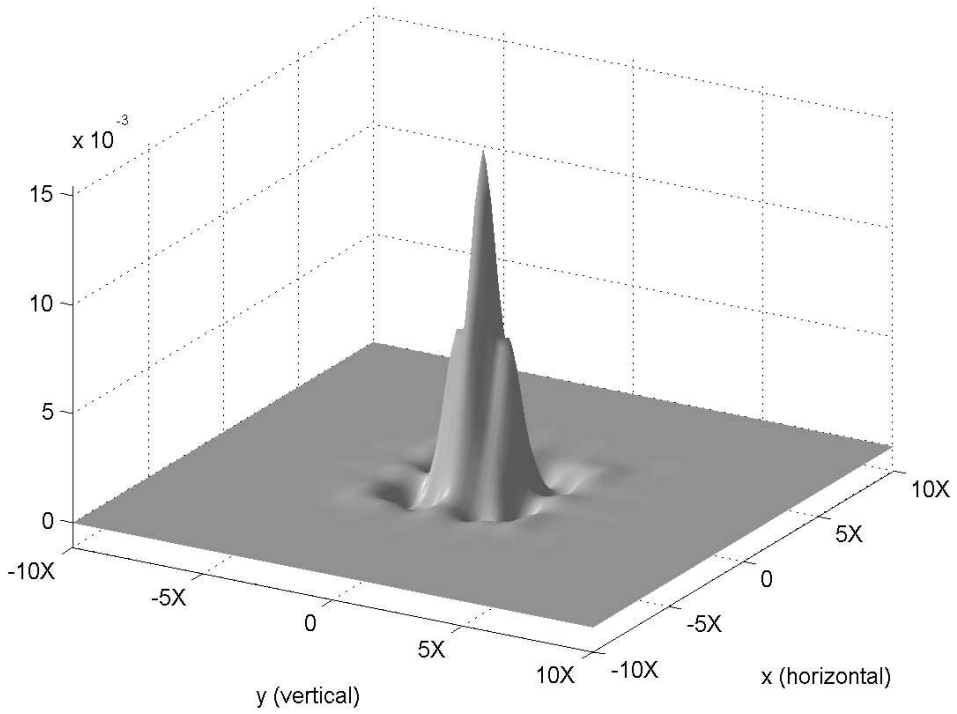

Fig. 4.15 Unit-sample response of the display system ϕ defined on hexagonal lattice.

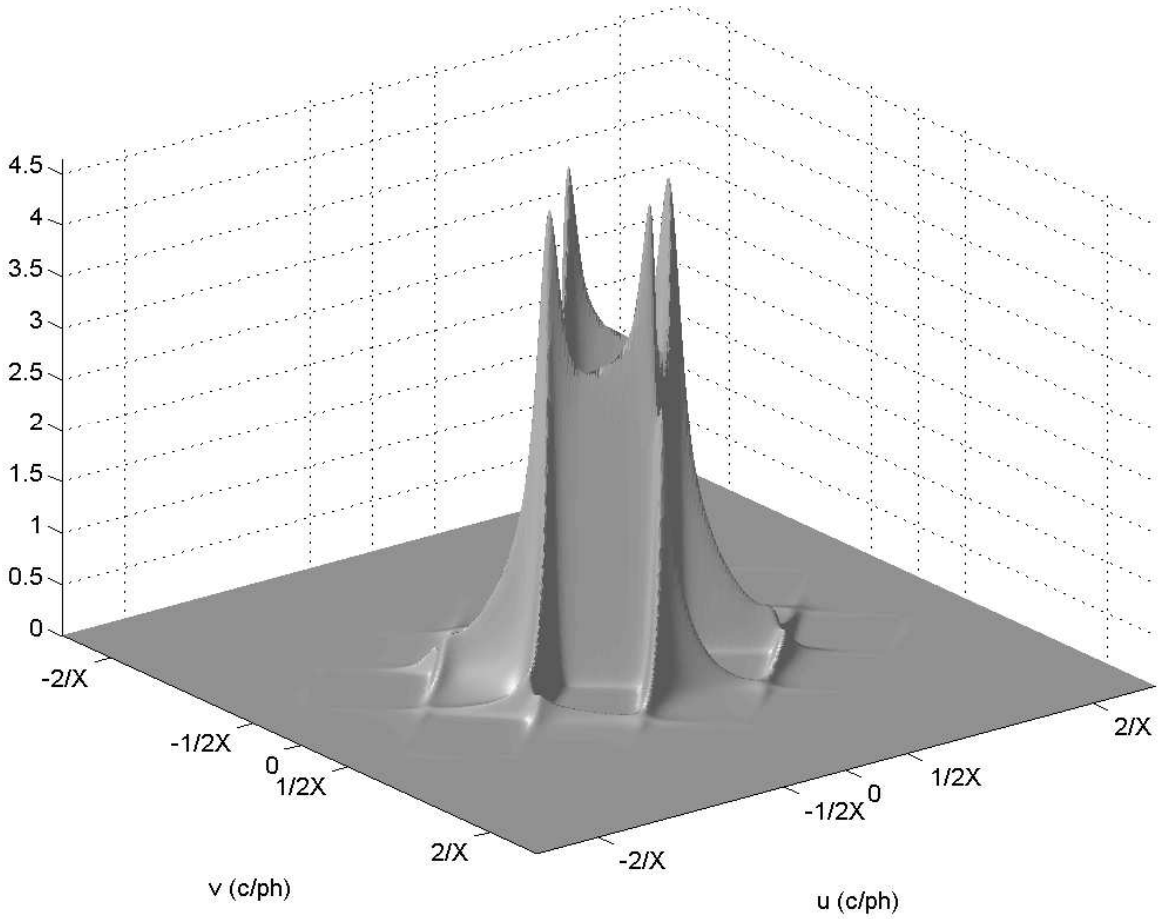

Fig. 4.16 Magnitude of the frequency response for the designed theoretical camera filter $H_1(\mathbf{u})$ for the display aperture of Fig. 4.15.

Modelling Filter	**Gauss-Gauss ($\downarrow 25$)**	**Rect-Rect ($\downarrow 25$)**	**Gauss-Rect ($\downarrow 25$)**	**Rect-Gauss ($\downarrow 25$)**
Resulting Optimal Modelling filter	See Fig. 4.5, 4.4(b)	Moving Average	see Fig. 4.3(a)	see Fig. 4.3(b), 4.4(a)
Comments	Optimized Gaussian-like: variance is critical	Phase correction is critical	Moving Average can work but not optimal	Neither Gaussian nor moving average
Simulated Optimization (Upper bound)	*61.96*	*63.22*	*53.48*	*58.35*
Our Model with PSD model: (4.11)	53.51	58.39	**52.20**	**55.15**
Moving Average	32.31	**63.22**	50.42	31.77
Maximally flat $\omega_{-3\text{dB}} = \frac{\pi}{4X}$	34.45	37.22	38.03	29.00
Maximally flat $\omega_{-3\text{dB}} = \frac{\pi}{8X}$	38.07	33.03	32.76	38.97
Optimized Gaussian[a]	**53.69**[b]	40.90[c]	40.43[d]	38.42 [e]

[a] Standard deviation of optimized Gaussian

[b] 2.1772 pixels

[c] 1.5635 pixels

[d] 1.497 pixels

[e] 1.874 pixels

Table 4.1 Performance of modelling filters for different scenarios: $\|e(\mathbf{x})\|_2$, MSE expressed as PSNR (dB)

Chapter 5

Results of Image Up-sampling

5.1 Results of regularized grey-scale image up-sampling

5.1.1 Perceptual uniformity versus linearity

The output light of CRTs are related to the input image by the power law [72]; images are raised to the power of a constant (γ) by the CRT. Hence, in order to display images correctly on CRTs they need to be compensated for this effect by preprocessing them. This compensation process is known as gamma correction. The gamma correction is performed automatically by physical cameras so that the digital image obtained is ready to be fed directly to the CRT. A commonly-used gamma correction for CRTs is the ITU-R Rec. 709 given by

$$f^{(\gamma)} = \begin{cases} 4.5f & f \leq 0.018; \\ 1.099f^{0.45} - 0.99 & 0.018 < f \leq 1, \end{cases}$$

which is plotted in Fig. 5.1. An advantage associated with the gamma correction process is that it produces images that are considered to be approximately perceptually uniform. The gamma correction process is a non-linear process and our observation

model designed in section 4.3 is applicable to LSI systems. This means that we need to perform our processing on the non-gamma-corrected image. Now we have two contradictory requirements:

1. We need the processing to be performed in the linear non-gamma-corrected grey scale space, to be compliant with the LSI nature of the designed observation model.

2. The processing should be done in an approximately perceptually-uniform space in accordance with the properties of the HVS.

In order to solve this problem I developed a methodology that performs all the processing in the linear grey-scale space while correcting for the perceptual uniformity using the gamma-correction. This is done by obtaining a correction weight that depends on the grey-scale value of the sample to be processed. Let us denote the gamma-corrected image by $f^{(\gamma)}$ and the distance between 2 grey-scale values as ΔE and ΔE_γ in the grey-scale and the gamma-corrected space respectively. The correction weight that maps the measure ΔE to its corresponding ΔE_γ, for small values of ΔE, can be obtained simply by computing $\frac{\partial f^{(\gamma)}}{\partial f}$. The plot for this correction weight computed on a grey-scale range $[0, 1]$ is shown in Fig. 5.2 and is given by

$$\frac{\partial f^{(\gamma)}}{\partial f} = \begin{cases} 4.5 & f \leq 0.018; \\ 0.49/f^{0.55} & 0.018 < f \leq 1. \end{cases}$$

The constant part of the weight is due to the corresponding linearity of the gamma-correction curve shown in Fig. 5.1. Hence we can write the corrected distance ΔE_{cor} as

$$\Delta E_{\text{cor}} = \frac{\partial f(^{\gamma})}{\partial f} \Delta E \tag{5.1}$$

These weights are computed for a reasonable step to quantize the grey-scale range $[0, 1]$ and then stored in a look-up table (LUT). This LUT is then used by any im-

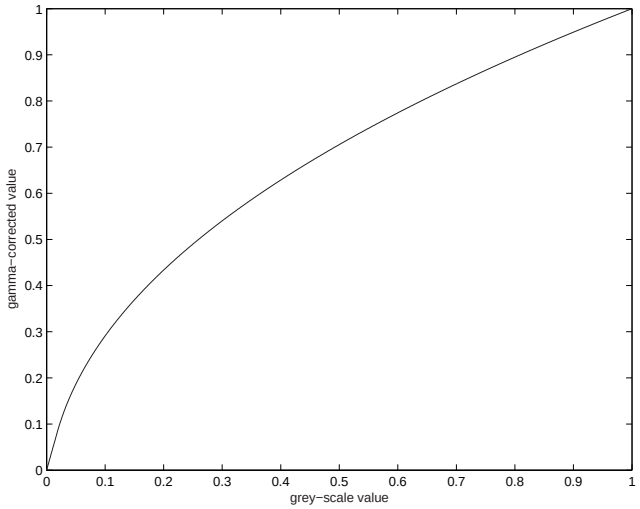

Fig. 5.1 ITU R Rec. 709 for gamma correction.

age processing algorithm to correct the sample updates during the processing. If we want to update $f[\mathbf{x}]$ by a value of ΔE then we quantize the value of $f[\mathbf{x}]$ using the same quantization step used in creating the LUT yielding a quantized value q. Then the value of q is used as an index entry in the LUT to access the correction weight needed. I used these correction weights in image up-sampling and it resulted in subtle enhancements near the edges. It should be noted that the procedure described here can be applied on the L channel used in the CIELAB color space which is more perceptually uniform than the gamma-corrected grey scale. The reason that I used the gamma-corrected is just for convenience because generally digital images are provided in the gamma-corrected space.

5.1.2 Implementation algorithms

The implementation of the grey-scale regularized image up-sampling is described by the following algorithms.

Algorithm 1. ***Image up-sampling*** *(f_2, λ, ΔT, ϵ)*

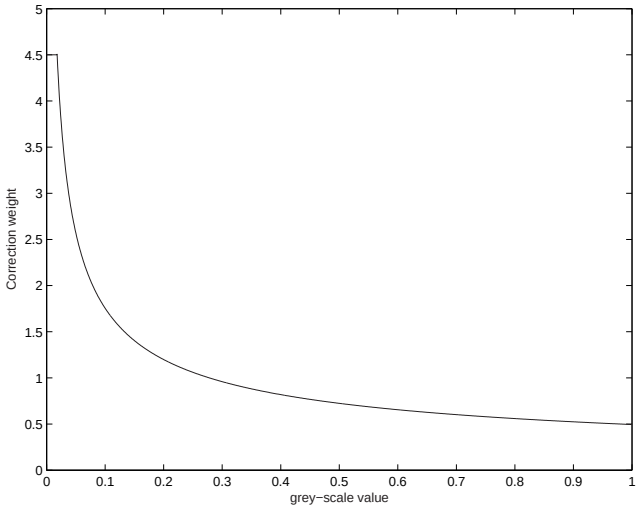

Fig. 5.2 Correction weights $\frac{\partial f^{(\gamma)}}{\partial f}$.

1. Undo the gamma-correction to f_2

2. Initialize $f_1^{(0)}$ by any arbitrary image

3. set $n = -1$

4. Do until termination criterion is satisfied

   (a) $n = n + 1$

   (b) Estimate the preconditioned mean curvature $\|\nabla_{\mathbf{x}} f_1^{(n)}\|\kappa^{(n)}$ by Algorithm 2 or 3

   (c) Compute the error $e^{(n)} = Hf_1^{(n)} - f_2$ as in Fig. 5.3

   (d) Compute the residue $r^{(n)} = H^{\mathrm{T}} e^{(n)}$ as shown in Fig. 5.3

   (e) $\zeta = \frac{\partial f_1^{(\gamma)}}{\partial f_1}|_{f_1}$

   (f) $f_1^{(n+1)} = f_1^{(n)} + \zeta \Delta T(\lambda \|\nabla_{\mathbf{x}} f_1^{(n)}\|\kappa^{(n)} - r^{(n)})$

(g) If MSE($f_1^{(n+1)}, f_1^{(n)}$) $< \epsilon$ then terminate

5. Store $f_1^{(n)}$

Algorithm 2. ***Preconditioned mean curvature*** *(f).*

1. Estimate the partial derivatives: $f_x, f_y, f_{xx}, f_{yy}, f_{xy}$ by (3.15)
2. Estimate $\|\nabla_{\mathbf{x}} f\| = \sqrt{f_x^2 + f_y^2}$
3. If $\|\nabla_{\mathbf{x}} f\| = 0$ then set $\|\nabla_{\mathbf{x}} f\|\kappa = 0$
4. Else using (3.6) set $\|\nabla_{\mathbf{x}} f\|\kappa = \frac{f_{xx} f_y^2 - 2 f_x f y f_{xy} + f_{yy} f_x^2}{f_x^2 + f_y^2}$
5. Return $\|\nabla_{\mathbf{x}} f\|\kappa$

The preconditioned mean curvature can also be computed analytically in terms of a specific prototype basis function ϕ. This function serves as the basis of an embedding space $\mathbf{V}(\phi, \Lambda)$. This gives the freedom to use many different prototype functions ϕ like splines or any other that combines the cascade effect of the display device used and an approximated LSI response of the HVS.

Algorithm 3. ***Advanced preconditioned mean curvature*** *(f, ϕ).*

1. Estimate the partial derivatives: $f_x, f_y, f_{xx}, f_{yy}, f_{xy}$ by (3.21)
2. Estimate $\|\nabla_{\mathbf{x}} f\| = \sqrt{f_x^2 + f_y^2}$
3. If $\|\nabla_{\mathbf{x}} f\| = 0$ then set $\|\nabla_{\mathbf{x}} f\|\kappa = 0$
4. Else using (3.6) set $\|\nabla_{\mathbf{x}} f\|\kappa = \frac{f_{xx} f_y^2 - 2 f_x f y f_{xy} + f_{yy} f_x^2}{f_x^2 + f_y^2}$
5. Return $\|\nabla_{\mathbf{x}} f\|\kappa$

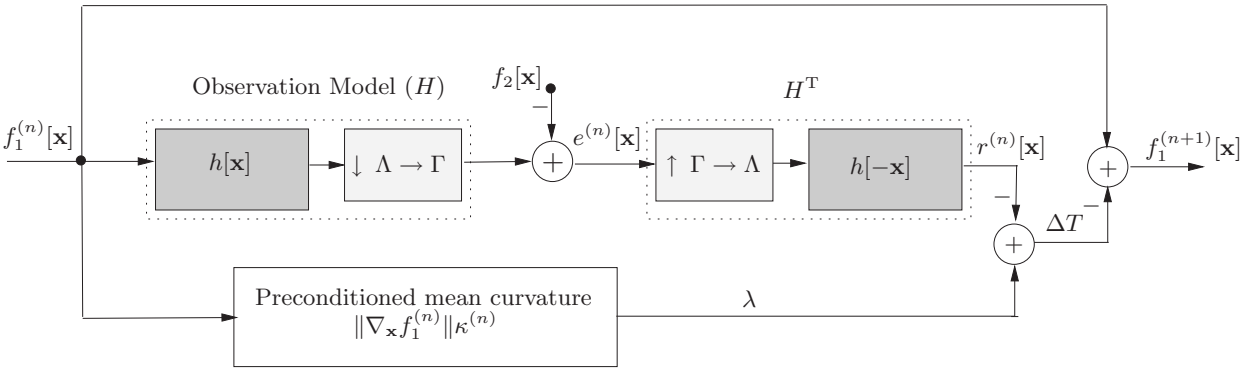

Fig. 5.3 An iteration in the up-sampling algorithm.

5.1.3 Experiments and results

In this section I will present some sample results for grey-scale image up-sampling using the proposed approach in (3.18). The solution scheme is implemented using an LSM with hybrid motions interacting simultaneously that are given by (3.19). The iterative numerical implementation of the LSM given by (3.20) is implemented using algorithms 1 and 2. The choice of the value of the regularization parameter here was based on the subjective quality of the results by running the experiments for several values of λ. The subjective quality of the results are measured informally by my personal preference as a human viewer in terms of edge sharpness, contour crispness, no ringing in smooth regions, and no ringing near edges. Different choices for the regularization parameter yield visually different results as shown later in the results. All these results for different λ produce visually acceptable results and are all visually better than other techniques like cubic B-spline. The results presented include various choices of λ. The sampling structures $\Lambda \supset \Gamma$ used here are both rectangular. The scenario used to design the observation model for up-sampling is assumed to be Gauss-

Rect($\downarrow 25$). Hence, the up-sampling is by a factor of 5 in each dimension. The iterative process is run until convergence. Normally convergence is achieved in a few hundred iterations. However, the convergence for sharp step edges and ramp edges is slower and may take up to a few thousand iterations. The LR image $f_2[\mathbf{x}]$ shown in Fig. 5.4(a) was used and the resulting HR image $f_1[\mathbf{x}]$ for $\lambda = 0.15$, $\Delta T = 1$, and 200 iterations is shown in Fig. 5.4(b). The result is also obtained using the Tikhonov regularization with $\lambda = 0.3$ and is shown in Fig. 5.4(c). The choice of the regularization parameter for the Tikhonov regularization method was based on my personal visual preference as described before. The results by the proposed method show enhancement over the Tikhonov regularization in many aspects. Regions that contain detailed objects like the camera are greatly enhanced and details are clear; these fine objects are treated as separate structures and did not undergo topological changes like merging. Edges with different orientations are sharp and continuous with no staircase effects; this is clear in the camera handle, the coat's edge, and the edge between hair and face. No ringing appears in smooth regions like the sky behind. Another example for up-sampling the tripod of the camera in the cameraman image by a factor of 25 using the proposed approach is shown in Fig. 5.5. The corresponding up-sampling using cubic B-spline is shown in Fig. 5.6. The proposed approach shows significant enhancement at the sharp edges as can be seen along all the rods of the tripod. An interesting enhancement can be seen at the white bottom part of the tripod main rod. In the spline up-sampling this part shows a roping effect. In the proposed approach this part is neatly up-sampled and its geometrical structure is preserved. I compared my results to Tikhonov regularization and cubic B-spline because both methods are currently used in various image processing applications. Tikhonov regularization is the most widely used regularization method used in most image processing applications because its numerical implementation is traceable and well studied. Cubic B-spline is receiving a lot of researchers attention in applying it in solving many image processing

(a)

(b)

(c)

Fig. 5.4 Up-sampling of (a) a portion of the cameraman image by a factor of 25 using (b) the proposed approach $\lambda = 0.15$ (c) Tikhonov regularization $\lambda = 0.3$.

problems, especially with its implementation for the minimum-error sampling. The false edges that are generated in Fig. 5.5 in the central part of the tripod is due to an early termination of the process (200 iterations) before this ramp edge was allowed to converge. Ramp edges usually need more iterations until they are represented by sufficient number of grey scale levels. Furthermore, over-regularization can be used to get rid of this effect by setting a slightly larger values of λ. I will show results for up-sampling the tripod of the camera in the cameraman image for different values of λ, $\Delta T = 1$, and after 5000 iterations. The results are shown in Fig. 5.7, 5.8, 5.9 for $\lambda = 0.06, 0.1, 0.4$ respectively. *I recommend using* $\lambda \in [0.02, 0.2]$ *as a tuning parameter left to the user preference.* Based on the experience gained from applying this approach to various images, values of λ closer to 0.1 usually provides the best results based on my visual preference. Another example is up-sampling a portion of the Barbara image shown in Fig. 5.10(a) by a factor of 5 in each dimension using the proposed approach (Fig. 5.10(b)) and cubic B-spline (Fig. 5.10(c)). The parameters used in the result in Fig. 5.10(b) are $\lambda = 0.15$, $\Delta = 1$, and 1000 iterations for a Gauss-Gauss ($\downarrow 25$) observation model scenario. It is clear from the figures that the result by the proposed approach is superior to the result by the cubic B-spline. The stripes are sharp without any ringing as in the cubic B-spline result in Fig. 5.10(c). The hand on the left side of the image is smooth in Fig. 5.10(b) while it suffers from ringing in Fig. 5.10(c).

The main drawback of the proposed approach as being an iterative approach is the computation time. Specifically, the main burden in the computation is the estimation of the mean curvature κ. Its computation requires the following:

- Estimation of 5 partial derivatives which are implemented by convolutions with different kernel sizes.
- Computation of the squares of both f_x and f_y.
- Performing an additional 4 multiplications, 3 additions, and 1 division.

Fig. 5.5 Up-sampling of the tripod of the cameraman image by a factor of 25 using the proposed approach for 300 iterations and with $\lambda = 0.15$.

Fig. 5.6 Up-sampling of the tripod of the cameraman image by a factor of 25 using cubic B-spline.

Fig. 5.7 Up-sampling of the tripod of the cameraman image by a factor of 25 using the proposed approach for $\lambda = 0.06$.

Fig. 5.8 Up-sampling of the tripod of the cameraman image by a factor of 25 using the proposed approach for $\lambda = 0.1$.

Fig. 5.9 Up-sampling of the tripod of the cameraman image by a factor of 25 using the proposed approach for $\lambda = 0.4$.

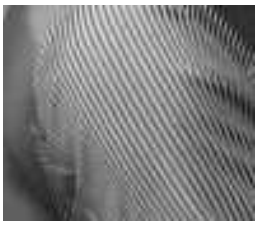

(a)

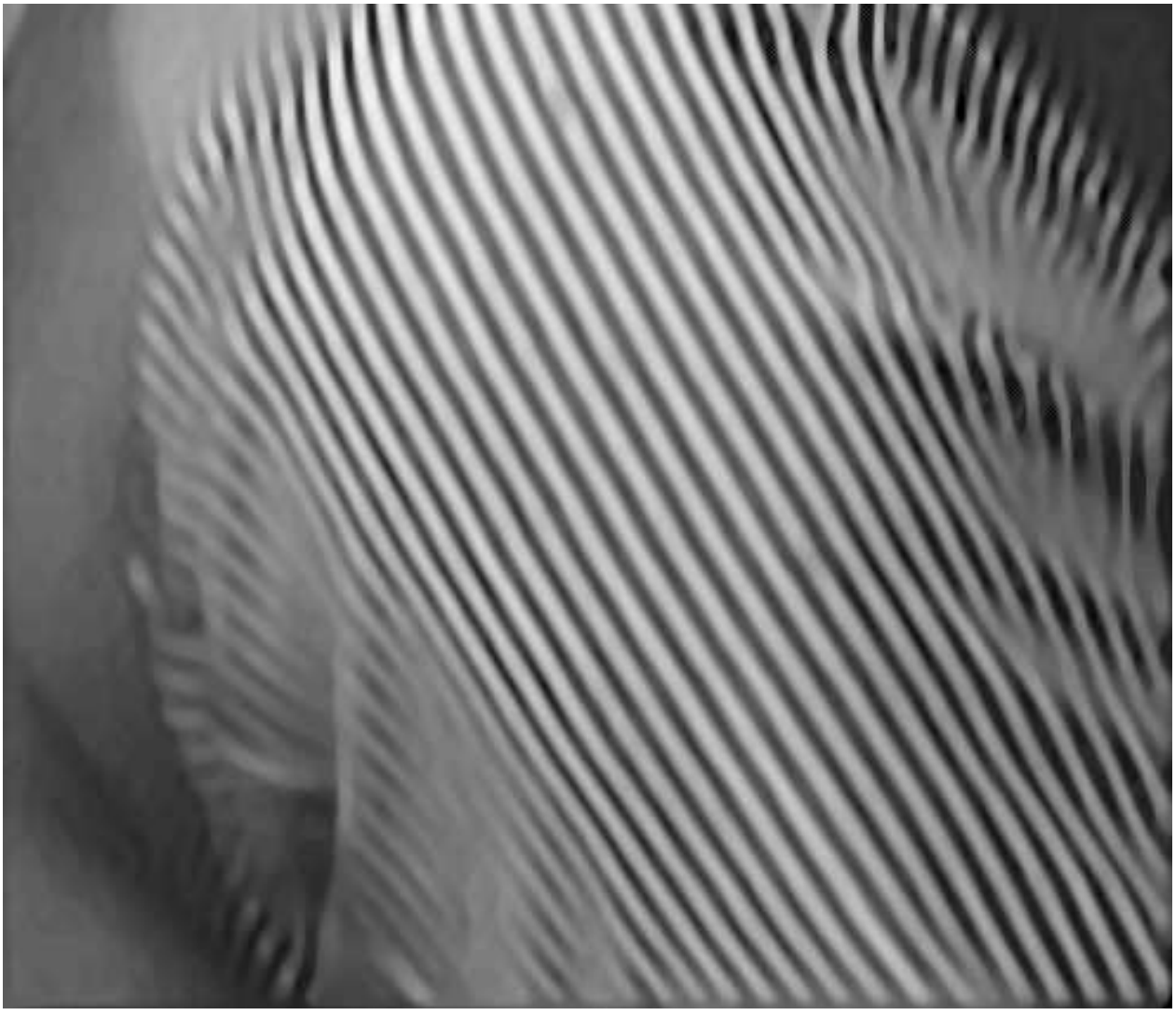

(b)

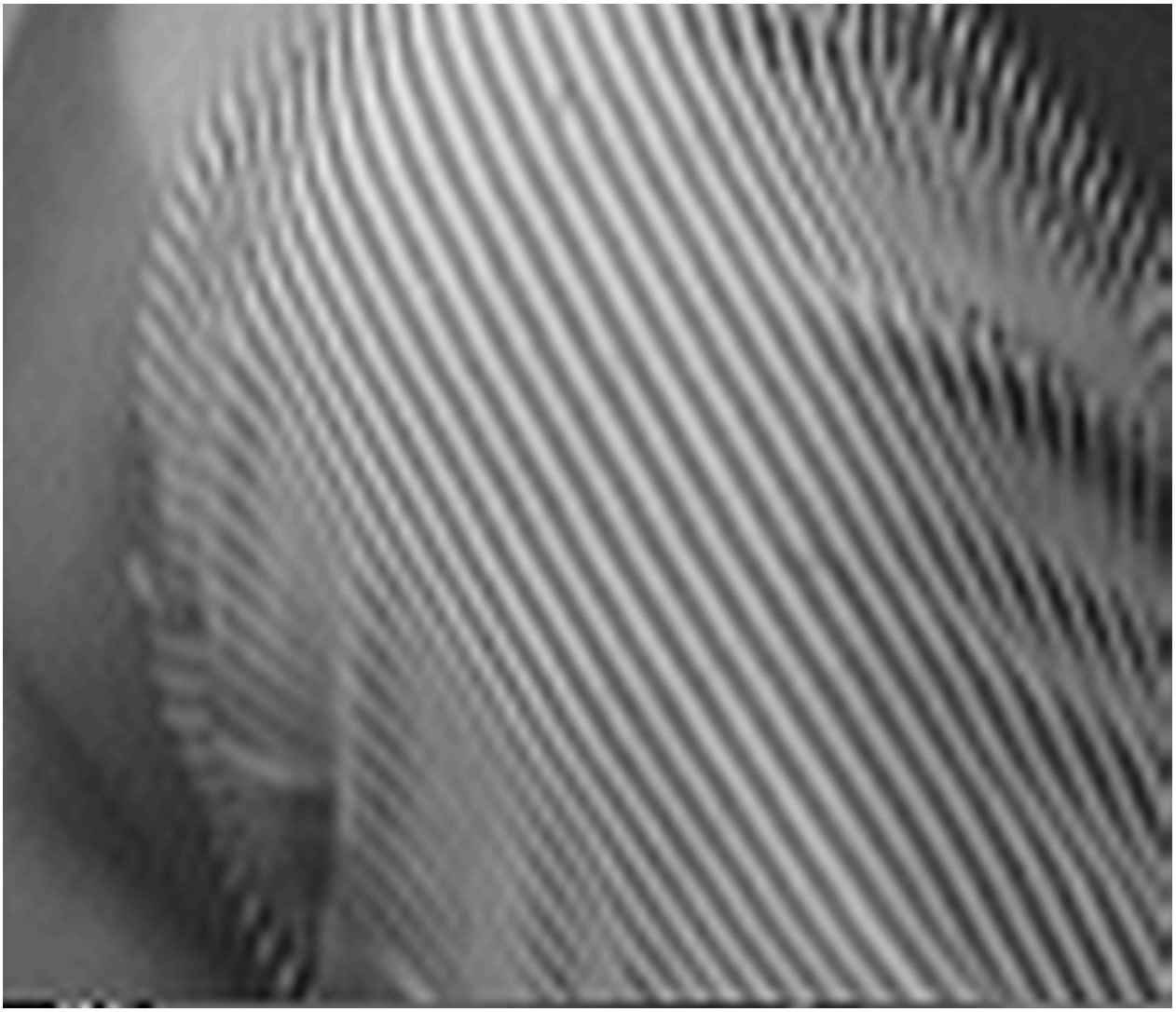

(c)

Fig. 5.10 Up-sampling of (a) a portion of Barbara image by a factor of 25 using (b) the proposed approach for 300 iterations and with $\lambda = 0.15$ and (c) cubic B-spline .

The details of the computations of κ for a single pixel of the HR image in each iteration is given in Table 5.1. This is in addition to the need for many memory accesses to retrieve the intermediate results. However, this drawback can be mitigated by hardware implementation since the computation is localized in a small neighborhood around the target pixel. Another way to enhance the speed is by mathematical inspection of the problem and coming with a better optimization technique. Fortunately, there is a recent work by Combettes [73, 74] to solve these kinds of optimization problems numerically in the dual space. He implemented this dual space numerical optimization for quadratic-type objective functions for signal restoration [73]. This seems to be a promising mathematical result to overcome the current computation load. Implementation of this new optimization method is still needed for the total-variation norm like the one we are using in this thesis.

Item	**Multiplications**	**Additions**
f_x	2	2
f_y	2	2
f_{xx}	3	3
f_{yy}	3	3
f_{xx}	3	3
f_{xy}	4	4
f_x^2	1	0
f_y^2	1	0
$f_{xx}f_y^2$	1	0
$f_{yy}f_x^2$	1	0
$f_x f_y f_{xy}$	2	0
Numerator sum	0	3
Denominator sum	0	1
Division	1	0
Total	**23**	**21**

Table 5.1 Computational complexity of estimating the mean curvature.

5.2 Extension to color image magnification

After the success of the proposed approach in solving the regularized grey-scale image up-sampling, the natural step is to extend the approach to color images. Many researchers in the field have advised exploiting the correlation among the color channels during the processing. This advice is based on results from biological vision system studies that humans synthesize information from all channels to convey the visible information [75]. Since we are concerned with producing high-quality HR images that will be viewed by the human vision system (HVS), then the processing should be optimized for this HVS. There are many color spaces to represent the color information. These spaces are optimized for a variety of purposes or physical devices as follows:

- Acquisition devices such as camera, scanner, etc.
- Display device color spaces such as ITU-R Rec. 709 for the red, green, and blue phosphors used in CRTs and the ITU-R Rec. 709 gamma-corrected RGB used for CRT monitors;
- Broadcasting, which requires compression due to the limited transmission media bandwidth. The luma-color-difference (ITU-R Rec. 601) color space is commonly used for this purpose;
- Finally, HVS oriented color spaces like the CIE 1976 LUV and CIE 1976 LAB color spaces.

One can always convert from one color space to the other. A collection of these transformation formulas from one color space to the other can be found in [76]. One should ask an important question before performing any processing involving color images: what is the suitable color space? The answer depends on what one wants to do. In our case we are interested in a color space that is oriented towards the HVS. One of the most successful and simple to compute is the CIELAB [77]. The main

advantage of this space is that it is a perceptually uniform space. This means that the Euclidean distance between the representations of any two color stimuli in the LAB space corresponds to a uniform measure of the ability of the human sensation to distinguish these two colors. Indeed this is crucial for the up-sampling problem because we seek perceptual uniformity of color transitions in the newly added samples by the up-sampling process. However, there are two associated difficulties in using the LAB color space in our case:

1. The LAB color space is not a linear space and the mapping from the camera RGB space or the display ITU-R Rec. 709 RGB space to LAB space requires a non-linear transformation. This is problematic to be involved as a stage in the observation model which is linear by nature.

2. In some applications like the demosaicking of a color filter array, the three RGB values are not available at each sample location and hence we cannot perform the transformation to LAB space.

We would like to perform the up-sampling process in the LAB space but we are faced with the two above-mentioned difficulties. Fortunately, I solved this problem as given in the next section

5.2.1 Implicit processing in perceptually-uniform color spaces

First we need to understand the idea of perceptual-uniformity and why the RGB or the gamma-corrected RGB spaces would not offer a good solution when we are interested in presenting the results to a HVS. I produced both the CRT gamma-corrected RGB gamut[1] and the RGB gamut in the LAB space. When a perceptually uniform space is mapped to the LAB space, its plot should resemble a cubic structure with equidistant planes along the three axes L, a, and b. This means that the distance between two

[1] Gamut: the set of colors that can be produced by a device [76].

colors in this perceptually uniform space can be measured by the Euclidean distance in the LAB space. The farther the gamut or the plot of a color space in the LAB space from the cubic structure with equidistant planes, the farther it is from being perceptually uniform. The gamuts of the gamma-corrected RGB and the RGB color spaces are plotted in Fig. 5.11 and Fig. 5.12 respectively. I generated these plots by designing and running algorithm 4. These plots were generated for a step size of 0.2 between the planes and 256 points to plot each line. Each line is plotted by fixing 2 values of the RGB representation while changing the third color along the full range of values. In the plot, the color of each line corresponds to the single color value that is changing. In other words, a green line represents a plot for fixed values of both R and B while G is changing.

Algorithm 4. ***Gamut generation*** *($p_{\texttt{step}}, l_{\texttt{step}}$).*

1. `For R = 0:`$p_{\texttt{step}}$`:  1`
   - `For G = 0:`$p_{\texttt{step}}$`:  1`
     - `For B = 0:`$l_{\texttt{step}}$`:  1`
       - `plot gamut point(R,G,B)`
2. `For B = 0:`$p_{\texttt{step}}$`:  1`
   - `For R = 0:`$p_{\texttt{step}}$`:  1`
     - `For G = 0:`$l_{\texttt{step}}$`:  1`
       - `plot gamut point(R,G,B)`
3. `For G = 0:`$p_{\texttt{step}}$`:  1`
   - `For B = 0:`$p_{\texttt{step}}$`:  1`
     - `For R = 0:`$l_{\texttt{step}}$`:  1`

* `plot gamut point(R,G,B)`

Algorithm 5. ***plot gamut point*** *(R, G, B)*

1. `Convert the (R,G,B) point to (L,a,b) point`
2. `Plot the point whose coordinates are (L,a,b)`

It is clear that the RGB color space is far from being perceptually uniform. The gamma-corrected RGB is better than RGB in terms of perceptual uniformity and is sometimes claimed to be approximately perceptually uniform. Ironically, this is far from the truth; the gamma-corrected RGB can only locally be considered as perceptually uniform because of the local orthogonality of its representation in LAB space. If we inspect the plotted planes orthogonal to any of the LAB axes, we find that they are not equidistant although they were generated from equidistant values in the CRT gamut!

To keep our designed observation model intact and to be able to handle problems like demosaicking of the color-filter-array, then we ought perform the analysis and the explicit processing in RGB or YCbCr color space. In order to perform all the processing in LAB space I developed the following analysis and results as follows

1. Analytically calculate the Jacobian of the transformation from RGB to LAB space as
$$J = \begin{pmatrix} \frac{\partial L}{\partial R} & \frac{\partial a}{\partial R} & \frac{\partial b}{\partial R} \\ \frac{\partial L}{\partial G} & \frac{\partial a}{\partial G} & \frac{\partial b}{\partial G} \\ \frac{\partial L}{\partial B} & \frac{\partial a}{\partial B} & \frac{\partial b}{\partial B} \end{pmatrix}$$
2. Calculate the rate of change of the Euclidean distance between two colors in the LAB space with respect to each of R, G, and B. The Euclidean distance in LAB space between two colors is denoted by ΔE^*_{ab}. Then this above rate of change

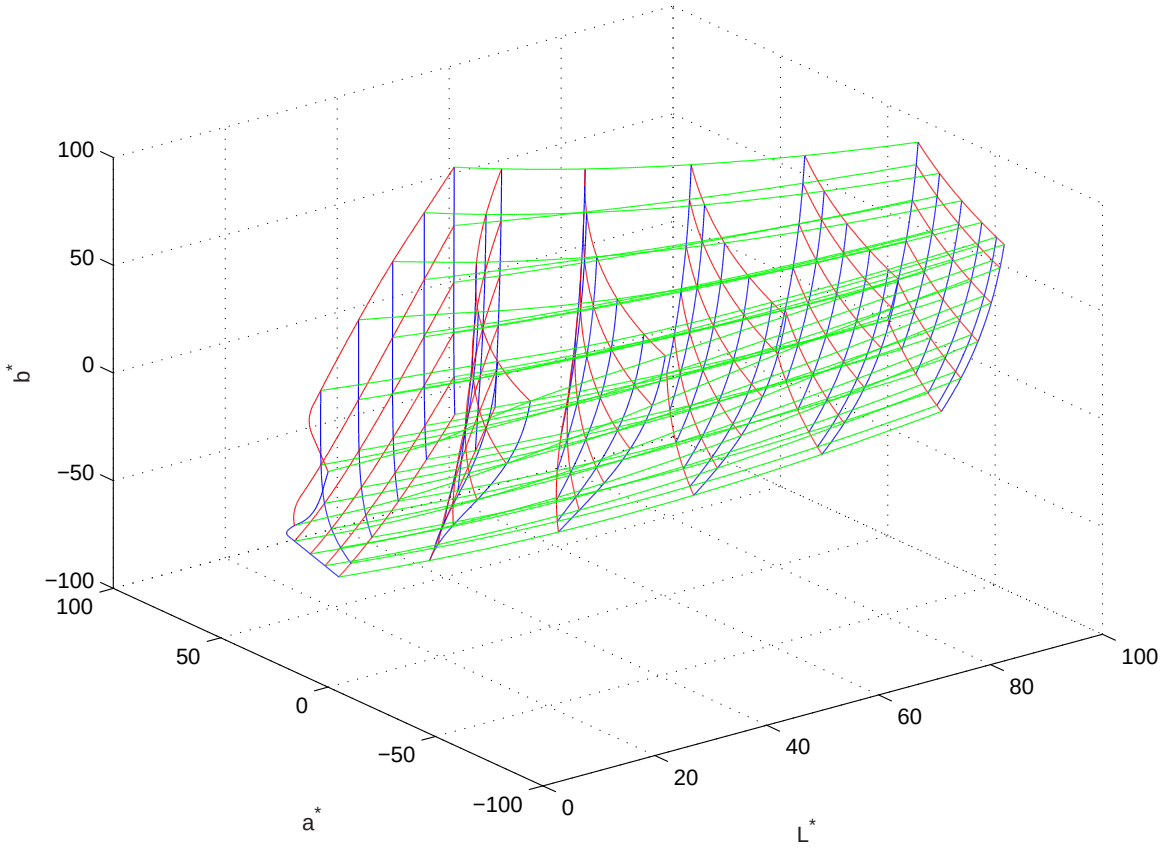

Fig. 5.11 CRT gamut: perceptual non-uniformity of Gamma-corrected RGB (ITU-R Rec. 709) plotted in CIELAB color space.

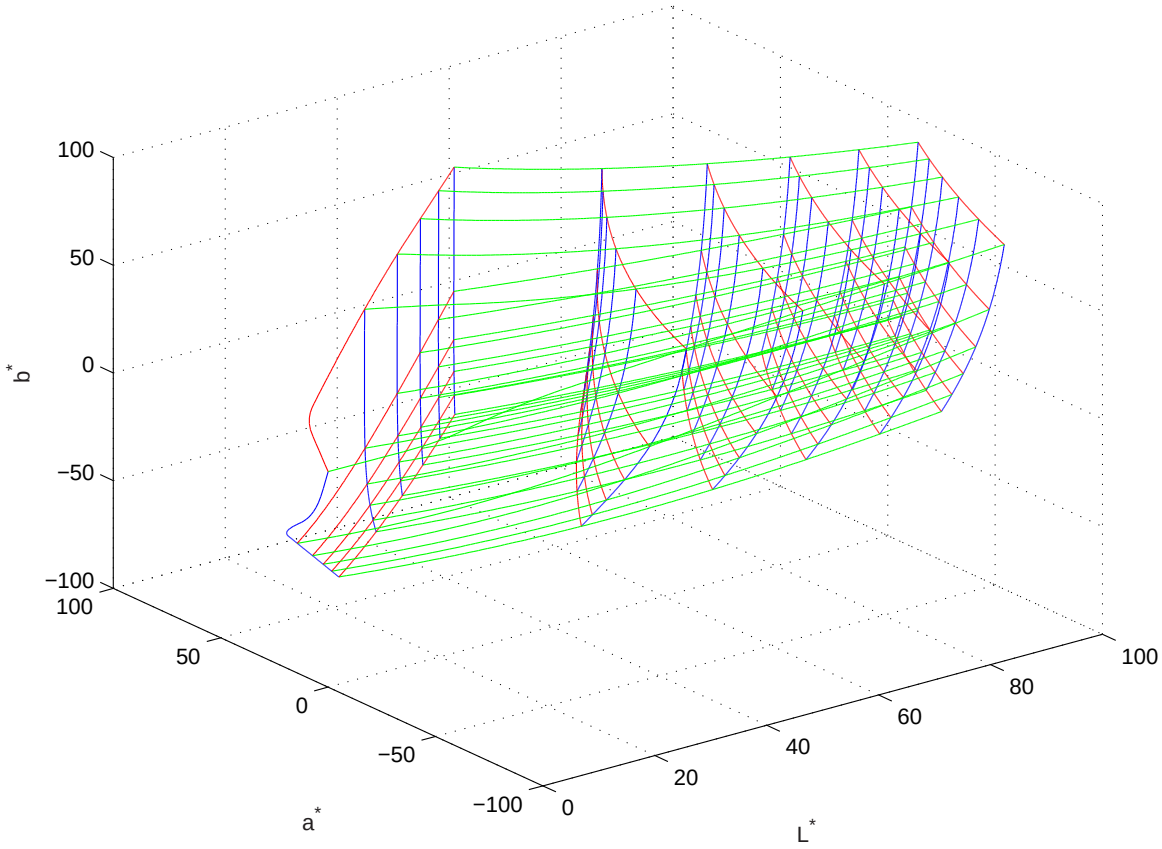

Fig. 5.12 Perceptual non-uniformity of RGB (ITU-R Rec. 709) plotted in CIELAB color space.

is evaluated as:

$$\begin{pmatrix} \frac{\partial \Delta E^*_{\mathrm{ab}}}{\partial R} \\ \frac{\partial \Delta E^*_{\mathrm{ab}}}{\partial G} \\ \frac{\partial \Delta E^*_{\mathrm{ab}}}{\partial B} \end{pmatrix} = \begin{pmatrix} \sqrt{(\frac{\partial L}{\partial R})^2 + (\frac{\partial a}{\partial R})^2 + (\frac{\partial b}{\partial R})^2} \\ \sqrt{(\frac{\partial L}{\partial G})^2 + (\frac{\partial a}{\partial G})^2 + (\frac{\partial b}{\partial G})^2} \\ \sqrt{(\frac{\partial L}{\partial B})^2 + (\frac{\partial a}{\partial B})^2 + (\frac{\partial b}{\partial B})^2} \end{pmatrix}$$

This is admissible because of the local orthogonality of the RGB and the Gamma-corrected RGB in the LAB space.

3. Compute the quantities derived in step 2 for a reasonable quantization step for both the RGB and gamma-corrected RGB space. I used a step of 8 intensity levels so that we have $256/8 = 32$ values for each color. This will yield a total of $32^3 = 32768$ values.

4. Normalize the obtained values by dividing them by the ratio between the maximum distance that can be measured CIELAB space and the maximum distance that can be measured in the corresponding RGB or gamma-corrected RGB space. This means dividing by a value of 300. This is just for convenience to obtain reasonable values of the magnitudes for the rate of change.

5. Store the numerical values of the derivatives obtained in step 3 in a look-up table (LUT) for fast use by any color image processing technique.

The plots for $\frac{\partial \Delta E^*_{\mathrm{ab}}}{\partial R}$, $\frac{\partial \Delta E^*_{\mathrm{ab}}}{\partial G}$, $\frac{\partial \Delta E^*_{\mathrm{ab}}}{\partial B}$ are shown in Fig. 5.13. Similarly, the plots for performing the same process for gamma-corrected RGB are shown in Fig. 5.14. It is obvious from the plots that the values of the Euclidean distances are not constant and depend on the values of the color represented by its three values in RGB or gamma-corrected RGB space. The spike that appears in all the plots near the blue color ($G = R \approx 0$) is due to a limitation in the CIELAB space in the vicinity of the CRT blue primary [76]. There are other CIE formulas to correct for this defect; an example is the CIE-DE 2000. However, its computational complexity is very high and it needs

external tuning parameters which does not justify this small correction that might not be critical in our case here.

We can use the obtained weights by this procedure to correct the computations during our up-sampling algorithm. This is done by weighting the iterative changes to the RGB values by these obtained weights. Without any corrections for perceptual uniformity a distance between two colors in the RGB or the Gamma-corrected RGB space is measured by $\sqrt{(\Delta R)^2 + (\Delta G)^2 + (\Delta B)^2}$. This measure does not reflect any of the properties of the HVS. Thus I propose measuring the corrected distance between two colors in the RGB or the gamma-corrected RGB by the following formula

$$\boxed{\Delta E_{\mathrm{RGB}} = \sqrt{\Big(\frac{\partial \Delta E^*_{\mathrm{ab}}}{\partial R}\Delta R\Big)^2 + \Big(\frac{\partial \Delta E^*_{\mathrm{ab}}}{\partial G}\Delta G\Big)^2 + \Big(\frac{\partial \Delta E^*_{\mathrm{ab}}}{\partial B}\Delta B\Big)^2}.} \tag{5.2}$$

5.2.2 Background on vectorial total variation norm for color images

The transitions in the color channels are correlated because they reflect the transition from one object to another or texture in the real scene. Hence, there is a unique definition for an edge or contour for all three color channels. They should all reflect a unique identification of the spatial location of the edge but might possibly have different magnitude and sign of change across the color channels. Then the important factor in designing a vectorial total variation regularizer is to have a unified definition for the measure of the transitions for all color channels. In this case the gradient of the HR image $\tilde{\mathbf{f}}_1$ represented in RGB color space is actually a Jacobian matrix given by

$$D\tilde{\mathbf{f}}_1 = \begin{pmatrix} \frac{\partial R}{\partial x} & \frac{\partial G}{\partial x} & \frac{\partial B}{\partial x} \\ \frac{\partial R}{\partial y} & \frac{\partial G}{\partial y} & \frac{\partial B}{\partial y} \end{pmatrix}.$$

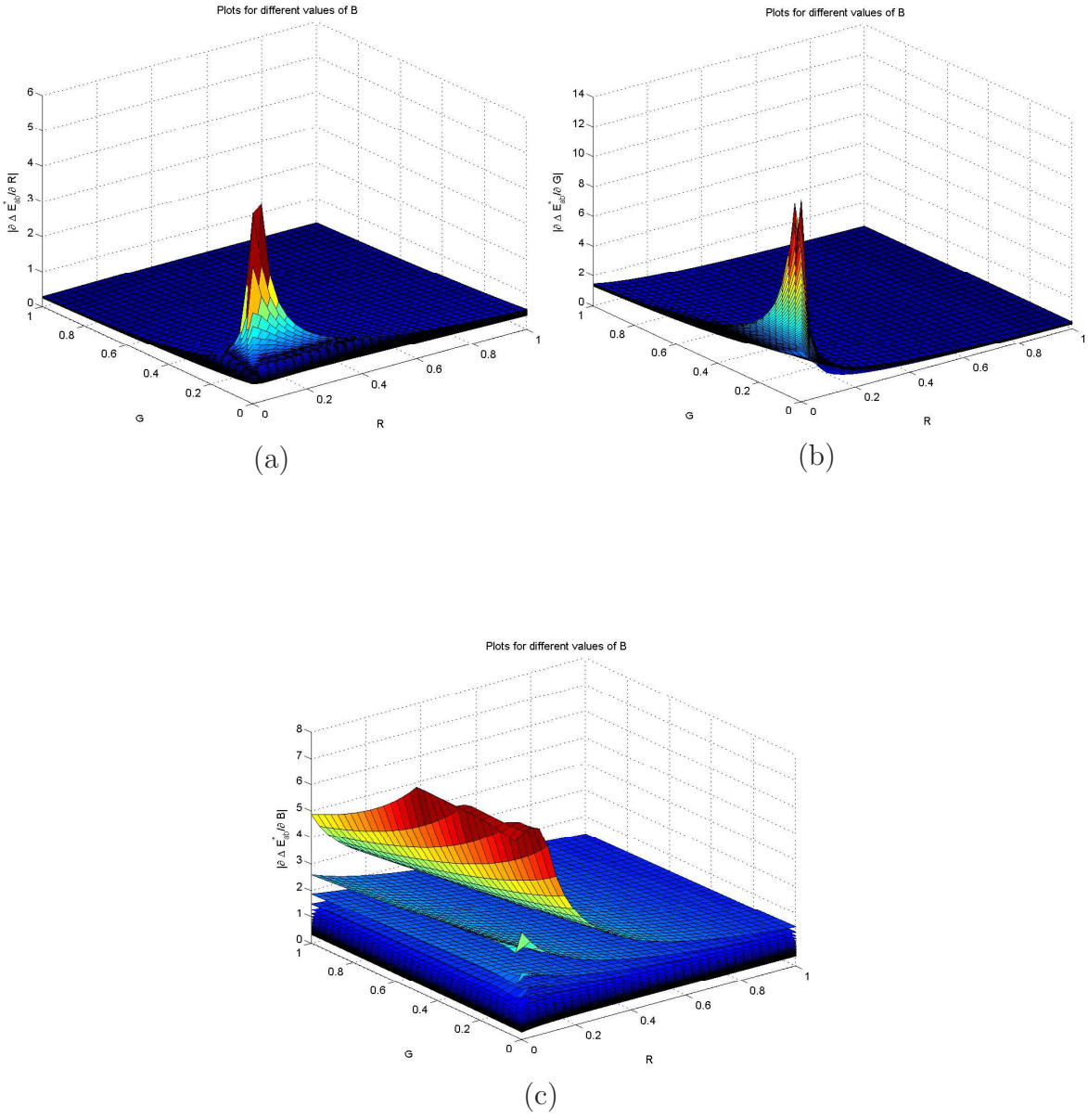

Fig. 5.13 Rate of change of perceptual-uniformity per change in (a) Red, (b) Green, and (c) Blue measured in CIELAB distance.

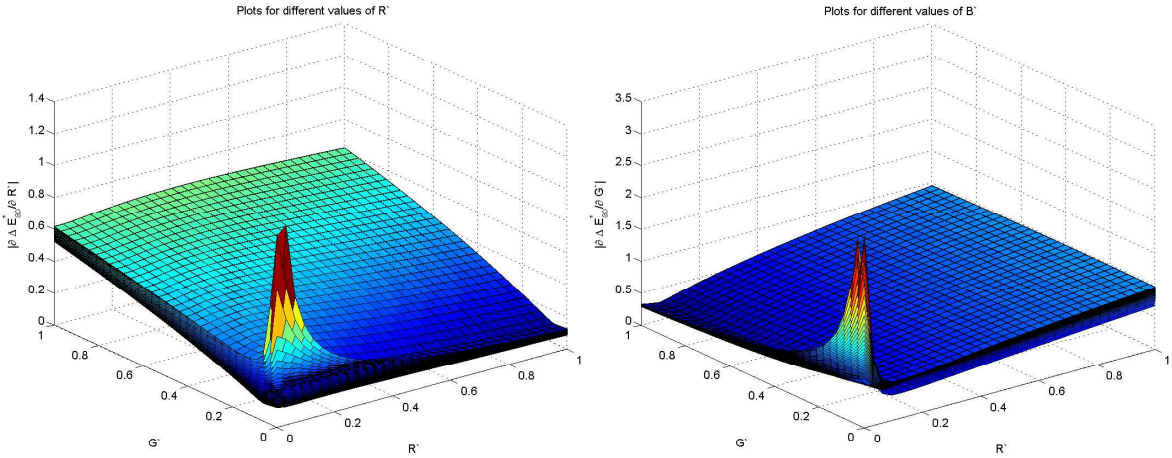

(a) (b)

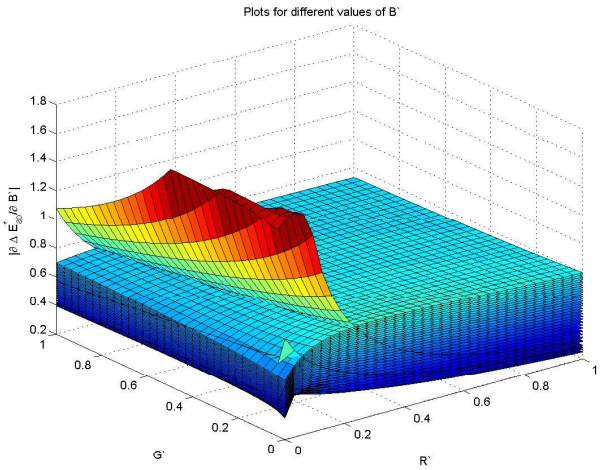

(c)

Fig. 5.14 Rate of change of perceptual-uniformity per Gamma-corrected (a) Red, (b) Green, and (c) Blue measured in CIELAB distance.

The idea of vector edges and contours for color images was analyzed in the framework of differential geometry by Di Zenzo [78]. He described the first fundamental form for a RGB color image to be given in what is sometimes called the $\mathcal{G}$ matrix as follows:

$$\mathcal{G} = \begin{pmatrix} R_{xx}^2 + G_{xx}^2 + B_{xx}^2 & R_{xy} + G_{xy} + B_{xy} \\ R_{xy} + G_{xy} + B_{xy} & R_{yy}^2 + G_{yy}^2 + B_{yy}^2 \end{pmatrix}, \tag{5.3}$$

where R, G, and B denotes the color channels and the subscript denotes the directional spatial derivative. The matrix $\mathcal{G}$ has two eigenvalues λ_+ and λ_- which correspond to the magnitude (strength) of the transition along two orthogonal directions. It should be noted that for grey-scale images λ_- is zero and thus we have only one direction for the transition (gradient) that is in the plane of the image itself. Sapiro [79] proposed that the color image transitions should account for both eigenvalues and proposed a variational scheme $\mathfrak{L}(\mathbf{f}_1(\mathbf{x})) = \mathfrak{F}(\lambda_+, \lambda_-)$. However, he did not specify a particular choice for $\mathfrak{F}$. Some choices have been proposed in the literature which are surveyed in a recent paper [80]. Perhaps the most common choice in the literature is setting $\mathfrak{F}(\lambda_+, \lambda_-) = \sqrt{\lambda_+^2 + \lambda_-^2}$ which is sometimes denoted by $\mathcal{N}_+$. Interestingly, this choice is just the ℓ^2 norm of the magnitude of the gradients of the color channels. This choice leads to a variational form that is denoted as $L^1 \diamond \ell^2 \diamond \ell^2(D\tilde{\mathbf{f}}_1)$-norm by Blomgren and Chan [81]. In their analysis they criticized this choice as being biased towards equal transitions in all three color channels. Indeed, this is true and usually the magnitude of the gradient for each channel will be different, especially in purely-chromatic transition regions. They proposed the $\ell^2 \diamond L^1 \diamond \ell^2(D\tilde{\mathbf{f}}_1)$-norm which is basically the second norm of the scalar total variation norm of the three channels.

I performed many comparisons for up-sampling color images using the $\mathcal{N}_+$ and other 3 vectorial variational formulations that I proposed and implemented for investigation. I only got a subtle enhancement over the independent channel by channel processing in the RGB color space. This led my research in a different direction as

given in the following section.

5.2.3 Unified perception of geometrical structures in color images

The main influential properties of the HVS on the color image up-sampling approach that I have taken are based on the analyses by Zhang and Wandell [82]. Their analyses demonstrated that a spatial-CIELAB color space is closer to the properties of the HVS than the CIELAB. They found that the CIELAB does not account for the spatial frequency and was only based on the ability of humans to distinguish two constant areas of different color stimulus. Based on their analysis it is straightforward to conclude the following:

1. Humans perceive most of the geometric-structure outlines and deep fine details from a luminance channel.

2. The chromatic channels act as complementary information and are perceived with lower bandwidth by the HVS than the luminance channel.

Hence, they developed the *S-CIELAB* space which filters the chromatic channels in an opponent color space more than the luminance representative in this space. Then the filtered channels are converted to the CIELAB color space. I concluded that one can hope to have better color image magnification by applying these concept to the up-sampling scheme. In other words there are two important conceptual observations

1. the spatial processing of the color channels can be decorrelated in an appropriate color space;

2. better results can be obtained by up-sampling the luminance representative component with higher quality than that of the chromatic components. This can be done by redistributing the computational power with higher share to the luminance than the shares of both chromatic channels.

Now, the idea of variational vectorial processing may seem to be a less effective choice for two reasons:

1. In the general sense, it is not adapted to the spatial response of the HVS to the color information which is of different bandwidth for each color channel in a general luminance-chrominance color-space;

2. It tends to obtain nearly equal magnitude of the gradient (transitions) among all color channels as described in the previous section. This makes it suitable for implementation in color spaces like RGB where no single channel contains the luminance information exclusively.

Color spaces characterized by general luminance-chrominance components such as YCbCr and opponent color spaces, have drastically different values for the magnitude of the gradient in each color channel for the same spatial location. The luminance channel containing more spatial frequency contents is expected to have higher magnitude of the spatial gradient than that in the chromatic channels. Generally, a variational vectorial formulation in this kind of color spaces will prefer distributing the spatial transitions equally among the color channels. This will result in blurring the luminance channel which blurs the perceived image while sharpening the chromatic channels unnecessarily as they will be refiltered by the HVS. That is why I think that the variational vectorial formulation will give its best results in RGB color space.

Hypothesis 1. *For any natural color image* $\mathbf{f}_1[\mathbf{x}]$ *there exists a scalar image* $f_1[\mathbf{x}]$ *that contains the maximum perceived contents in* $\mathbf{f}_1[\mathbf{x}]$ *and can be described by*

$$f_1 = \min_g \mathcal{J}_c(\mathbf{f}_1, g),$$
$$\mathcal{J}_c(\mathbf{f}_1, f_1) \triangleq \mathfrak{Q}(\mathcal{M}_{\mathbf{x}}(f_1) - \mathcal{M}_{\mathbf{x}}(\mathfrak{G}(\mathbf{f}_1)).$$

$\mathfrak{G}$ is a process that maps the color image $\mathbf{f}_1$ to a scalar image. Then for $\mathbf{f}_1 \in \mathbb{R}^3$ as in RGB color space we have $\mathfrak{G} : \mathbb{R}^3 \to \mathbb{R}$. The preferred properties in the HVS can be

roughly quantified in $\mathcal{M}_{\mathbf{x}}$, and $\mathfrak{Q}$ is a mathematical metric that penalizes deviations. This proposition is in accordance with the ideas in [83, 84]. Caselles et al. [83] suggested a linear combination of the color components of $\mathbf{f}_1$, specifically they chose the luminance in the HSV color space. An implemented example of this proposition was given in [84] if we set $\mathfrak{Q} = \ell_2$, $\mathcal{M}_{\mathbf{x}} = \nabla_{\mathbf{x}}$, and $\mathcal{M}_{\mathbf{x}}\mathfrak{G} = \mathfrak{F}(\lambda_-, \lambda_+)$ as described in the previous section. The authors in [84] were able to obtain f_1 from a given $\mathbf{f}_1$ by solving the optimization problem given by proposition 1. The idea is to find the best scalar image that matches the vectorial gradient of $\mathbf{f}_1$ based on the first fundamental form using the Riemannian geometry as developed in [78].

In the simplest form we can set $\mathfrak{Q}$ to be an ℓ_p-norm, $\mathcal{M}_{\mathbf{x}}$ be an identity operator, and $\mathfrak{G}$ be a mapping to the luminance. By this setup, the scalar image f_1 described by proposition 1 will be the luminance of $\mathbf{f}_1$. Hence, I will simply up-sample the luminance of $\mathbf{f}$ with high-quality and independently from the chromatic channels up-sampling, as shown in the next section.

5.2.4 Color image up-sampling implementation

The extension of the scalar variational up-sampling method to color image up-sampling is given in algorithm 6.

Algorithm 6. ***Color image up-sampling*** *($\mathbf{f}_2,\ \lambda,\ \Delta T,\ \epsilon$)*

1. Convert $\mathbf{f}_2$ from gamma-corrected RGB to YCbCr
2. set ϵ_Y to be very small compared to ϵ
3. Up-sample Y using algorithm 7 as $\grave{Y} =$ channel up-sampling$(Y, \lambda, \Delta T, \epsilon_Y)$
4. Up-sample Cb using algorithm 7 as $\grave{C}_b =$ channel up-sampling$(C_b, \lambda, \Delta T, \epsilon)$
5. Up-sample Cr using algorithm 7 as $\grave{C}_r =$ channel up-sampling$(C_r, \lambda, \Delta T, \epsilon)$

6. Obtain $\mathbf{f}_1$ by converting ŸČbČr back to gamma-corrected RGB

7. Store $\mathbf{f}_1$

Algorithm 7. ***Channel up-sampling*** *(f_2, λ, ΔT, ϵ)*

1. Initialize $f_1^{(0)}$ by any arbitrary image

2. set $n = -1$

3. Do until termination criterion is satisfied

   (a) $n = n + 1$

   (b) Estimate the preconditioned mean curvature $\|\nabla_{\mathbf{x}} f_1^{(n)}\|\kappa^{(n)}$ by Algorithm 2 or 3.

   (c) Compute the error $e^{(n)} = Hf_1^{(n)} - f_2$ as in Fig. 5.3

   (d) Compute the residue $r^{(n)} = H^{\mathrm{T}} e^{(n)}$ as shown in Fig. 5.3

   (e) $f_1^{(n+1)} = f_1^{(n)} + \Delta T(\lambda\|\nabla_{\mathbf{x}} f_1^{(n)}\|\kappa^{(n)} - r^{(n)})$

   (f) If MSE$(f_1^{(n+1)}, f_1^{(n)}) < \epsilon$ then terminate

4. Return $f_1^{(n)}$

The first experiment that I have run was for up-sampling a portion of the famous bike image, used in the JPEG2000 evaluation, shown in Fig. 5.2.4(b). The up-sampling factor was 5 in each dimension, for $\lambda = 0.05$, $\Delta T = 1$, and assuming a Gauss-Gauss($\downarrow$ 25) observation model scenario. The chromatic channels were up-sampled using 300 iterations while the luminance channel was up-sampled using 5000 iterations. The result is shown in Fig. 5.2.4(a) and for comparison the cubic B-spline was used for each channel independently and its result is shown in 5.2.4(c)

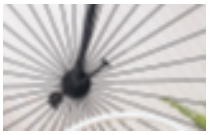

(a)

(b)

(c)

Fig. 5.15 Up-sampling of a portion of the bike image by a factor of 25 using (a) proposed approach $\lambda = 0.05$ (b) Cubic B-splines.

It is apparent that the result of the proposed approach is better than cubic B-spline. In the proposed approach the spokes of the bike are up-sampled as straight objects with no wavy effect as in Cubic B-spline method. There are no oscillations around the spokes in the background as those in the result using the Cubic B-spline. Overall the image looks more clear using the proposed approach compared to using the cubic B-spline.

The second comparison is done to compare the proposed approach to a state-of-the-art variational vectorial method described in the framework of the Riemannian geometry by the regularizer $\mathcal{J}_s = \sqrt{\lambda_- + \lambda_+}$ which is the ℓ_2-norm of the magnitude of the spatial gradients of the RGB color channels and denoted by $\mathcal{N}_+$ in [80]. For visual comparison the result obtained using the proposed approach in (b) is reprinted again in Fig. 5.16(a), while that of the vectorial norm is shown in Fig. 5.16(b).

The results are very close, and the proposed approach is slightly better in some regions. The areas labelled (a) near the spokes has some color artifact appearing like white shadow in the vectorial approach. The central region labelled (b) where the spokes are converging is a region of higher frequency; the proposed approach reconstructed these frequency contents slightly better that is why it looks more distinguishable than that in the vectorial method. Two more examples for up-sampling a portion of the flowers image shown in Fig. 5.17(a) and Fig. 5.18(a) by a factor of 5 in each dimension using the proposed approach (Fig. 5.17(b), Fig. 5.18(b)) and cubic B-spline (Fig. 5.17(c), Fig. 5.18(c)). The parameters used for the result in Fig. 5.17(b) are $\lambda = 0.05$, $\Delta = 0.25$, and 300 iterations and for the result in Fig. 5.18(b) are $\lambda = 0.15$, $\Delta = 0.25$, and 300 iterations. It clear from the figures that the results by the proposed approach is superior to the results by the cubic B-spline. The results of the proposed approach does not suffer from color artifacts at the edges that are present in the results of cubic B-spline.

(a)

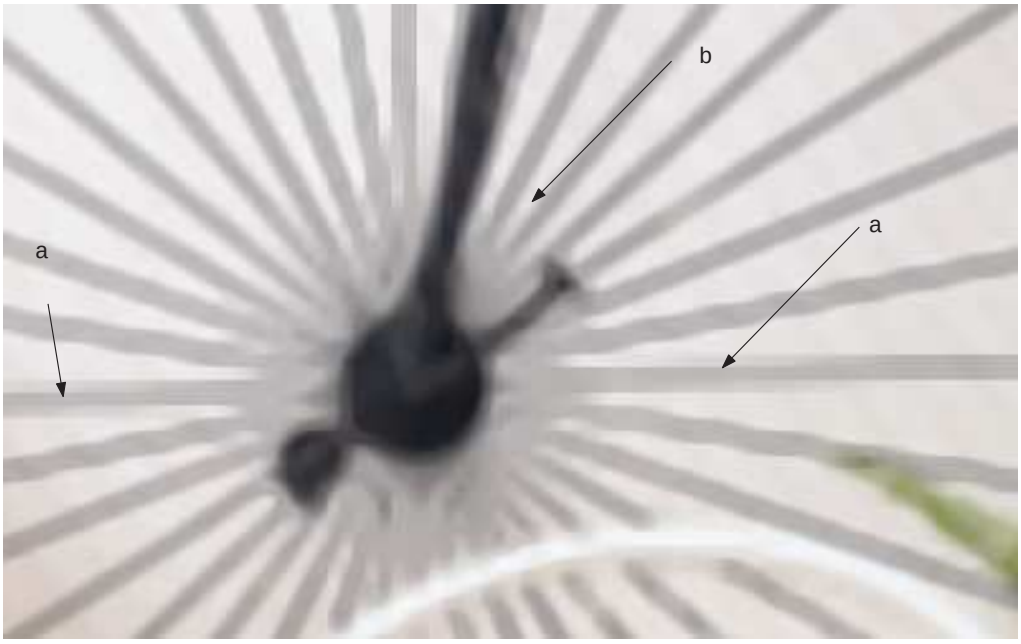

(b)

Fig. 5.16 Up-sampling of a portion of the bike image by a factor of 25 using (a) proposed approach $\lambda = 0.05$ (b) vectorial approach $\mathcal{N}_+$.

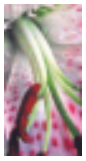

(a)

(b)

(c)

Fig. 5.17 Up-sampling of (a) a portion of the flowers image by a factor of 25 using (b) proposed approach $\lambda = 0.05$ (c) Cubic B-splines.

(a)

(b)

(c)

Fig. 5.18 Up-sampling of (a) a portion of the flowers image by a factor of 25 using (b) proposed approach $\lambda = 0.12$ (c) Cubic B-splines.

Chapter 6

Conclusions and Future Work

This chapter provides a summary of the work presented and the conclusions drawn from this research. It lists the contributions to knowledge already achieved in this work and provides directions for future work.

6.1 Summary and conclusions

In this thesis I have presented a regularization approach to the up-sampling of high-quality images from lower resolution (LR) grey-scale and color images. The regularized image up-sampling problem has been formulated using two ingredients: a newly designed observation model and the total-variation regularizer. The observation model, relating the up-sampled higher resolution (HR) image to the given LR image, leads to the design of the data fidelity criterion. The observation model has been an outcome of analyses of the image up-sampling problem from a new perspective. These analyses have led to the introduction of a new concept which is the theoretical (virtual) camera. Furthermore, the theoretical camera has been optimally designed to be adapted to the properties of the display device used. The need for an optimal design process directed me to generalize the minimum-error-sampling theorem, which was developed by Unser [14] for 1-D and Cartesian grids, to arbitrary sampling lattices. The total-variation

regularizer caused the objective criteria to be of the variational type. Hence, this formulation has led to a variational optimization problem. The variational optimization problem has been analyzed using the Euler–Lagrange formulation which has yielded a set of partial differential equations (PDEs). The numerical solution of these PDEs has been implemented using the level set method (LSM). The LSM is characterized in general by a space-varying evolution speed. I have introduced two hybrid interacting speeds for the LSM used that led to a homogenous unimodal solution method which is not trapped in the constant-image solution as in other implementations of the LSM.

First, the image up-sampling problem has been analyzed from a new perspective. It has been assumed that there exists an ideal HR image that can be obtained from the original continuous-space(-time) scene by a theoretical (virtual) high-quality camera. This is analogous to the process of acquiring the given LR image. The LR image was obtained from the original continuous-space(-time) scene by a real physical camera. This real physical camera is governed by the physical realization constraints. On the contrary, the virtual camera used to obtain the ideal HR image is not restricted by any physical realization constraints. Hence, obtaining a high-quality up-sampled image from the given LR image has become a problem of obtaining the best estimate of this ideal HR image. This estimation problem has been formulated in a regularization framework, specifically a data fidelity criterion and a total-variation regularizer.

The data fidelity criterion has been designed in accordance with a novel design of the observation model. Generally the observation model is described by a digital prefilter followed by down-sampling from the HR image sampling lattice to the LR image sampling lattice. An exploratory research whose outcome has been one of the major contributions of this thesis, a generalized design of the observation model. The theoretical analysis has been performed in the frequency domain deriving a closed form for the observation model. This generalization is in the sense of the underlying scenario setup. A scenario is described by any combination of LSI prefilter model for

both the physical camera used to acquire the LR image and the theoretical camera used to acquire the ideal HR image, the sampling lattice of the ideal HR image, and that of the LR image. A necessity for the analysis is the power spectral density (PSD) estimation of the continuous-space(-time) original image. I have estimated this PSD by two methods: the Welch-modified periodogram method from a very-high resolution image and the commonly-used parametric exponential model for images. In both cases the observation models obtained for a specific scenario were the same. The main conclusion drawn from designing the observation model for many scenarios is that the commonly-used moving average as a prefilter is not suitable for many scenarios and is inferior in performance compared to the prefilter designed by the theory developed here.

The observation model design depends on the choice of the theoretical camera used in the scenario setup. Since the HR image will be eventually presented to a human viewer by using a display device, then the theoretical camera ought be optimally designed to serve this purpose. I have designed the theoretical camera to be adapted to the properties of the display device. Its design has been optimized to minimize the MSE between the continuous-space-time original scene and the reconstructed one by the display device. This optimal design problem was introduced by Aldroubi and Unser [85] for 1-D and Cartesian grids. I have extended the theorem to arbitrary sampling lattices which is necessary for a variety of practical image acquisition devices. By completion of the optimal design of the theoretical camera, the observation model has become available and hence the data fidelity criterion is specified.

The total-variation regularizer has shown success in various applications in image processing like restoration, segmentation, and motion estimation. Its successful results emerge from its preference to the image with the least oscillatory iso-intensity contours while not penalizing occurrences of discontinuities (edges) in the image. Being a norm of the spatial partial derivatives, the total-variation norm is generally defined for

continuous functions. Hence, its criterion is analyzed using Euler's equation resulting in a PDE whose steady state solution is characterized by the so-called evolution by mean curvature. The numerical implementation of this evolution by mean curvature has been performed using the LSM which provides stable numerical schemes. The general implementation of the LSM developed for the image up-sampling problem has been described by two interacting speeds. The choice of the first speed has given rise to a descent algorithm whose gradient is the preconditioned mean curvature, while the second speed has acted as projection onto the data fidelity constraints.

The processing has been performed in a linear grey-scale space in accordance with the linear nature of the observation model design theory. Implicitly a correction of the processing to account for perceptual uniformity to the HVS has been measured in the ITU Rec. R709 gamma-corrected space. This correction has been obtained by computing the rate of change of the distance between two grey-levels in the gamma-corrected space with respect to the grey-level value in the linear non-gamma-corrected space. The result using this correction has provided a subtle enhancement over that performed directly in the gamma-corrected space ignoring the linear nature of the observation model design. The results of the proposed up-sampling approach have manifested significant enhancements over many methods including cubic B-splines and the Tikhonov regularization method. The edges are sharper and clear; the contours of long edges are crisp with no oscillatory patterns or waves along them. The smooth regions closer to the edges does not suffer from any ringing artifacts unlike most of the adaptive techniques.

The approach has been extended to color image up-sampling. First, many variational vectorial formulations that incorporate the three color channels have been proposed and used. One state-of-the-art variational vectorial formulation from the literature which is the norm of the vector gradients has been implemented and tested. All these methods have been implemented in the RGB device space and have been com-

pared to the scalar variational approach applied to every color channel independently. Comparing the results visually, I have concluded that the improvement obtained by these vectorial formulations over the scalar formulation applied independently to the color channels is very subtle and does not pay for their computational complexity. This conclusion was also drawn by the authors in [83] based on a different kind of analysis and personal communications with the authors of some of the variational vectorial formulations. Finally, I have tried choosing an appropriate color space that decorrelates the spatial processing across the color channels. Several color spaces have been tried like the legacy YCbCr and some of the latest opponent color spaces. I performed the scalar variational scheme independently to every color channel and I found the results are better than the vectorial formulations implemented in the RGB device space. The results obtained in the YCbCr and the opponent color spaces were greatly alike. I concluded that the implementation should be done in the YCrCb color space independently for every color channel. Furthermore, I found that one should put more computational cost (more iterations) to up-sample the luminance Y channel with high quality at the expense of less quality up-sampling for both chromatic channels Cb and Cr. This is due to the classical fact that humans perceive most of the geometrical information, especially the fine details, from the Y channel.

6.2 Thesis contributions

In this thesis research I proposed, and successfully implemented a solution to the grey-scale image magnification problem with higher perceived resolution. I also proposed approaches to provide a solution for the color-image up-sampling problems. By the completion of this thesis I have solved two main problem in the field of image processing, with a corresponding list of contributions to the field. These contributions are listed as follows:

1. New formulation of the problem of image up-sampling with the introduction

of the new concept of a theoretical camera that acquires an ideal HR image (Fig. 2.5).

2. This new formulation of the problem led to a generalized design of the observation model for the regularized image up-sampling problem (Fig. 4.1). This observation model is derived and designed for

   (a) Any dimension 2-D, 3-D or even higher;

   (b) Any scenario modelling the properties of the physical and the virtual camera;

   (c) Any up-sampling factor;

   (d) General lattices Λ, Γ that are not necessarily rectangular to rectangular.

3. New design for the theoretical camera that is optimized for a specific modelled display device (Fig. 4.6). This design problem led to the development of a generalization of the minimum-error sampling theory which was developed by Unser in [14] to non-orthogonal bases. This generalization is for arbitrary sampling structures (Theorem 1, 2).

4. Development of a new methodology for color space processing. This method allows the implementation to be implicitly executed in a perceptually-uniform space (section 5.2.1).

5. Development of a variational scheme for image up-sampling that involves two sampling structures Λ and Γ as part of the formulation and dealing with the Euler–Lagrange equation for the involved down-sampling operator (3.18).

6. Selecting two interacting speeds for the level set method that provides a stable numerical solution that can be started from any initial value image including the constant images and not being trapped in local minima as with other approaches.

All the above mentioned contributions, except for the contribution numbered four, appear in my publications as follows:

1. Contributions numbered one and two have been published in [60].

2. Contributions numbered five and six have been published in [59].

3. Contribution numbered three has been accepted and is currently in press [68].

6.3 Future directions

6.3.1 Observation model adapted to shadow-mask color displays

The design of the observation model in this thesis was adapted to in-depth analysis of the properties of the typical grey-scale display device. An immediate extension is to extend the analysis and the design of the observation model for shadow mask-type color display devices. In the shadow mask CRT and TFT monitors the color phosphor dots are arranged in a hexagonal pattern while the scan line driving the three electron beams sweeps the monitor in the same typical horizontal fashion. It is the shape of the shadow mask which determines where each electron beam falls on the different color phosphor dots. Furthermore there is a spatial offset for these beams that is always adjusted by the user of the display device. The combination of these characteristics in a model for the reconstruction function of the display device is interesting, and more interesting is to find the optimal theoretical camera adapted to this display function. Finally, this fuses inside the design of the optimal observation model used in the up-sampling problem for color images.

6.3.2 Color-filter-array image up-sampling

The completion of the grey-scale and color image up-sampling problem in this thesis motivates pursuing the research towards solving the color-filter array image mosaic

up-sampling. Most commercial CCD cameras uses a color-filter-array because it is more economical than the beam-splitter technology. Thus we have only one value of the three color channels at each spatial location. A commonly-used sampling lattice in this case is the Bayer structure as shown in Fig. 6.1 [86]. The Green channel is sampled at twice the sampling density of both the red and blue channels. The Green channel is sampled on a hexagonal lattice while the red and blue channels are sampled on a rectangular one. Thus we can write their sampling matrices as

$$V_{\Xi_G} = \begin{pmatrix} 2X & X \\ 0 & X \end{pmatrix}, \quad V_{\Xi_R} = V_{\Xi_B} = \begin{pmatrix} 2X & 0 \\ 0 & 2X \end{pmatrix} \tag{6.1}$$

where the subscript indicates the color channel. Demosaicking of the color filter

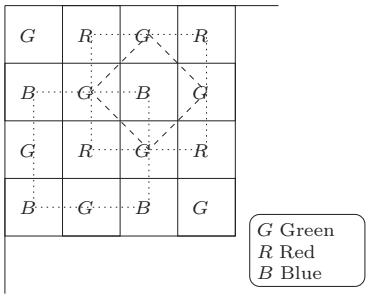

Fig. 6.1 Bayer-type color filter array.

array is the problem of finding the missing samples of all color channels. This is seen as up-sampling the three channels to a rectangular lattice Γ which is defined by the sampling matrix $V_\Gamma = \mathrm{diag}(X, X)$ for a sampling period X, where $d(\Gamma) = \frac{1}{2}d(\Xi_G) = \frac{1}{4}d(\Xi_R) = \frac{1}{4}d(\Xi_B)$. It should be noted that the commercial CCD cameras perform a post-processing to solve the demosaicking problem and provide the consumer with three color channels which are defined on Γ. This technique is usually

not optimized and researchers are still pursuing better approaches. Gunturk et al. [87] have recently proposed a successful approach for this problem that outperformed many other approaches. Messing and Sezan [88] proposed a scheme for this problem that integrates a sequence of color-filter array images to obtain the result defined on Γ. This is based on the idea of super-resolution for a sequence of images.

6.3.3 Image sequence super-resolution and video up-sampling

The solutions to the set of problems in this thesis actually constitute a rigorous foundation for many other interesting applications and problems. The most interesting one is the super-resolution problem to reconstruct an HR image from a set of LR images. With the deployment of a reliable motion estimation technique, the super-resolution problem will benefit a lot from the theories that were developed in this thesis. For instance, the observation model developed in chapter 4 is directly applicable to the super-resolution problem when the temporal aperture is to be involved. This will design a 3-D observation model that when coupled with motion estimation will provide a good foundation for accounting for motion blur and warping due to the temporal aperture. Another application is the conversion of an LR video sequence to an HR cinematic sequence.

References

[1] T. Blu, P. Thévenaz, and M. Unser, "How a simple shift can significantly improve the performance of linear interpolation," in *Proc. IEEE Int. Conf. Image Processing*, vol. 3, pp. 377–380, 2002.

[2] E. Dubois, "Video sampling and interpolation," in *Handbook of Image and Video Processing* (A. Bovik, ed.), ch. 7.2, pp. 645–654, San Diego, CA: Academic Press, 2000.

[3] E. Dubois, "The sampling and reconstruction of time-varying imagery with application in video systems," *Proc. IEEE*, vol. 73, pp. 502–522, Apr. 1985.

[4] O. Schade, Sr., "Image reproduction by a linear raster process," in *Perception of displayed information* (L. M. Biberman, ed.), pp. 233–278, New York: Plenum, 1973.

[5] S. Coulombe and E. Dubois, "Nonuniform perfect reconstruction filter banks over lattices with application to transmultiplexers," *IEEE Trans. Signal Process.*, vol. 47, pp. 1010–1022, Apr. 1999.

[6] R. R. Schulz and R. L. Stevenson, "A Bayesian approach to image expansion for improved definition," *IEEE Trans. Image Process.*, vol. 3, pp. 233–242, May 1994.

[7] G. Golub and C. V. Loan, *Matrix Computations*. Baltimore: The John Hopkins University Press, 3 ed., 1996.

[8] J. Hadamard, *Lectures on Cauchy's Problem in Linear Partial Differential Equations*. NY: Dover Pub. Inc., 1952.

[9] P. D. Welch, "The use of fast Fourier transform for the estimation of power spectra: A method based on time averaging over short, modified periodograms," *IEEE Trans. Audio Electroacoust.*, vol. AU-15, pp. 70–73, June 1967.

[10] E. Dubois, "Spectral analysis of image sequences," Tech. Rep. 83-03, Institut national de la recherche scientifique (INRS), Montréal QC, Canada, Feb. 1983.

[11] J. P. Allebach, "Image scanning, sampling, and interpolation," in *Handbook of Image and Video Processing* (A. Bovik, ed.), ch. 7.1, pp. 629–643, San Diego, CA: Academic Press, 2000.

[12] R. Keys, "Cubic convolution interpolation for digital image processing," *IEEE Trans. Acoust. Speech Signal Process.*, vol. 29, pp. 1153–1160, Dec. 1981.

[13] M. Unser, "Splines: A perfect fit for signal and image processing," *IEEE Signal Process. Mag.*, vol. 16, pp. 22–38, Nov. 1999.

[14] M. Unser, "Sampling—50 years after Shannon," *Proc. IEEE*, vol. 88, pp. 569–587, Apr. 2000.

[15] A. Muñoz, T. Blu, and M. Unser, "Least-squares image resizing using finite differences," *IEEE Trans. Image Process.*, vol. 10, pp. 1365–1378, Sept. 2001.

[16] A. Gotchev, K. Egiazarian, J. Vesma, and T. Saramäki, "Edge-preserving image resizing using modified B-splines," in *Proc. IEEE Int. Conf. Acoustics Speech Signal Processing*, vol. 3, pp. 1865–1868, 2001.

[17] Q. Wang, R. Ward, and H. Shi, "Isophote estimation by cubic-spline interpolation," in *Proc. IEEE Int. Conf. Image Processing*, vol. 3, pp. 401–404, Sept. 2002.

[18] J. Allebach and P. W. Wong, "Edge-directed interpolation," in *Proc. IEEE Int. Conf. Image Processing*, vol. 3, pp. 707–710, Sept. 1996.

[19] A. Biancardi, L. Cinque, and L. Lombardi, "Improvements to image magnification," *Pattern Recognit.*, vol. 35, pp. 677–687, Mar. 2002.

[20] Q. Wang and R. Ward, "A new edge-directed image expansion scheme," in *Proc. IEEE Int. Conf. Image Processing*, vol. 3, pp. 899–902, 2001.

[21] X. Lu, P. S. Hong, and M. J. Smith, "An efficient directional image interpolation method," in *Proc. IEEE Int. Conf. Acoustics Speech Signal Processing*, vol. 3, pp. 97–100, Apr. 2003.

[22] S. Carrato, G. Ramponi, and S. Marsi, "A simple edge-sensitive image interpolation filter," in *Proc. IEEE Int. Conf. Image Processing*, vol. 3, pp. 711–714, 1996.

[23] K. Ratakonda and N. Ahuja, "POCS based adaptive image magnification," in *Proc. IEEE Int. Conf. Image Processing*, vol. 3, pp. 203–207, 1998.

[24] W. K. Carrey, D. B. Chuang, and S. S. Hemami, "Regularity-preserving image interpolation," *IEEE Trans. Image Process.*, vol. 8, pp. 1293–1297, Sept. 1999.

[25] T. Chen, H. R. Wu, and B. Qiu, "Image interpolation using across-scale pixel correlation," in *Proc. IEEE Int. Conf. Acoustics Speech Signal Processing*, vol. 3, pp. 1857–1860, 2001.

[26] X. Li and T. Orchard, "New edge-directed interpolation," *IEEE Trans. Image Process.*, vol. 10, pp. 1521–1527, Oct. 2001.

[27] S. Carrato and L. Tenze, "A high quality 2× image interpolator," *Signal Process. Lett.*, vol. 7, pp. 132–134, June 2000.

[28] Y. Takahashi and A. Taguchi, "An enlargement method of digital images with the prediction of high-frequency components," in *Proc. IEEE Int. Conf. Acoustics Speech Signal Processing*, vol. 4, pp. 3700–3703, 2002.

[29] N. Shezaf, H. Abramov-Segal, I. Sutskover, and R. Bar-Sella, "Adaptive low complexity algorithm for image zooming at fractional scaling ratio," in *21st IEEE Conv. Electrical and Electronic Engineers in Israel*, pp. 253 –256, 2000.

[30] A. Darwish, M. Bedair, and S. Shaheen, "Adaptive resampling algorithm for image zooming," *IEE Proc., Vis., Image and Signal Process.*, vol. 144, pp. 207–212, Aug. 1997.

[31] W. C. Karl, "Regularization in image restoration and reconstruction," in *Handbook of Image and Video Processing* (A. Bovik, ed.), ch. 3.6, pp. 141–160, San Diego, CA: Academic Press, 2000.

[32] A. Katsaggelos and C. Tsai, "Iterative image restoration," in *Handbook of Image and Video Processing* (A. Bovik, ed.), ch. 3.9, pp. 191–206, San Diego, CA: Academic Press, 2000.

[33] C. Kelley, *Iterative Methods for Optimization*. Philadelphia: Society of Industrial and Applied Mathematics (SIAM), 1999.

[34] S. Geman and D. Geman, "Stochastic relaxation, Gibbs distribution, and the Bayesian restoration of images," *IEEE Trans. Pattern Anal. Machine Intell.*, vol. 6, pp. 721–741, 1984.

[35] C. Bouman and K. Sauer, "A generalized Gaussian image model for edge-preserving MAP estimation," *IEEE Trans. Image Process.*, vol. 2, pp. 296–310, July 1993.

[36] D. Rajan and S. Chaudhuri, "Generation of super-resolution images from blurred observations using Markov random fields," *Proc. IEEE Int. Conf. Acoustics Speech Signal Processing*, vol. 3, pp. 1837–1840, 2001.

[37] P. Perona and J. Malik, "Scale-space and edge detection using anisotropic diffusion," *IEEE Trans. Pattern Anal. Machine Intell.*, vol. 12, pp. 629–639, July 1990.

[38] L. Rudin, S. Osher, and E. Fatemi, "Nonlinear total variation based noise removal algorithms," *Physica D*, vol. 60, pp. 259–268, 1992.

[39] L. Alvarez, P. Lions, and J. Morel, "Image selective smoothing and edge detection by nonlinear diffusion," *SIAM J. Num. Anal.*, vol. 29, pp. 845–866, June 1992.

[40] Y. You, W. Xu, A. Tannenbaum, and M. Kaveh, "Behavioral analysis of anisotropic diffusion in image processing," *IEEE Trans. Image Process.*, vol. 5, pp. 1539–1552, Nov. 1996.

[41] M. Giaquinta and S. Hildebrandt, *Calculus of Variations*. NY: Springer-Verlag, 1996.

[42] W. F. Ames, *Numerical Methods for Partial Differential Equations*. London: Nelson, 1969.

[43] E. Kreyszig, *Advanced Engineering Mathematics*. New York: John Wiley & Sons, Inc., 2 ed., 1967.

[44] S. T. Acton, "Diffusion-based edge detectors," in *Handbook of Image and Video Processing* (A. Bovik, ed.), ch. 4.12, pp. 433–458, San Diego, CA: Academic Press, 2000.

[45] R. T. Whitaker and S. M. Pizer, "A multi-scale approach to nonuniform diffusion," *CVGIP: Image Underst.*, vol. 57, pp. 99–110, Jan. 1993.

[46] S. Osher and J. Sethian, "Fronts propagating with curvature dependent speed: Algorithms based on the Hamilton-Jacobi formulation," *Comput. Physics J.*, vol. 79, pp. 12–49, 1988.

[47] N. Nguyen, P. Milanfar, and G. Golub, "Efficient generalized cross-validation with applications to parametric image restoration and resolution enhancement," *IEEE Trans. Image Process.*, vol. 10, pp. 1299–1308, Sept. 2001.

[48] H. Jiang and C. Moloney, "A new direction adaptive scheme for image interpolation," in *Proc. IEEE Int. Conf. Image Processing*, vol. 3, pp. 369–372, 2002.

[49] B. Morse and D. Schwartzwald, "Image magnification using level-set reconstruction," in *Proc. IEEE Conf. Computer Vision Pattern Recognition*, vol. 1, pp. 333–340, 2001.

[50] B. Morse and D. Schwartzwald, "Isophote-based interpolation," in *Proc. IEEE Int. Conf. Image Processing*, vol. 3, pp. 227–231, 1998.

[51] G. Gilboa, N. Sochen, and Y. Y. Zeevi, "Forward-and-backward diffusion processes for adaptive image enhancement and denoising," *IEEE Trans. Image Process.*, vol. 5, pp. 689–703, July 2002.

[52] G. Gilboa, Y. Zeevi, and N. Sochen, "Anisotropic selective inverse diffusion for signal enhancement in the presence of noise," in *Proc. IEEE Int. Conf. Acoustics Speech Signal Processing*, vol. 1, (Istanbul, Turkey), pp. 221–224, June 2000.

[53] F. Guichard and F. Malgouyres, "Total variation based interpolation," in *Signal Process. IX: Theories and Applications (Proc. 9th European Signal Process. Conf.)*, vol. 3, pp. 1741–1744, 1998.

[54] S. Osher and R. Fedkiw, *Level Set Methods and Dynamic Implicit Surfaces*. NY: Springer-Verlag, 2003.

[55] J. Sethian, *Level Set Methods and Fast Marching Methods*. Cambridge, UK: Cambridge University Press, 2 ed., 1999.

[56] R. Malladi and J. Sethian, "Image processing: Flows under min/max curvature and mean curvature," *Graph. Models and Image Process.*, vol. 58, pp. 127–141, Mar. 1996.

[57] A. Marquina and S. Osher, "Explicit algorithms for a new time dependent model based on level set motion for nonlinear deblurring and noise removal," *SIAM J. Sci. Comput.*, vol. 22, pp. 387–405, 2000.

[58] P. L. Combettes and J. Luo, "An adaptive level set method for nondifferentiable constrained image recovery," *IEEE Trans. Image Process.*, vol. 11, pp. 1295–1304, Nov. 2002.

[59] H. Aly and E. Dubois, "Regularized image up-sampling using a new observation model and the level set method," in *Proc. IEEE Int. Conf. Image Processing*, vol. 3, pp. 665–668, 2003.

[60] H. Aly and E. Dubois, "Crafting the observation model for regularized image up-sampling," in *Proc. IEEE Int. Conf. Acoustics Speech Signal Processing*, vol. 3, pp. 101–104, 2003.

[61] B. Tom and A. Katsaggelos, "Resolution enhancement of monochrome and color video using motion compensation," *IEEE Trans. Image Process.*, vol. 10, pp. 278–287, Feb. 2001.

[62] S. Baker and T. Kanade, "Limits on super-resolution and how to break them," *IEEE Trans. Pattern Anal. Machine Intell.*, vol. 24, pp. 1167–1183, Sept. 2002.

[63] M. Elad and A. Feuer, "Restoration of single superresolution image from several blurred, noisy, and undersampled measured images," *IEEE Trans. Image Process.*, vol. 6, pp. 1646–1658, Dec. 1997.

[64] S. Borman and R. L. Stevenson, "Super-resolution for image sequences - A review," in *Proc. IEEE Int. Symp. Circuits and Systems*, pp. 374–378, 1998.

[65] R. Y. Tsai and T. S. Huang, "Multiframe image restoration and registration," in *Advances in Computer Vision and Image Processing* (T. S. Huang, ed.), vol. 1, ch. 7, pp. 317–339, London UK: JAI Press, 1984.

[66] S. Coulombe and E. Dubois, "Linear phase and symmetries for multidimensional FIR filters over lattices," *IEEE Trans. Circuits Syst. II, Analog Digit. Signal Process.*, vol. 45, pp. 473–481, Apr. 1998.

[67] R. N. Bracewell, *The Fourier Transform and Its Applications.* McGraw-Hill, 3 ed., 2000.

[68] H. A. Aly and E. Dubois, "Design of optimal camera apertures adapted to display devices over arbitrary sampling lattices," *Signal Process. Lett., Apr. 2004, to appear.*

[69] D. Van De Ville, W. Philips, and I. Lemahieu, "Least-squares resampling to a hexagonal lattice," *Signal Process., Image Commun.*, vol. 17, pp. 393–408, May 2002.

[70] S. Mallat, *A Wavelet Tour of Signal Processing.* CA: Academic Press, 2 ed., 1999.

[71] A. Mertins, *Signal Analysis.* UK: John Wiley & Sons, Inc., 1999.

[72] M. A. Isnardi, "Modeling the television process," Tech. Rep. 515, RLE, MIT, Cambridge, Massachusetts, May 1986.

[73] P. L. Combettes, "A block-iterative surrogate constraint splitting method for quadratic signal recovery," *IEEE Trans. Signal Process.*, vol. 51, pp. 1771–1782, July 2003.

[74] H. H. Bauschke and P. L. Combettes, "Construction of best Bergman approximations in reflexive Banach spaces," *Proc. Amer. Math. Soc.*, vol. 131, pp. 3757–3766, 2003.

[75] G. Boccignone, M. Ferraro, and T. Caelli, "Generalized spatio-chromatic diffusion," *IEEE Trans. Pattern Anal. Machine Intell.*, vol. 24, pp. 1298–1309, Oct. 2002.

[76] G. Sharma, *Digital Color Imaging Handbook*. Boca Raton: CRC Press, 2002.

[77] G. Sharma, M. J. Vrhel, and H. J. Trussell, "Color imaging for multimedia," *Proc. IEEE*, vol. 86, pp. 1088–1108, June 1998.

[78] S. Di Zenzo, "A note on the gradient of a multi-image," *Comput. Vis. Graph. Image Process.*, vol. 33, pp. 116–125, Jan. 1986.

[79] G. Sapiro and D. Ringach, "Anisotropic diffusion of multivalued images with applications to color filtering," *IEEE Trans. Image Process.*, vol. 5, pp. 1582–1585, Nov. 1996.

[80] D. Tschumperlé and R. Deriche, "Diffusion PDEs on vector-valued images," *IEEE Signal Process. Mag.*, vol. 19, pp. 16–25, Sept. 2002.

[81] P. Blomgren and T. Chan, "Color TV: Total variation methods for restoration of vector-valued images," *IEEE Trans. Image Process.*, vol. 7, pp. 304–309, Mar. 1998.

[82] X. Zhang and B. A. Wandell, "A spatial extension of CIELAB for digital color-image reproduction," *J. SID*, vol. 5-1, pp. 61–66, 1997.

[83] V. Caselles, B. Coll, and J. Morel, "Geometry and color in natural images," *J. Math. Imaging Vis.*, vol. 16, pp. 89–105, Mar. 2002.

[84] D. Chung and G. Sapiro, "On the level lines and geometry of vector-valued images," *Signal Process. Lett.*, vol. 7, pp. 241–243, Sept. 2000.

[85] A. Aldroubi and M. Unser, "Sampling procedures in function spaces and asymptotic equivalence with Shannon's sampling theory," *Numer. Funct. Anal. and Optimiz.*, vol. 15, pp. 1–21, 1994.

[86] B. E. Bayer, "Color imaging array." U.S. Patent 3971065, July 1976.

[87] B. K. Gunturk, Y. Altunbasak, and R. M. Mersereau, "Color plane interpolation using alternating projections," *IEEE Trans. Image Process.*, vol. 11, pp. 997–1013, Sept. 2002.

[88] D. S. Messing and M. I. Sezan, "Improved multi-image resolution enhancement for color images captured by single-CCD cameras," in *Proc. IEEE Int. Conf. Image Processing*, vol. 3, pp. 484–487, 2000.

Index